

RESEARCH AND DESIGN OF NON-FOSTER ACTIVE METAMATERIALS

by
Yifeng Fan

A thesis submitted in partial fulfilment of
the requirements for the degree of

Doctor of Philosophy

The school of Electronic Engineering and Computer Science
Queen Mary, University of London
United Kingdom

July 2013

TO MY FAMILY

Abstract

During this PhD study, metamaterials incorporating active devices such as varactors and non-Foster circuits, were researched and designed. Starting from the research on tuneable metamaterials, an electronically controlled leaky-wave (LW) antenna based on composite right/left handed (CRLH) transmission line (TL) structure was proposed which could perform a broadband beam-fixing function with the frequency range from 1 to 4 GHz. In addition, scanning from forward to backward at a fixed frequency can be achieved by manipulating the biasing voltage applied to the varactors.

Most of this study has been devoted to the non-Foster active metamaterials. First, the characterization of active magnetic metamaterials with non-Foster loads was presented. Based on the equivalent circuit model, stability of an actively-loaded loop array was examined through different analysis techniques, further to give the design specifications to achieve the broadband non-dispersive negative- $\text{Re}(\mu)$ (MNG) or μ -near-zero (MNZ) magnetic properties. Moreover, the wave propagation in the actively-loaded medium was investigated. By relating the dispersion characteristics and the effective medium properties, we henceforth proposed the design of zero-loss and broadband metamaterials.

This thesis also has covered the study of active high impedance surfaces (HIS) with non-Foster loads. As a two-dimensional metamaterial structure, HIS have been widely used in the microwave and antenna engineering. However it can be easily seen that the performance of a general passive HIS is always limited by the narrow bandwidth, thus making a broadband HIS desirable. In this work, an analytical solution to achieving a stable broadband HIS structure is given by incorporating appropriate negative impedance converter (NIC) circuits. Simulation results have verified the design approach.

Finally, the design of NIC circuits was presented as the key part of the realization of

active metamaterials. Two schemes have been adopted to realize the design of NICs, one is the operational amplifier (op-amp) based NIC, and another is based on discrete transistors. Both types of NICs were introduced and studied in this thesis.

Acknowledgments

I would like to express my deepest gratitude to my advisor Prof. Yang Hao for providing guidance and encouragement throughout my PhD study. I would like to thank Prof. Clive Parini and Dr. Akram Alomany for serving in my committee during mid-exams. I would also like to thank Dr. Khalid Z. Rajab for fruitful discussions and being an example to me with his attention to meticulous details.

Special thanks to my colleagues for providing a peaceful and friendly environment to work. I also enjoyed very much our intellectual and cultural exchange during my PhD studies. I would especially like to thank Di, Wenxuan, Tuba, Deepak, Rihannon, Jiefu, Anestis, Oscar, and Max for their support and friendship.

I would like to give the most of the credit to my family, without their support, guidance, and sacrifices, beginning from my childhood, this dissertation would not be possible. I would also like thank my girlfriend who always supported and pushed me to perform at my best, without her encouragement and patience this thesis would have never been possible.

Table of Contents

Abstract	i
Acknowledgments	iii
Table of Contents	iv
List of Figures	viii
List of Abbreviations	xx
Appendix A List of Publications	xxi
1 Introduction	1
1.1 Research Objectives and Methodology	3
1.2 Organization of the Thesis	6
1.3 Contribution of the Thesis	7
References	8
2 Research on Tuneable Leaky Wave Antennas	12
2.1 Overview of TL Structure	12
2.2 Theory of CRLH TL Metamaterials	15
2.3 General Leaky-Wave Antenna Structure	17
2.4 Electronically Controlled Fixed-Beam Leaky-Wave Antenna Design	20
2.4.1 Principle of Voltage Controlled Leaky-Wave Antenna	20

2.4.2	Circuit Design and Experimental Results	23
2.5	Conclusion	27
	References	28
3	Characterization of Active Metamaterials with Non-Foster Loads	29
3.1	Background	30
3.2	Effective Medium of Loop Arrays	31
3.2.1	The Unit Cell	31
3.2.2	Effective Permeability	33
3.3	Review of Prior Stability Analysis of Actively-Loaded Medium	34
3.3.1	Routh-Hurwitz Stability Criterion	34
3.3.2	Nyquist Stability Criterion	37
3.4	Imittance-Based Stability Characterization of Actively-Loaded Medium	39
3.4.1	Principle of Imittance-Based Stability Analysis	40
3.4.2	Application in the Design of Broadband Active Metamaterials	47
3.5	Wave Propagation in Actively-Loaded Medium	53
3.5.1	Dispersion Characteristics	53
3.5.2	Effective Medium Properties	58
3.5.3	Design of Zero-Loss and Broadband Active Metamaterials	60
3.6	Conclusions	65
	References	66
4	Noise Analysis of Active Metamaterials with Non-Foster Loads	71
4.1	Background	72
4.2	Effective Properties of Active Metamaterials	72
4.3	Analysis of Noise Performance in Active Broadband Metamaterials	74
4.3.1	0-Dimensional Case	74
4.3.2	Noise in Infinitely Periodic Metamaterials	79
4.3.3	Noise in Finite Metamaterials	86
4.3.4	Noise Figure for Metamaterials	89

4.4	Simulation of Noise Performance in Active Broadband Metamaterials . . .	97
4.5	Conclusions	101
	References	103
5	Characterization of Active High Impedance Surfaces with Non-Foster Loads	105
5.1	Background	106
5.2	Effective Medium of Loaded HIS	109
5.2.1	Equivalent Circuit Model	109
5.2.2	Reflection Properties	115
5.2.3	Surface Waves	118
5.3	Stability Characterization of Actively-Loaded HIS	122
5.3.1	Stability of HIS with Non-Foster Loads	122
5.3.2	Application in the Design of Broadband Active HIS	126
5.4	Conclusions	129
	References	130
6	Design and Analysis of Negative Impedance Converters	134
6.1	Overview of NICs	134
6.1.1	Basic Definitions	135
6.1.2	Compensation Network	137
6.1.3	Stability Analysis	140
6.2	Design and Analysis of Operational Amplifier Based NICs	142
6.2.1	Ideal Op-Amp Properties	142
6.2.2	Non-Inverting Amplifier	144
6.2.3	Ideal Op-Amp Based NIC Circuit	145
6.2.4	Real Op-Amp Based NIC Circuit	148
6.3	Design and Analysis of Transistor Based NICs	152
6.3.1	Floating NIC Circuit	152
6.3.2	Grounded NIC Circuit	156

6.4	Conclusions	162
	References	163
7	Conclusions and Future Work	165
7.1	Conclusions	165
7.2	Future Work	168

List of Figures

1.1	Materials in the ε - μ domain [7].	2
2.1	Transmission line circuit model unit-cells. (a) RH transmission line unit-cell. (b) LH transmission line unit-cell.	13
2.2	Dispersion diagrams for the unit-cells shown in Fig. 2.1. (a) RH unit-cell (black-solid). (b) LH unit-cell (red-solid). It is shown that the RH structure has a linear dispersion diagram while a LH structure has a non-linear slope.	14
2.3	Distributed realization of unit-cell shown in Fig. 2.1. (a) RH microstrip transmission line. (b) LH microstrip transmission line consisting of periodic cascade of Sievenpiper mushroom unit-cells.[2]	15
2.4	CRLH transmission line. (a) Circuit model of an unit-cell. (b) General dispersion diagram for unbalanced case. Based on the light line ($\pm k_0$), the whole region is divided into four parts plotted by different colors, indicating the different wave propagation phenomena.	16
2.5	Leaky wave antenna. (a) Concept. (b) Principle of operation. θ is the radiation angle with respect to the axis z , while k_z is the perpendicular propagation constant for radiation, related to the free space wave number k_0 and the propagation constant of the travelling wave β . [4]	18
2.6	Typical CRLH unit cell. (a) Physical size. (b) Equivalent circuit.[4] . . .	19

2.7	A novel voltage-controlled CRLH leaky-wave antenna. (a) Layout of a single unit cell. (b) Equivalent circuit model.	21
2.8	The prototype of a 12-cell voltage controlled leaky-wave antenna.	24
2.9	Measured return loss under different reverse-biasing voltages of 13 V, 18 V and 23V.	25
2.10	Measured E-field patterns of the 12-cell voltage controlled LW antenna. (a) Radiation patterns at 0 V, scanning from 1 GHz to 4 GHz. (b) Voltage controlled beam at different frequency points, scanning at 1.8 GHz, 2.27 GHz, 2.37 GHz and 2.52 GHz.	26
2.11	Theoretical and measurement results of the relation function between the voltage and the frequency.	27
3.1	Equivalent circuit of a loop and load in a system of N coupled loaded loops[6]. Summations indicate the coupling factors between the loop m and the remaining $N - 1$ loops.	32
3.2	Simulated and theoretically calculated real (a) and imaginary (b) permeabilities for a range of negative load inductances [6].	36
3.3	Nyquist contours of a periodic system of loops. The dotted lines are their reflections, which represent the plots in negative-frequency ($-\omega$) space. The negative inductance is varied from the unstable to the stable cases. The Routh-Hurwitz method gives a stable range of inductances at $L_L > -41.3nH$; the Nyquist method clearly agrees with that. (a) The Nyquist contours for $L_L = (-50, -42, -41, -30)nH$. (b) Magnification of the Nyquist contours around the -1 point. It is evident that for $L_L = (-50, -42)nH$ the systems are unstable, while for $L_L = (-41, -30)nH$ the systems are stable.[12]	39
3.4	Source-load system.	41
3.5	Various stability criteria and their forbidden regions in the complex plane [27].	43

3.6	EPSC-based forbidden region versus ESAC and GMPM regions.	44
3.7	(a) The EPSC boundary in the complex plane where $M_S = 2$, and k is varied from 1 to 3. (b) The corresponding impedance constraint of the active load at a given frequency of $300MHz$	45
3.8	(a) Stability constraint of the active load in the impedance space. In this space, the x-axis is frequency s , the y-axis is phase PM in degree, and z-axis is magnitude GM in dB. Thus, any arbitrary impedance can be expressed by $GM(s)\angle PM(s)$. The load is defined as a parallel negative RLC circuits with $R_L = -1000\Omega$, $C_L = -5pF$ and $L_L = (-41nH, -42nH)$. (b) Magnification of the stability constraint around the intersection region. It shows that the red curve penetrates the forbidden region (unstable case) whereas there is no intersection for the blue curve and the forbidden region(stable case), which is in agreement with Routh-Hurwitz criterion. .	47
3.9	Equivalent circuit of a coupled loop with non-Foster loads. The non-Foster elements are obtained as the output of a NIC circuit terminated in a parallel positive RLC load Z_N	48
3.10	Impedance of the NIC circuits simulated using Agilent ADS, as compared to the ideal models. In all cases, the ideal NIC output is a parallel-RLC circuit with $R_L = -1000\Omega$ and $C_L = -2pF$. The negative inductance is $L_L = (-5, -10, -15)nH$. The simulation results are obtained as the output of the practical NIC network terminated a parallel RLC load with $R_N = 1000\Omega$ and $C_N = 2pF$ and $L_N = (5, 10, 15)nH$, and are represented by solid lines, while the ideal cases are represented by dashed lines. (a) Resistance. (b) Reactance.	49
3.11	Impedance of the unloaded loop simulated by HFSS (red line), as compared to the analytically calculation (blue line). Here, we use (a) log-scale resistance and (b) reactance with linear-scale frequency to give a more clear demonstration.	50

3.12	(a) Stability constraint of the NIC load in the impedance space. As before, a three dimensional space is depicted where the x-axis is frequency s , the y-axis is phase PM in degree, and z-axis is magnitude GM in dB. The simulated impedance of the practical NIC circuit are plotted. (b) Magnification of the stability constraint around the intersection region. It is shown that the impedance profiles for both the $10nH$ (red curve) and $15nH$ (green curve) cases penetrate the forbidden region, which means they are unstable, whereas the $5nH$ case (blue curve) is stable because there is no intersection with the forbidden region.	51
3.13	(a) Real and (b) imaginary parts of the effective permeability. For the $L_N = (5, 10, 15)nH$, the simulation results are plotted with dashed lines whereas the ideal cases are solid. From these results we can see that a stable MNG performance may be achieved over a relatively large frequency bandwidth (for the $L_N = 5nH$), which are not present in the corresponding ideal case. Moreover, it is shown that the magnetic gain ($Im(\mu_r) < 0$) can be achieved at certain frequencies for the simulated case due to the parasitics while the ideal case only exhibits losses ($Im(\mu_r) > 0$).	52
3.14	Dispersion characteristics of 1D infinite periodic active loop arrays. (a) The active array consist of periodic coaxial non-Foster loaded loops, where each load is defined as a parallel-RLC circuit with $R_L = -1000\Omega$, and $C_L = -2pF$, and $L_L = [-34(blue), -43(red), -44(red - dashed)]nH$. (b) The coplanar array, only replacing the load inductance by $L_L = [-32(blue), -35(red), -36(red - dashed)]nH$	54
3.15	Equivalent circuit for a transmission line loaded with 1D non-Foster loaded loop array.	56

3.16	(a) Dispersion diagrams for the model of Fig. 3.15 with (I) $q^2 = 0.6$ and $k_m \neq 0$ (blue line), (II) $q^2 = 0$ and $k_m \neq 0$ (red dashed line), and (III) $q^2 = 0.6$, $M_m = 0$ (green line). For the case (I) and (II), it is shown that two branches can be obtained, one correspond to an EM-like wave, the other to an MI-like wave. (b) The dispersion diagrams of the EM branches for all cases are again plotted, respectively.	57
3.17	(a) Real and (b) imaginary parts of the relative permeability extracted from the effective medium. The case I and II correspond to Eq. (3.20) and Eq. (3.5), respectively.	59
3.18	Transmission line model of a 1D zero-loss and broadband metamaterials.	61
3.19	The ratio of the magnitude of the currents (a) I_n (the MI wave) and (b) J_n (the EM wave) to the source current i_n under stable and unstable conditions. Once again, the parameters are generally as before, and results are computed for an array loaded with negative resistance amplifier where $R_L = -1000\Omega$, and NIC circuits, in that $C_L = -2pF$ for all cases, and $L_L = [-34(blue), -43(red), -44(green - dashed), -45(black)]nH$	64
4.1	Extracted parameters of effective medium comprising infinite loaded loops corresponding to different spacing. (a) Non-Foster loading medium, (b) Passive loading medium.	73
4.2	Equivalent circuit of a single loop with non-Foster load. The non-Foster circuits are obtained as the output of a noiseless NIC network terminated in a parallel positive RLC load Z_N . The impedance looking into the NIC output would ideally be $Z_L = -Z_N$. Shaded components indicate Johnson-Nyquist noise sources.	75

4.3	The power spectral density with the units V^2/Hz (log-scale) of noise from a single non-Foster loaded loop, as compared to a passively-loaded structure. (a) Three-dimensional plots of the PSD of the active loop with the NIC load inductance L_L changing from 0nH to -50nH while it varies from 0nH to +50nH for the positive RLC case, however having no impact on the positive C case. (b) Two-dimensional plots of the PSDs under different loading conditions, the negative inductance is varied from the stable to unstable cases.	77
4.4	The PSD of the noise in one-dimensional infinitely-periodic loop arrays with different spacings. The spacing is varied from 5mm to 20mm. (a) The active media consist of periodic axial non-Foster loaded loops, where each load is defined as a parallel-RLC circuit with $R_L = -1000\Omega$, $L_L = -30nH$, and $C_L = -2pF$ (b) The passive media consist of loops where the loads are replaced by positive capacitances $C_L = 4pF$	83
4.5	The PSD of the noise in multi-dimensional infinitely-periodic loop arrays, as compared to the single unit case. The 1D arrays consists of periodic coaxial loops with periodicity of 10mm in the x direction, while the 2D arrays have additional coplanar periodicity (25mm) in the y direction. The addition of coplanar periodicity (25mm) in the z direction results in the 3D array case. (a) Active medium consists of non-Foster loaded loops. (b) Passive medium consists of loops where the loads are replaced by positive capacitances.	85
4.6	The PSD of the noise at the central element of a finite 1D loop array, as compared to the single unit and the infinite cases. The lattice spacing is 10mm, and the number of elements varies from 11 to 21. (a) Active medium consists of non-Foster loaded loops. (b) Passive medium consists of loops where the loads are replaced by positive capacitances.	89

4.7	A system using a single active loop to connect a source R_{source} to a load R_{load} . As discussed before, the active load is a non-Foster element Z_L generated from the NIC, and equivalent to a parallel negative RLC circuit ($Z_L = R_L L_L C_L$).	90
4.8	(a) The noise figure of the system consisting of a single non-Foster's loaded loop, as compared to the passive case. As proposed before, we take the same definitions for the loop and the loads, but vary the load inductance from $L_L = -50nH$ to $L_L = 0nH$. (b) The contrast between the noise figure and the gain of the network for the actively-loaded system with discrete load inductances $L_L = -20nH$, $L_L = -30nH$ and $L_L = -40nH$	92
4.9	A system using a 1D active loop array to connect a source and a load. . .	93
4.10	The noise figure of one-dimensional non-Foster loaded loop arrays. (a) and (b) correspond, respectively, to different distances between neighboring loops and different load inductances.	96
4.11	Schematic of the circuit model of a NIC-loaded loop, as compared to the loop circuit loaded with ideal negative elements. The NIC is described by its h-parameters.	98
4.12	The real part and imaginary parts of the input impedance of the NIC-loaded loop circuit (circle symbols line) and ideal negative elements loaded circuit (solid line), respectively.	99
4.13	Schematic of the noisy network where R_0 and R_N are the two noise sources.	100
4.14	The root mean square (RMS) node noise voltage V_{out} at different frequencies. The solid blue line represents the ADS simulation results while the red circle symbols line represents the theoretical results.	101
4.15	Parts of the list of the node noise voltage V_{out} where the first column indicates the frequency, the second column shows the noise contributions are from R_0 and R_N and the third column gives the voltage value corresponding to the noise sources.	102

5.1	Realized of a magnetic wall as a dielectric layer covered with a metal ground plane and as an artificial high-impedance surfaces. (a) Without HIS texture at the upper surface and (b) With HIS texture at the upper surface. Clearly, the thickness is reduced by using textured surface. [19]	107
5.2	Cross-section of a high impedance surface [20].	108
5.3	(a) View from the top of the actively-loaded HIS based on mushroom structure. (b) View from the side.	110
5.4	Equivalent circuit parameters extracted from an unloaded HIS. (a) Grid capacitance C . (b) Grid conductance G . (c) Substrate inductance L_s . (d) Substrate resistance R_s .	114
5.5	Input impedance of an unloaded mushroom-type HIS simulated using HFSS, as compared to the circuit models. Here, two different circuit models are presented: One is the proposed accurate circuit model represented by red-dashed lines, and the other one corresponds to the simple parallel-LC circuit model represented by green-solid lines. The simulated case is plotted with blue-solid lines. (a) Resistance. (b) Reactance. Clearly, the simulation results fits the proposed circuit model very well, and disagree with the LC model.	115
5.6	Transmission-line model for modeling the wave reflection at an actively-loaded HIS. η is the free-space impedance.	116
5.7	Reflection coefficient of an unloaded mushroom-type HIS. As before, the simulated case is represented by blue-solid lines, and the proposed circuit model is represented by red-dashed lines, while the simple parallel-LC circuit model is green-solid. (a) Reflection Magnitude. (b) Reflection phase. It is evident that the reflection coefficient calculated using the proposed circuit model matches very well with the simulation results.	118
5.8	Surface TE and TM waves along a planar impedance surface.	119
5.9	Dispersion diagrams for TE and TM waves along an unloaded HIS structure based on its equivalent circuit model.	121

5.10	An active HIS loaded with negative inductors. (a) Cross-section. (b) Equivalent circuit.	123
5.11	Nyquist contours of a mushroom-type HIS loaded with negative inductors. The inductance value is varied from the unstable to the stable cases. The Routh-Hurwitz method gives a stable range of inductances at $L_L < -2.02nH$; the Nyquist method clearly agrees with that. (a) The Nyquist contours for $L_L = (-1.9 \text{ (blue)}, -2.0 \text{ (red)}, -2.1 \text{ (green)}, -2.2 \text{ (magenta)})nH$. (b) Magnification of the Nyquist contours around the -1 point. It is evident that for $L_L = (-1.9, -2.0)nH$ the systems are unstable, while for $L_L = (-2.1, -2.2)nH$ the systems are stable.	125
5.12	Simulated Nyquist stability plots of the HIS structure with NIC loads, as compared to the analytical results obtained from the circuit model. In all cases, the solid lines represent the simulation results, while the dashed line represent the analytical solution based on the circuit model. The $N = 2$ case is plotted in blue, while the $N = 3$ case is plotted in red. It is evident that in all cases the Nyquist contour does not encircle the -1 point no matter what it is from, thus conforms stability.	127
5.13	Simulated reflection phase of the actively-loaded HIS, as compared to the analytical results obtained from the circuit model. In all cases, the simulation results are plotted by solid lines, while the dashed lines represent the analytical results. Here, three cases are plotted. Case (I) (blue line) corresponds to the unloaded HIS, while case (II) (red line) and (III) (green line) correspond to the actively-loaded HIS with an increased bandwidth of 2 and 3, respectively.	128
6.1	An ideal NIC modeled as a two-port network. [5]	135
6.2	Equivalent model for a general two-port h -parameter network with an arbitrary passive load Z_L at port 2. [6]	136

6.3	General model of a non-ideal NIC compensated with additional passive lumped elements.	138
6.4	Compensated NIC with passive terminations.	140
6.5	(a) Op-amp symbol. (b) Controlled-source model. [11]	143
6.6	(a) Non-Inverting amplifier. (b) Controlled-source model. [11]	144
6.7	Topology of an op-amp based NIC.	145
6.8	Schematic of an ideal op-amp based negative capacitance circuit captured from Agilent ADS.	147
6.9	Input impedance of the NIC circuit based on an ideal op-amp simulated using ADS, as compared to the theoretical results. The simulated case is represented by blue-solid line while the theoretical case is represented by red-dashed line. (a) Resistance. (b) Reactance. It is shown that there is good agreement between both cases, although the simulated resistance exhibits some oscillations at low frequencies due to the finite gain.	147
6.10	(a) Schematic of an real op-amp based negative capacitance circuit captured from Agilent ADS. (b) Behavior model of the real op-amp based NIC circuit, where the op-amp are described as a controlled-source model with parasitical lumped elements.	149
6.11	Input impedance of the NIC circuit based on an real op-amp simulated using ADS, as compared to the theoretical cases. The simulated case is plotted with blue-solid lines, while the theoretical case (I) from Eq. (6.34) is represented by red-dashed line, and case (II) from Eq. (6.35) is green-solid. (a) Resistance. (b) Reactance. It is shown that the simulation results again match the analytical solution very well. However, it also indicates the error between the ideal and real op-amp based NICs.	151
6.12	(a) Linvill's floating OCS NIC. (b) Equivalent circuits of Linvill's floating OCS NIC. [2]	153
6.13	Schematic of a transistor based floating NIC circuit captured from Agilent ADS to achieve a negative resistance.	154

6.14	Prototype of the transistor based floating NIC circuit.	155
6.15	Measured input impedance of the floating NIC circuit, as compared to the simulation and theoretical cases. (a) Resistance. (b) Reactance.	155
6.16	Grounded NIC model based on Linvill's OCS NIC [5].	157
6.17	Small-signal equivalent circuit of the grounded NIC model.	157
6.18	Schematic of a transistor based grounded NIC circuit captured from Agilent ADS to achieve a negative parallel-RLC network.	159
6.19	Prototype of the transistor based grounded NIC circuit.	160
6.20	Measured input impedance (green-solid) of the grounded NIC circuit, as compared to the simulation (red-solid) and analytical cases (blue-solid and blue-dashed). Here, two analytical cases are given: case (I) (blue- solid) corresponds to the designed NIC circuit with load capacitance $C_L =$ $5pF$, while case (II) (blue-dashed) is an modification of case (I) to fit the measurement results, by replacing the capacitance with $C_L = 2.1pF$. (a) Resistance. (b) Reactance. (c) Smith-chart plotting.	161

List of Abbreviations

MTM	Metamaterials
LH	Left-handed
RH	Right-handed
LHM	Left-handed medium
CRLH	Composite right/left-handed
TL	Transmission line
NIC	Negative impedance converter
HIS	High impedance surface
AMC	Artificial magnetic conductor
PCB	Printed circuit board
PSD	Power spectral density
LW	Leaky wave
MNG	μ -negative
MNZ	μ -near-zero
ENG	ε -negative
ENZ	ε -near-zero
SRR	Split ring resonator
FDTD	Finite-difference time-domain
EPSC	Exponential peak stability criterion
GMPM	Gain and phase margin
ESAC	Energy source analysis consortium
MPC	Maximum peak criterion
MI	Magneto-inductive
EM	Electromagnetic

Appendix A

List of Publications

Journal Publications

1. **Yifeng Fan**, Khalid Z. Rajab, Yang Hao, “Noise analysis of broadband active metamaterials with non-Foster loads,” Journal of Applied Physics, vol.113, no.23, pp.233905, Jun 2013.
2. Khalid Z. Rajab, **Yifeng Fan**, Yang Hao, “Characterization of active metamaterials based on negative impedance converters,” Journal of Optics, vol.14, no.11, pp.114004, April 2012.
3. **Yifeng Fan**, Khalid Z. Rajab, Yang Hao, “Characterization of active high impedance surface with non-Foster loads,” IEEE Trans. Microw. Theory Tech.(to be submitted)
4. **Yifeng Fan**, Khalid Z. Rajab, Yang Hao, “Wave propagation in actively-loaded medium: towards zero-loss and broadband magnetic metamaterials,” Appl. Phys. Lett.(to be submitted)

Conference Proceedings

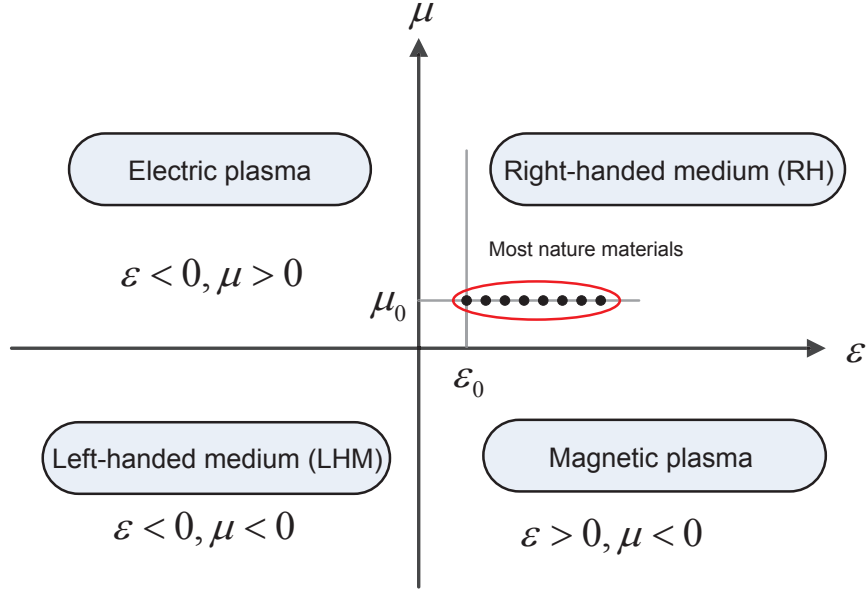
1. **Yifeng Fan**, Khalid Z. Rajab, Max Munoz, Yang Hao, “Electrically small half-loop antenna design with non-foster matching networks,” EUCAP 2012, Prague, Czech Republic, March 2012.
2. **Yifeng Fan**, Khalid Z. Rajab, Yang Hao, “Noise figure of broadband active metamaterials,” International Symposium on Electromagnetic Theory (EMTS 2013), Hiroshima, Japan, May 2013.
3. **Yifeng Fan**, Khalid Z. Rajab, Yang Hao, “Noise power of broadband active metamaterials,” APS/URSI 2013, Orlando, Florida, USA, July 2013.
4. **Yifeng Fan**, Khalid Z. Rajab, Yang Hao, “Impedance Space Stability Analysis of Engineered Metamaterials of Active Loops,” Metamaterials 13, Bordeaux, France, September 2013.
5. Khalid Z. Rajab, **Yifeng Fan**, Di Bao, Atiqur Raman, Yang Hao, “Active circuits for improved metamaterial performance,” iWAT 2011, Hong Kong, China, March 2011.

Chapter 1

Introduction

Since Veselago [1] first introduced the concept of left-handed (LH) medium with simultaneous negative permittivity (ε) and permeability (μ), the development of artificially engineered materials or metamaterials has been a subject of growing interest for both engineers and physicists due to their possible ability of designing and building novel devices [2–5]. A metamaterial is a macroscopic composite of periodic or non-periodic structure, whose function is due to both the cellular architecture and the chemical composition [6]. If the condition of effective-homogeneity is satisfied, the structure behaves as a real material in the sense that electromagnetic waves are essentially myopic to the lattice and only probe the average, or effective, macroscopic and well-defined constitutive parameters, which depend on the nature of the unit cell; the structure is thus electromagnetically uniform along the direction of propagation [7]. The constitutive parameters are the permittivity ε and the permeability μ , which are related to the refractive index n by

$$n = \pm\sqrt{\varepsilon_r\mu_r}, \quad (1.1)$$

Figure 1.1: Materials in the ε - μ domain [7].

where ε_r and μ_r are the relative permittivity and permeability related to the free space permittivity and permeability by

$$\varepsilon_0 = \varepsilon/\varepsilon_r = 8.854 * 10^{-12} F/m, \quad \mu_0 = \mu/\mu_r = 4\pi * 10^{-7} N * A^{-2}$$

respectively. In Eq. (1.1), sign \pm for the double-valued square root function has been a priori admitted for generality.

The four possible sign combinations in the pair (ε, μ) are $(+, +)$, $(+, -)$, $(-, +)$, and $(-, -)$, as illustrated in the $\varepsilon - \mu$ diagram of Figure 1.1. Whereas the first combination is well known as conventional right-handed (RH) materials, the other three, with either negative permittivity or permeability, correspond to electric plasma, magnetic plasma and left-handed medium (LHM), respectively.

LH structures are clearly metamaterials, according to the definition given above, since they are artificial, effectively homogeneous, and exhibit highly unusual properties ($\varepsilon_r, \mu_r < 0$). It should be noted that, although the term “metamaterial” has been used most often in reference to LH structures in the literature, metamaterials may encompass

a much broader range of structures. For example, structures with only one of the two constitutive parameters negative in addition to many existing materials obtained by novel nanotechnology and chemistry progress can be regarded as metamaterials [7].

The unique properties of metamaterials have allowed novel applications, concepts, and devices to be developed. There are many novel properties, such as negative refraction, backward waves, novel dispersion diagrams, to name just a few. These properties have already been utilized in a number of different applications, such as the super-lens [3], cloaks [4], novel antennas [7], microwave components and so on.

1.1 Research Objectives and Methodology

As proposed by Caloz *et al.* [8, 9], one of the important application of metamaterials is leaky wave (LW) antenna design which is based on the composite right/left handed (CRLH) transmission line (TL) theory. However, the frequency-dependent nature of LW antennas does limit the application of the CRLH LW antenna in modern communication system, which generally requires fixed-beam operation for effective channelizing. In our work, a varactor-controlled leaky-wave (LW) antenna based on the tuneable CRLH TL structure incorporating varactor diodes for dynamic-frequency voltage-controlled operation will be proposed which could perform a broadband beam-fixing function. In addition, scanning from forward to backward at a fixed frequency can be achieved by manipulating the biasing voltage applied to the varactors.

Due to the dispersive nature of passive materials, most of metamaterial-based devices are often narrowband and lossy [10, 11]. Particularly for near-zero or negative-valued material properties (ε or μ), which occur due to resonance in passive materials, this highly dispersive nature can be quite overwhelming too, and significantly degrades the performance of a device. In this thesis, the methodology for research and design of active metamaterials which can overcome these inherent limitations will be presented. In order to enable low-loss and broadband metamaterials, initial experimental effort have shown

that the concept can be made to work [12–14]. However, due to the basic underlying physics of energy stored with passive material, their claimed “broadband properties” are actually very frequency restricted [15]. Recently, new approaches based on active devices such as non-Foster circuits [16–19], power amplifiers [20–22], and tunnel diodes [23], have been proposed and experimentally verified as a means to overcome these problems. Metamaterials based on non-Foster circuits are particularly interesting and have shown significant potential to advance negative permeability-based applications [17, 24, 25], where non-Foster circuit elements are negative lumped elements realized by negative impedance converters (NICs). However, as any active device, there are bottlenecks associated with the implementation of NIC-loaded metamaterials that have delayed their application, one is the possibility of instability, and the other is the noise issue.

In Ref. [25], the Routh-Hurwitz [26], [27] technique was used to derive the range of lumped element parameters for which the ideally NIC-loaded loop array structure will be stable. The drawback with this approach is that in practice a NIC circuit is not a perfect negative lumped element component. A two-pole lumped element model may only have limited accuracy, and parasitic elements in the circuit will limit performance beyond a certain frequency. For this purpose, it is preferable to use a frequency-domain stability criterion in which the measured performance of an NIC circuit can be used along with the effective medium to examine stability. For this purpose, the application of Nyquist stability criterion has been proposed based on the fact that the signal stability at a given operating point can be determined by examining the Nyquist contour [28].

Although the Nyquist criterion is capable of testing the stability for practical NIC-loaded medium, one disadvantage associating with this analysis method is that it is not design oriented. For example, it only tests the stability of a single operating point, unable to provide the design specifications. Hence, an impedance/admittance based approach which can overcome the limitations of Nyquist stability criterion will be presented and applied to the design of active broadband magnetic metamaterials. In essence, this is a

method of transforming the forbidden region into a load admittance (source impedance) specification for a given source impedance (load admittance). Similar as [29], there are two aspects to this method, which can be employed separately or together. First, a new stability criterion named as Exponential Peak Stability Criterion (EPSC) will be developed to ensure robust stability, which is less artificially conservative than the heretofore available methods and at the same time is less sensitive to component grouping. In addition, it can be used to explicitly address operating points and parameter variations. As for demonstration, a sample NIC-loaded material has been implemented and simulated to provide an accurate portrayal of the stability of these active metamaterials, as well as the broadband material properties. Finally, the wave propagation in active metamaterials with non-Foster loads has been investigated in terms of its dispersion characteristics. Moreover, we will demonstrate how powered active unit cells incorporating both NICs and amplifiers can compensate the loss of the effective medium while maintaining the broadband magnetic properties. Thus, the way to achieve zero-loss and broadband active metamaterials will be analytically provided.

Another important factor in the design of active metamaterials is the noise performance which still remains to be explored. In addition to the Johnson-Nyquist noise from lossy conductors, active devices used for the design of NIC circuits will give rise to noise as well. In this thesis, a general analytical model is developed for the prediction of the noise performance of broadband, stable active metamaterials based on ideal NIC circuits.

High Impedance surface (HIS) or artificial magnetic conductor (AMC) is a type of two-dimensional (2D) metamaterial that exhibits the performance of perfect magnetic conductors (PMCs) over a limited frequency band [30, 31]. Although there has been an extensive amount of research conducted with the aim to increase their bandwidth, non-Foster loading has been suggested as an effective means to greatly enhance the bandwidth [32, 33]. However, only very basic considerations were given to the stability analysis for these actively-loaded HIS structures, while their characteristics such as the

reflection properties and surface waves propagation still remain unexplored. In our work, the characterization of active HIS with non-Foster loads will be presented based on the equivalent circuit model of a normal unloaded HIS. Moreover, the way to achieve a broadband active HIS whilst maintaining the stability will be analytically provided by applying the Routh-Hurwitz technique.

Following the investigation on different types of active metamaterials, the practical NIC design will be introduced and demonstrated at last, as the main challenge to achieve a successful design of non-Foster loaded metamaterial structure.

1.2 Organization of the Thesis

In **Chapter 2**, the fundamental electromagnetic properties of metamaterials and the physical realization of these materials are reviewed based on a general TL approach. The general TL approach provides an insight into the physical phenomena of LHMs and provides an efficient design tool for LH applications. LHMs are considered to be a more general model of CRLH structures, which also include right-handed (RH) effects that occur naturally in practical LHMs. Furthermore, an electronically controlled CRLH leaky-wave antenna will be proposed and designed which can perform a fixed beam function at different frequencies as well as tunable bandwidth by tuning the biasing voltage.

Chapter 3 give a detailed investigation of active metamaterials with non-Foster loads. First, several stability criteria are proposed to maintain the stability for a NIC-loaded effective magnetic material, in order to enhance the negative- $\text{Re}(\mu)$ (MNG) or μ -near-zero (MNZ) regions. Subsequently, the wave propagation in the actively-loaded medium is investigated using the TL approach. By inspection of the relation between the wave propagation and the effective medium properties, an analytical design of a zero-loss and broadband metamaterials by incorporating the NIC circuits and negative resistance amplifiers is provided.

In **Chapter 4**, the noise performance, represented as the Power Spectral Density (PSD) and Noise Figure (NF), of broadband metamaterials is analyzed in relation to stability, and the effective material properties. All noise parameters of active metamaterials will be presented in comparison with their passive counterparts.

Chapter 5 presents the design of active high impedance surfaces (HIS) with non-Foster loads which can overcome the physical limitations of passive HIS, thus greatly increase the bandwidth. Based on the equivalent circuit model, the stability of active HIS is investigated to derive the stability bounds for the load components. The application to design of broadband HIS is given and verified by full-wave simulations.

Chapter 6 describes the design of negative impedance converters (NICs) which is the key part of designing of active magnetic metamaterials and active HIS. Based on the different active inclusions, the NIC circuit can be classified by two categories: one is the operational amplifier (op-amp) based NIC and the other is based on discrete transistors. For the op-amp based NIC, we only give the simulation results since it is shown that the real op-amps are seriously limited by their non-ideal properties, thus affecting the NIC performance. However, we have experimentally designed and built two types of transistor based NIC, one is the floating NIC on the breadboard and the other is the grounded NIC fabricated on the printed circuit board (PCB). The measurement results of both circuits have verified the circuit designs.

Finally in **Chapter 7**, the summary of the dissertation and possible future work is presented. Potential future work includes the practical realization of active magnetic metamaterials and active HIS.

1.3 Contribution of the Thesis

The key contributions of the work presented in this thesis can be summarized as follows:

- Several techniques are explored for analyzing the stability of the actively-loaded

medium. In particular, a novel immitance-based stability criterion named EPSC is proposed and applied to the practical design of broadband active metamaterials.

- A general analytical model is developed for the prediction of the noise performance of broadband, stable active metamaterials based on negative impedance converters (NICs).
- A detailed investigation on the characterization of active high impedance surface (HIS) with non-Foster loads is provided.
- A broadband zero-loss magneto-inductive transmission structure has been proposed.

References

- [1] V. G. Veselago, “The electrodynamics of substances with simultaneously negative values of ε and μ ,” *Sov. Phys. USPEKHI*, vol. 10, pp. 509–514, 1968.
- [2] D. R. Smith, W. J. Padilla, D. C. Vier, S. C. Nemat-Nasser, and S. Schultz, “Composite medium with simultaneously negative permeability and permittivity,” *Phys. Rev. Lett.*, vol. 84, pp. 4184–4187, 2000.
- [3] J. Pendry, “Negative refraction makes a perfect lens,” *Phys. Rev. Lett.*, vol. 85, pp. 3966–3969, 2000.
- [4] D. Schurig, J. J. Mock, B. J. Justice, S. A. Cummer, J. B. Pendry, A. F. Starr, and D. R. Smith, “Metamaterial electromagnetic cloak at microwave frequencies,” *Science*, vol. 314, pp. 977–980, 2006.
- [5] R. Shelby, D. R. Smith, and S. Schultz, “Experimental verification of a negative index of refraction,” *Science*, vol. 292, pp. 77–79, 2001.
- [6] T. J. Cui, D. Smith, and R. Liu, *Metamaterials: Theory, Design and Applications*. Springer, 2010.
- [7] C. Caloz and T. Itoh, *Electromagnetic Metamaterials: Transmission Line theory and Microwave Applications*. NJ: Wiley-Interscience publication, 2006.

- [8] —, “Transmission line approach of left-handed (*lh*) materials and microstrip implementation of an artificial *lh* transmission line,” *IEEE Trans. Antennas Propag.*, vol. 52, pp. 1159–1166, May. 2004.
- [9] C. Caloz, A. Sanada, and T. Itoh, “A novel composite right/left-handed coupled-line directional coupler with arbitrary coupling level and broad bandwidth,” *IEEE Trans. Microwave Theory Tech.*, vol. 52, pp. 980–992, Mar. 2004.
- [10] M. I. Stockman, “Criterion for negative refraction with low optical losses from a fundamental principle of causality,” *Phys. Rev. Lett.*, vol. 98, p. 177404, 2007.
- [11] B. Nistad and J. Skaar, “Causality and electromagnetic properties of active media,” *Phys. Rev. E*, vol. 78, p. 036603, 2008.
- [12] T. Campbell, A. Hibbins, J. Sambles, and I. Hooper, “Broadband and low loss high refractive index metamaterials in the microwave regime,” *Appl. Phys. Lett.*, vol. 102, p. 091108, 2013.
- [13] S. Rudolph, C. Pfeiffer, and A. Grbic, “Design and free-space measurements of broadband, low-loss negative-permeability and negative-index media,” *IEEE Trans. Antennas Propag.*, vol. 59, pp. 2989–2997, 2011.
- [14] J. Valentine, S. Zhang, T. Zentgraf, and X. Zhang, “Development of bulk optical negative index fishnet metamaterials: Achieving a low-loss and broadband response through coupling,” *Proceedings of the IEEE*, vol. 99, pp. 1682–1690, 2011.
- [15] S. Hrabar, I. Koris, I. Krois, and A. Kirichenko, “Negative capacitor paves the way to ultra-broadband metamaterials,” *Appl. Phys. Lett.*, vol. 99, p. 254103, 2011.
- [16] D. J. Gregoire, C. R. White, and J. S. Colburn, “Wideband artificial magnetic conductors loaded with non-foster negative inductors,” *IEEE Antennas and Wireless Propagat. Lett.*, vol. 10, pp. 1586–1589, 2011.
- [17] S. Saadat, M. Adnan, H. Mosallaei, and E. Afshari, “Composite metamaterial and metasurface integrated with non-foster active circuit elements: A bandwidth-enhancement investigation,” *IEEE Trans. Antennas Propag.*, vol. 61, pp. 1210–1218, 2013.
- [18] N. Zhu and R. W. Ziolkowski, “Broad-bandwidth, electrically small antenna augmented with an internal non-foster element,” *IEEE Antennas and Wireless Propa-*

- gat. Lett.*, vol. 11, pp. 1116–1120, 2012.
- [19] M. Barbuto, A. Monti, F. Bilotti, and A. Toscano, “Design of a non-foster actively loaded srr and application in metamaterial-inspired components,” *IEEE Trans. Antennas Propag.*, vol. 61, pp. 1219–1227, 2013.
 - [20] Y. Yuan, B. Popa, and S. A. Cummer, “Zero loss magnetic metamaterials using powered active unit cells,” *Opt. Exp.*, vol. 17, p. 16135, 2009.
 - [21] L. Jelinek and J. Machac, “An fet-based unit cell for an active magnetic metamaterial,” *IEEE Antennas and Wireless Propag. Lett.*, vol. 10, pp. 927–930, 2011.
 - [22] R. Syms, L. Solymar, and I. Young, “Three-frequency parametric amplification in magneto-inductive ring resonators,” *Metamaterials*, vol. 2, pp. 122–134, 2008.
 - [23] T. Jiang, K. Chang, L. Si, L. Ran, and H. Xin, “Active microwave negative-index metamaterial transmission line with gain,” *Phys. Rev. Lett.*, vol. 107, p. 205503, 2011.
 - [24] S. Tretyakov, “Meta-materials with wideband negative permittivity and permeability,” *Microwave Opt. Technology Lett.*, vol. 31, pp. 163–165, 2001.
 - [25] K. Z. Rajab, Y. Hao, D. Bao, C. G. Parini, C. Vazquez, J. Philippakis, and M. Philippakis, “Stability of active magnetoinductive metamaterials,” *J. Appl. Phys.*, vol. 108, p. 054904, 2010.
 - [26] E. J. Routh, *A Treatise on the Stability of a Given State of Motion, Particularly Steady Motion*. London: Macmillan and Co., 1877.
 - [27] A. Hurwitz, “On the conditions under which an equation has only roots with negative real parts,” *Selected Papers on Mathematical Trends in Control Theory (R. Bellman and R. Kalaba, eds.)*, vol. 65, 1964.
 - [28] K. Z. Rajab, Y. Fan, and Y. Hao, “Characterization of active metamaterials based on negative impedance converters,” *J. Opt.*, vol. 14, p. 114004, 2012.
 - [29] S. Sudhoff, S. Glover, P. Lamm, D. H. Schmucker, and D. Delisle, “Admittance space stability analysis of power electronic systems,” *Aerospace and Electronic Systems, IEEE Transactions on*, vol. 36, no. 3, pp. 965–973, 2000.
 - [30] D. Sievenpiper, L. Zhang, R. Broas, N. Alexopolous, and E. Yablonovitch, “High-impedance electromagnetic surfaces with a forbidden frequency band,” *IEEE Trans.*

- Microw. Theory Tech.*, vol. 47, pp. 2059–2074, 1999.
- [31] F. Costa, S. Genovesi, and A. Monorchio, “On the bandwidth of high-impedance frequency selective surfaces,” *IEEE Antennas Wireless Propag. Lett.*, vol. 8, pp. 1341–1344, 2009.
- [32] D. J. Gregoire, C. R. White, and J. S. Colburn, “Wideband artificial magnetic conductors loaded with non-foster negative inductors,” *IEEE Antennas Wireless Propag. Lett.*, vol. 10, pp. 1586–1589, 2011.
- [33] D. Kern, D. Werner, and M. Wilhelm, “Active negative impedance loaded ebg structures for the realization of ultra-wideband artificial magnetic conductors,” in *Antennas and Propagation Society International Symposium, 2003. IEEE*, vol. 2, 2003, pp. 427–430 vol.2.

Chapter 2

Research on Tuneable Leaky Wave Antennas

This chapter gives a literature review of the fundamental properties of left-handed (LH) metamaterials and the generalized composite right/left-handed (CRLH) concept based on the transmission line (TL) approach. The equivalent circuit model is developed and a CRLH-based electronically controlled metamaterial structure is presented and demonstrated as a novel leaky-wave (LW) antenna which can fix the radiation pattern at different frequencies. Finally, A 12-cell voltage controlled LW antenna was designed and tested.

2.1 Overview of TL Structure

TL theory has long been a powerful analysis and design tool for conventional (*i.e.*, RH) materials. By modeling a CRLH metamaterial as an equivalent TL, TL theory can be used to analyze and design one-, two-, or even three-dimensional CRLH metamaterials. In the following sections, the TL approach to CRLH metamaterials will be developed.

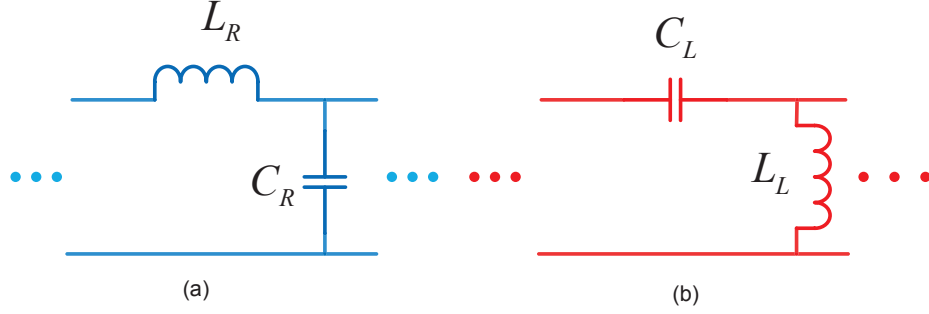


Figure 2.1: Transmission line circuit model unit-cells. (a) RH transmission line unit-cell. (b) LH transmission line unit-cell.

As proposed by Caloz *et al.* [1], conventional transmission lines can be modeled as unit-cells with series inductance (L_R) and shunt capacitance (C_R), whilst LH transmission lines are modeled as unit cells with capacitance (C_L) and shunt inductance (L_L) as shown in Fig. 2.1. The propagation constants (wave number) for the RH and LH unit-cell are given by

$$\begin{aligned}\beta_{RH} &= \omega\sqrt{C_R L_R} \\ \beta_{LH} &= -\frac{1}{\omega\sqrt{C_L L_L}}.\end{aligned}\tag{2.1}$$

By plotting a $\omega - \beta$ diagram, commonly referred to as a dispersion diagram, the group velocity ($v_g = \partial\omega/\partial\beta$) and phase velocity ($v_p = \omega/\beta$) of a TL circuit model can be directly observed. The dispersion diagrams for the unit-cell of Fig. 2.1 are plotted in Fig. 2.2, respectively. For comparison, the propagation constant of the light line in free space is also plotted

$$k_0 = \omega\sqrt{\mu_0\varepsilon_0},\tag{2.2}$$

where $\mu_0 = 4\pi \bullet 10^{-7}$ and $\varepsilon_0 = 8.854 \bullet 10^{-12}$ are the free space permeability and permittivity.

The dispersion diagrams show that v_g and v_p of the RH transmission line have the

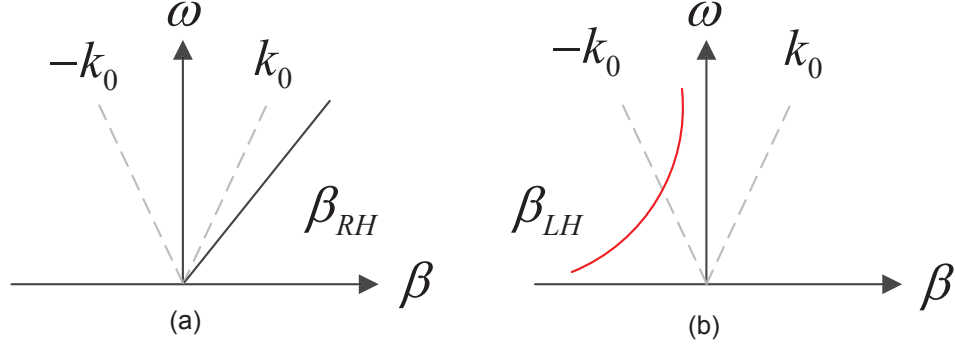


Figure 2.2: Dispersion diagrams for the unit-cells shown in Fig. 2.1. (a) RH unit-cell (black-solid). (b) LH unit-cell (red-solid). It is shown that the RH structure has a linear dispersion diagram while a LH structure has a non-linear slope.

same sign ($v_g v_p > 0$), whilst v_g and v_p for a LH TL are opposite ($v_g v_p < 0$). Therefore, a RH transmission line supports a forward wave, while a LH transmission line supports a backward wave. In addition, the dispersion diagram of LH TL shows that v_g approaches infinity as ω increases. However, this is not physically possible since it violates Einstein's special theory of relativity. This means that a pure LH transmission line is not possible. Instead, the unit-cell model of Fig. 2.2 (b) has to be modified to account for unavoidable parasitic effects with any practical realization of a LH transmission line. To see what these parasitic effects are, let's consider a distributed realization of a RH and LH transmission line. A RH microstrip line is shown in Fig. 2.3(a) and consists of a ground plane and trace separated by a dielectric substrate. The current flow along the trace of the microstrip line gives rise to a series inductance, while the voltage gradient between the trace and ground plane gives a rise to a shunt capacitance. Therefore, the RH unit-cell circuit model can accurately model a RH transmission line. Fig. 2.3(b) is a microstrip implementation of a transmission line, which is based on the Sievenpiper mushroom unit-cell [2]. The edge coupling between adjacent metal patches contributes to the series capacitance, while the via connecting the patch to the ground plane provides the required shunt inductance. Besides these LH contributions, RH parasitic effects also occur with the implementation of the LH transmission line; series inductance due to current flow on the metal patch and shunt capacitance from the voltage gradient between

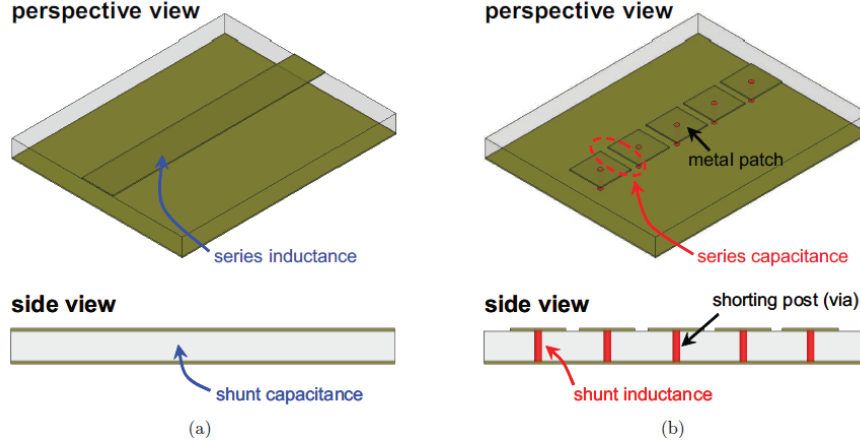


Figure 2.3: Distributed realization of unit-cell shown in Fig. 2.1. (a) RH microstrip transmission line. (b) LH microstrip transmission line consisting of periodic cascade of Sievenpiper mushroom unit-cells.[2]

the metal patch and the ground plane. Therefore, the LH unit-cell circuit model of Fig. 2.1 (b) does not take into account the unavoidable RH effects that occur with any practical realization of a LH transmission line.

2.2 Theory of CRLH TL Metamaterials

A pure LH transmission line cannot be physically realized due to RH parasitic effects. As a result, a LH transmission line should be described using a more general model of a composite right/left-handed (CRLH) transmission line, which also includes RH attributes. The general model of a CRLH-TL is shown in Fig. 2.4 (a) and consists of a series inductance L_R , a series capacitance C_L , a shunt capacitance C_R , and a shunt inductance L_L . The propagation constant of a TL is given by [3]

$$\gamma = \alpha + j\beta = \sqrt{ZY}, \quad (2.3)$$

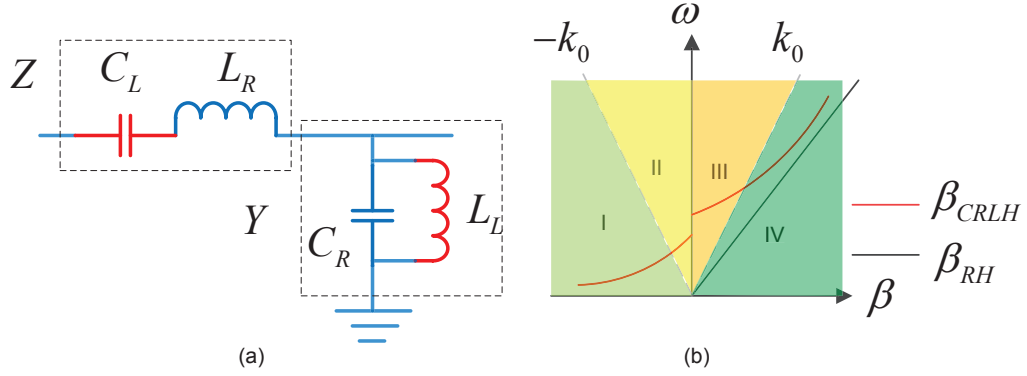


Figure 2.4: CRLH transmission line. (a) Circuit model of an unit-cell. (b) General dispersion diagram for unbalanced case. Based on the light line ($\pm k_0$), the whole region is divided into four parts plotted by different colors, indicating the different wave propagation phenomena.

where Z and Y are, respectively, the serial impedance and shunt admittance. In the particular case of the CRLH-TL, Z and Y are defined as

$$\begin{aligned} Z &= j(\omega L_R - \frac{1}{\omega C_L}) \\ Y &= j(\omega C_R - \frac{1}{\omega L_L}) \end{aligned} \quad (2.4)$$

Thus, in the lossless case ($\alpha = 0$), the phase constant (β) for the CRLH unit-cell is given by

$$\beta_{CRLH} = s(\omega) \sqrt{\omega^2 L_R C_R + \frac{1}{\omega^2 L_L C_L} - (\frac{L_R}{L_L} + \frac{C_R}{C_L})}, \quad (2.5)$$

where

$$s(\omega) = \begin{cases} -1 & \text{if } \omega < \omega_{\Gamma 1} = \min(\omega_{se}, \omega_{sh}), \\ 1 & \text{if } \omega > \omega_{\Gamma 2} = \max(\omega_{se}, \omega_{sh}). \end{cases} \quad (2.6)$$

by defining the series and shunt resonance frequencies

$$\omega_{se} = \frac{1}{\sqrt{L_R C_L}}, \quad (2.7)$$

$$\omega_{sh} = \frac{1}{\sqrt{L_L C_R}}. \quad (2.8)$$

The dispersion diagram for an unbalanced CRLH unit-cell is shown in Fig. 2.4 (b). In general, the series resonance (ω_{se}) and the shunt resonance (ω_{sh}) are not equal and a stop-band occurs between the transmission from LH to RH propagation, this is referred to as the unbalanced case. In the balanced case, $\omega_{se} = \omega_{sh}$ and a seamless transition from LH to RH propagation happens. The CRLH dispersion diagram shows that it supports a backward wave at low frequencies and forward wave at high frequencies relative to ω_{se} and ω_{sh} . In addition, the dispersion diagram for a RH transmission line is overlaid on Fig. 2.4(b) to illustrate the unique properties of the CRLH transmission line:

- RH transmission line has a linear slope, while a CRLH transmission line has a non-linear slope. Furthermore, it also shows that the CRLH dispersion curves tends to the LH and RH dispersion curves at low and high frequencies, respectively.
- Since the phenomenon of Vavilov-Čerenkov radiation is fundamentally similar to the phenomenon of leakage radiation in traveling-wave antennas [1], the CRLH transmission structure can be used in the design of leaky-wave antennas. From this point of view, radiation can occur only at frequencies where the phase velocity is larger than the speed of light (fast-wave region II and III where $v_p > c = 1/\sqrt{\mu_0\epsilon_0}$, i.e., region $|\beta| < k_0$). In contrast, the wave will be purely guided along the TL structure without radiation when the dispersion lies in the slow-wave region (region I and IV, where $\beta > k_0$).

2.3 General Leaky-Wave Antenna Structure

Leaky wave antennas are a form of travelling wave antennas with their electromagnetic field excited by a wave incident in the interior of the guiding structure. As the wave propagates down the guiding structure, some of its energy leaks out; this leaky energy power translates to far-field radiation. Any residual guided energy is simply lost to a matched load at the other end of the leaky-wave antenna. The general model of a leaky-wave antenna is shown in Fig. 2.5 (a) and its principle of operation in Fig. 2.5 (b).

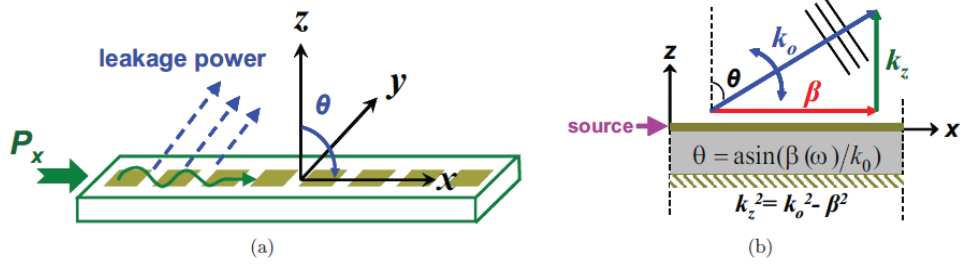


Figure 2.5: Leaky wave antenna. (a) Concept. (b) Principle of operation. θ is the radiation angle with respect to the axis z , while k_z is the perpendicular propagation constant for radiation, related to the free space wave number k_0 and the propagation constant of the travelling wave β . [4]

Fig. 2.5 (b) shows that by changing the frequency, the propagation constant of the traveling wave changes and the radiated beam is scanned. However, conventional leaky-wave antennas require complex feeds to excite a higher-order mode for radiation, since in order for leakage to occur k_z has to be real, where k_z is the propagation constant perpendicular to the traveling wave direction ($k_z^2 = k_0^2 - \beta^2$) [5]. This can be seen by looking at the dispersion curve of Fig. 2.4 (b) for a RH transmission line, whose dispersion diagram is in the slow-wave region ($v_p < c$, or $\beta > k_0$), the perpendicular propagation constant k_z becomes imaginary, thus there is exponential decay along z direction away from the interface, which means only guided wave occur. In contrast, when the dispersion curve of a CRLH transmission line lies in the fast-wave region ($|\beta| < k_0$), the perpendicular propagation constant is real, which leads to the leaky radiation. The region of the dispersion diagram where the condition $|\beta| < k_0$ is called the radiation region as represented in Fig. 2.4 (b). Any traveling wave structure whose dispersion curves intersecting with the radiation region is a leaky-wave structure. This means that a CRLH transmission line structure can be used as a dominant mode leaky-wave antenna since its radiating mode lies below the cutoff of higher order modes [1]. Furthermore, due to the combination of RH and LH structures, CRLH leaky antennas are capable of both backward ($-90^\circ < \theta < 0^\circ$) and forward ($0^\circ < \theta < 90^\circ$) scanning

[5]. In the case of a balanced CRLH transmission line, a seamless transition from LH to RH operation occurs resulting in a β of zero with non-zero group velocity. Therefore, a balanced CRLH transmission line can also scan broadside ($\theta = 0^\circ$). The ability to scan continuously from backward to forward under the dominant-mode is only possible with a balanced CRLH transmission line.

A typical CRLH unit-cell for realizing the leaky wave antenna is shown in Fig. 2.6. This unit-cell is based on microstrip technology; the LH series capacitance (C_L) is provided by the interdigital capacitor, while the LH shunt inductance (L_L) is provided by the shorted stub. The RH series inductance (L_R) and shunt capacitance (C_R) are provided by the current and voltage gradient across the interdigital capacitor, respectively.[5]

There are several advantages of the CRLH TL-based LW antenna as compared to its conventional counterparts. Conventional LW antennas operate at their higher-order modes and are limited to scanning only at forward or backward angles, but not at broadside. However, the CRLH LW antenna offers the ability of scanning both the backward and the forward directions, as well as at broadside. Characterization of such an antenna in terms of unit-cell properties and substrate permittivity is given in [6–8]. Further more, since the CRLH LW antenna operates at its dominant mode, it can easily be excited with the use of a simple microstrip feed.

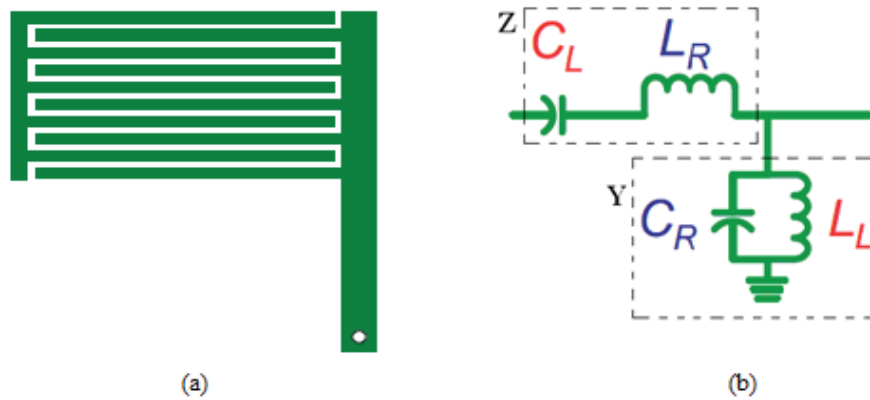


Figure 2.6: Typical CRLH unit cell. (a) Physical size. (b) Equivalent circuit.[4]

2.4 Electronically Controlled Fixed-Beam Leaky-Wave Antenna Design

The fixed-frequency beam steering TL-based LW antennas have been reported.[9, 10] However, the frequency-dependent nature of LW antennas does limit the application of the CRLH LW antenna in modern communication system, which generally requires fixed-beam operation for effective channelizing. Hence, a voltage controlled leaky-wave antenna based on tuneable CRLH transmission line structure is presented here which gives the solution to this problem. Incorporating varactor diodes for dynamic-frequency voltage-controlled operation, this antenna can be tuned to radiate at a fixed angle at different frequencies, effectively demonstrating broadband characteristics. The fabricated prototype antenna comprises of 12 cells and employs varactors in the shunt branch only. The antenna exhibits a fixed beam from 1.8 GHz to 2.8 GHz, while offering a bandwidth of more than 40%. A maximum gain of 6.5 dBi is measured for this antenna.

2.4.1 Principle of Voltage Controlled Leaky-Wave Antenna

For a leaky-wave antenna application, the radiation angle of the main beam is determined by the following simplified relation in the dominant mode ($n = 0$) [5]

$$\theta = \sin^{-1}\left(\frac{\beta_0 + 2n\pi/d}{k_0}\right) = \sin^{-1}\left(\frac{\beta_0}{k_0}\right), \quad (2.9)$$

where β_0 is the propagation constant of the traveling wave in the dominant mode, k_0 is the free space wave number. It was shown in Section 2.2 that a dispersion curve can be plotted using parameters extracted from an equivalent circuit. Therefore, the scanning angle of an CRLH leaky-wave antenna is dependent on its corresponding circuit parameters. In general, the distributed inductance and capacitance values are fixed once the physical size of a CRLH transmission line structure is determined, which leads to a beam shift when the frequency varies. However, if the circuit parameters can be

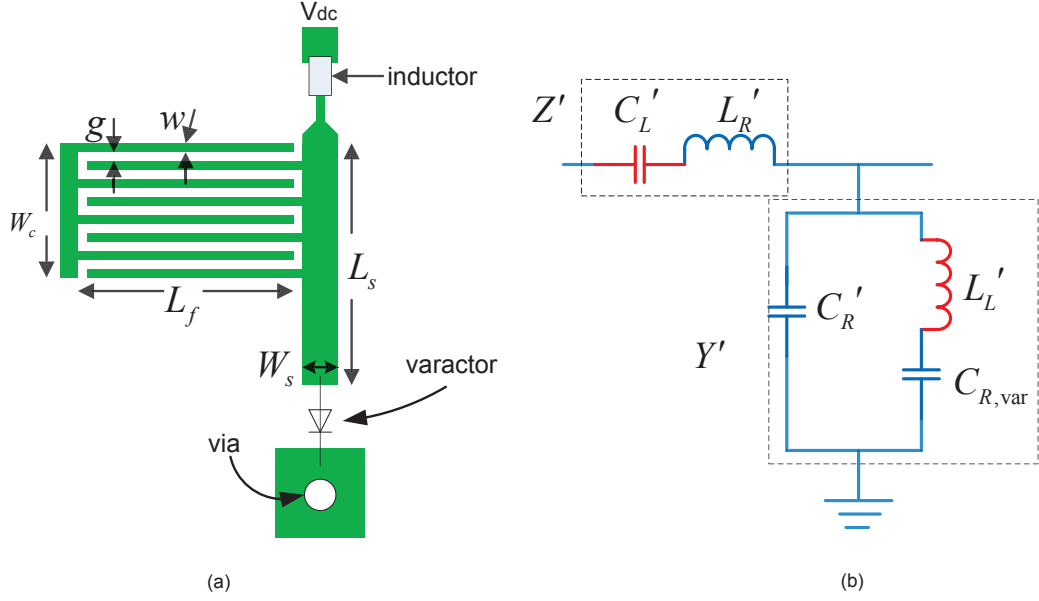


Figure 2.7: A novel voltage-controlled CRLH leaky-wave antenna. (a) Layout of a single unit cell. (b) Equivalent circuit model.

manipulated by voltages, then the same radiation pattern can be gained at different frequencies.

The proposed structure includes nonlinear devices (varactors) is shown in Fig. 2.7 (a). Thus, we need to investigate the varactor effects to the antenna radiation. Fig. 2.7 (b) shows the equivalent circuit model of the unit cell. The parameters of the circuit model which consists of a series RH inductance L'_R , a series LH capacitance C'_L , a shunt RH capacitance C'_R , and one shunt LH inductance L'_L can be extracted from S parameters obtained from a full-wave simulation. Here, the varactor diode is simply modeled as a single capacitance C_{var} .

In a similar manner, the per-unit length impedance Z' and per-unit length admittance Y' is modified from Eq. (2.4) to be

$$\begin{aligned} Z' &= j \left(\omega L'_R - \frac{1}{\omega C'_L} \right), \\ Y' &= j \left(\omega C'_R - \frac{1}{\omega L'_L - \frac{1}{\omega C_{var}}} \right). \end{aligned} \quad (2.10)$$

The phase constant β' for this novel voltage controlled CRLH unit-cell is given from Eq. (2.3) by

$$\beta' = s'(\omega) \sqrt{\left(\omega L'_R - \frac{1}{\omega C'_L}\right) \left(\omega C'_R - \frac{1}{\omega L'_L - \frac{1}{\omega C_{var}}}\right)}, \quad (2.11)$$

and the series and shunt resonance frequencies can also be obtained

$$\omega'_{se} = \frac{1}{\sqrt{L'_R C'_L}}, \quad (2.12)$$

$$\omega'_{sh} = \sqrt{\frac{C'_R + C_{var}}{L'_L C'_R C_{var}}}, \quad (2.13)$$

respectively. Similar to the conventional CRLH case discussed before, $s'(\omega)$ has the following sign function

$$s'(\omega) = \begin{cases} -1 & \text{if } \omega < \omega_{\Gamma 1} = \min(\omega'_{se}, \omega'_{sh}), \\ 1 & \text{if } \omega > \omega_{\Gamma 2} = \max(\omega'_{se}, \omega'_{sh}). \end{cases} \quad (2.14)$$

As suggested in [1], the sign function depends on the signs of the phase velocity v_p and group velocity v_g : when $\omega < \min(\omega'_{se}, \omega'_{sh})$, v_p and v_g have opposite signs, it means that the transmission line is LH and therefore β' is negative. In contrast, if the RH range $\omega > \max(\omega'_{se}, \omega'_{sh})$, v_p and v_g have the same sign, hence the transmission line is RH, which leads to positive β' .

As the capacitance of the varactor depends uniquely on the reverse-biasing voltage, it can be described by

$$C_{var} = f(V). \quad (2.15)$$

Thus, the scanning angle may be modified from the expression in Eq. (2.9) to include its voltage-dependance,

$$\theta(V) = \sin^{-1}\left(\frac{\beta'(V)}{k_0}\right). \quad (2.16)$$

From Eq. (2.11), (2.16) and (2.15), we can conclude that at a fixed radiation, angle θ the reverse-biasing voltage can be described as a function of the frequency

$$V(\omega) = f^{-1}\left(\frac{N(\omega)}{M(\omega)}\right), \quad (2.17)$$

where

$$\begin{aligned} N(\omega) &= k_0^2 \sin^2 \theta - \omega C'_R \left(\omega L'_R - \frac{1}{\omega C'_L} \right), \\ M(\omega) &= \omega^2 L'_L \left(k_0^2 \sin^2 \theta - \omega C'_R \left(\omega L'_R - \frac{1}{\omega C'_L} \right) \right) + \omega^2 L'_R - \frac{1}{C'_L}. \end{aligned} \quad (2.18)$$

Eq. (2.17) shows the relation between the voltage applied to the varactors and the frequency, to make the leaky-wave antenna radiates at angle θ . It should be noted that the voltage is introduced first only for the purpose of analytic derivations, and will be uniquely defined by the required propagation constant.

2.4.2 Circuit Design and Experimental Results

By tuning the reverse-biasing voltage applied to the varactors, the capacitance of the unit-cells can be modified and this property is exploited to keep β' constant at different frequencies. In order to demonstrate this effect, a 12-cell LW antenna was constructed. The circuit parameters in Fig. 2.7 (b) can be extracted from S-parameters obtained from a full-wave simulation. The first step is to examine the series and shunt resonance frequencies of the unloaded case (without varactors) which correspond to a stopband of the dispersion diagram. Such that, an approximation of the parameters of the circuit model can be obtained which can help us to choose a frequency band of operation. We optimize reflection and transmission coefficients from the circuit model for this frequency band and compare them to the full-wave simulation results. In the optimization process we define two of the lumped elements as variables and set the other two as constants. Here we used Agilent Advanced Design System to perform this task [11]. The values for

Table 2-A: Dimensions and extracted circuit model parameters of the structure

Parameters	Value
No. of fingers	8
Finger length L_f (mm)	6
Finger width w (mm)	0.3
Inter-finger spacing g (mm)	0.3
Stub length L_s (mm)	7.6
Stub width W_f (mm)	1
Series inductance L'_R [nH]	2.14
Series capacitance C'_L [pF]	9.47
Shunt inductance L'_L [nH]	7.5
Series capacitance C'_R [nH]	1.1

the CRLH unit-cell's parameters are listed in Tab. 2-A along with the extracted circuit model parameters.

The prototype is shown in Fig. 2.8. Infineon BB833s are used for the varactors which gives a graphic relation between the capacitance and reverse biasing voltage $C_T = f(V_R)$ in its datasheet [12]. Clearly, this can be fit into Eq. (2.15), further to yield the analytical voltage-frequency relation by inserting all the circuit parameters into Eq. (2.17). Chip inductors Multicomp MCFT000163 10uH are used for the DC feed inductors which are also used to isolate the ac signal. There is one parallel varactor used in each unit-cell. The biasing distribution is uniform so only one biasing network is required. This antenna is fabricated on Rogers RO 3003 with $\epsilon_r = 3$ and $h=1.524\text{mm}$.

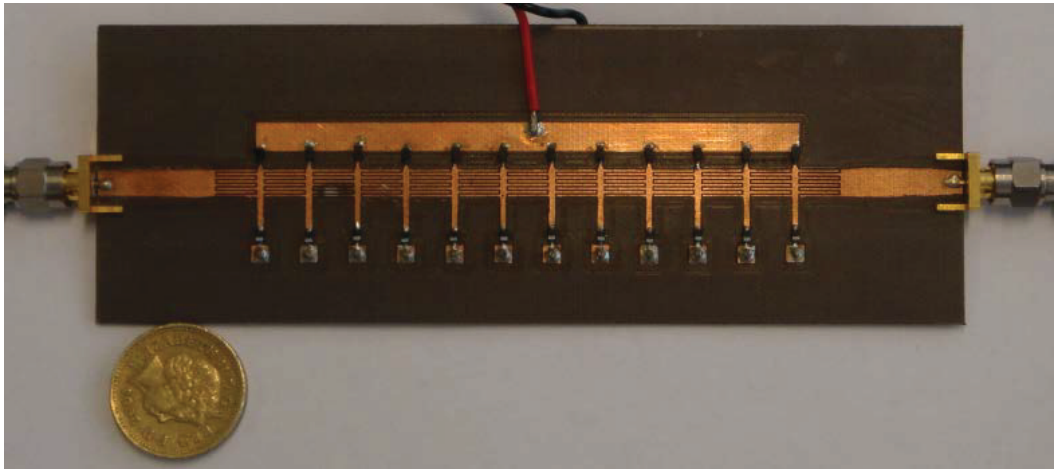


Figure 2.8: The prototype of a 12-cell voltage controlled leaky-wave antenna.

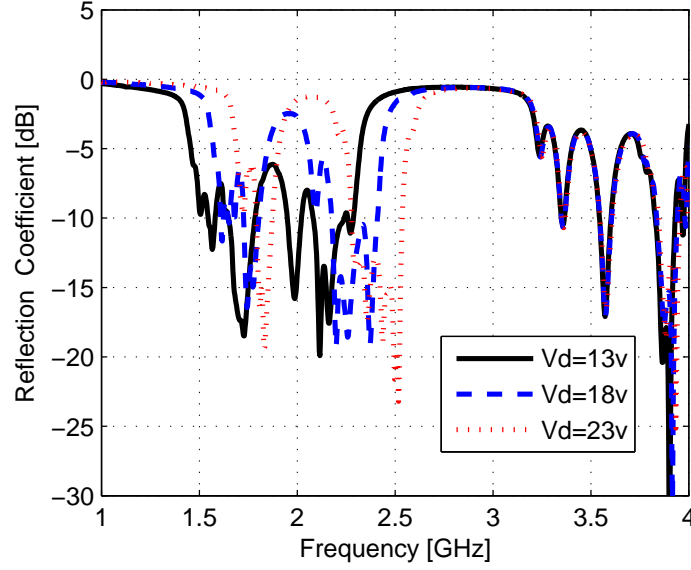


Figure 2.9: Measured return loss under different reverse-biasing voltages of 13 V, 18 V and 23V.

The antenna is designed to operate from 1 GHz to 4 GHz with a reverse-biasing voltage ranging from 0V to 27V. When the voltage increases, the working frequency band shifts to the right, as shown in Fig. 2.9.

As shown in Fig. 2.10 (a), the radiation angle of the antenna at frequencies of 1 GHz, 2.9 GHz and 4 GHz are measured to be -65° (LH), 0° (broadside) and 55° (RH). The measured gain at 2.9 GHz is 6.5dBi. As the frequency increases the radiation pattern shifts from the backward direction towards the forward direction which is a typical characteristic of an leaky-wave antenna. The measured half-power beamwidths (HPBW) are 40° , 40° and 30° at 1 GHz, 2.9 GHz and 4 GHz, respectively. The use of more unit-cells can improve the HPBW,[6] while applying non-uniform reverse-bias voltages can also shape the beam.[9] Fig. 2.10(b) shows the beam fixed at 1.8 GHz, 2.27 GHz, 2.37 GHz, and 2.52 GHz after varying the reverse-biasing voltage to 0V, 13V, 18V, and 23V respectively, while the radiation angle is fixed at about -52° and the measured HPBW remains unchanged at about 38° , respectively. The synergy of varactor action and the frequency variation keeps β constant which consequently keeps the effective length of the antenna same at all these frequencies which in turn keeps HPBW fixed.

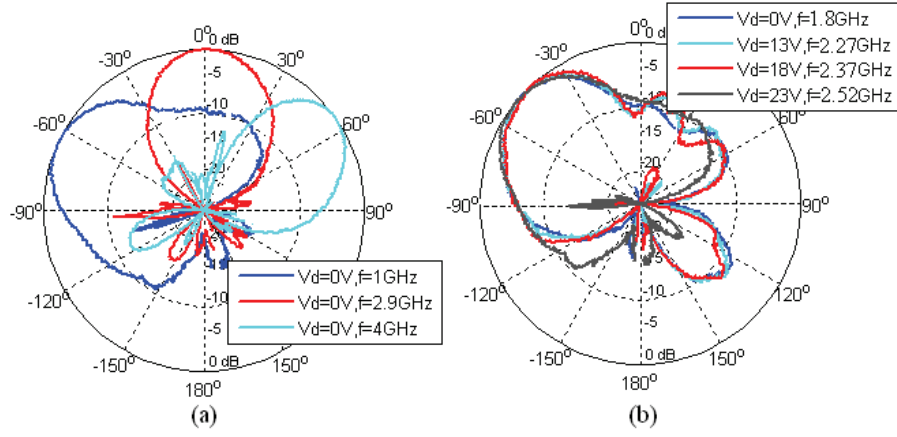


Figure 2.10: Measured E-field patterns of the 12-cell voltage controlled LW antenna. (a) Radiation patterns at 0 V, scanning from 1 GHz to 4 GHz. (b) Voltage controlled beam at different frequency points, scanning at 1.8 GHz, 2.27 GHz, 2.37 GHz and 2.52 GHz.

As shown in Fig. 2.11, the relation between the voltage applied to the varactor and the frequency obtained by Eq. (2.17) for a fixed radiation angle which is about -52° shows a good match with the one obtained experimentally. However, we shall observe that a poor agreement between the theoretical and measurement results occur when the frequency beyond 2.6 GHz, which is due to the varactor is limited to work under 2.5 GHz. By comparing the measured data with those obtained theoretically, we can draw the conclusion that it is feasible to use computed voltage values that are defined for different frequencies, in order to fix the beam.

It is important to point out the differences between our design and the one presented in [9]. While it should be quite possible to achieve the fixed-beam operation with the latter design, the proposed design in this work is greatly simplified. In our design, we only require a single varactor per cell, consequently simplifying the processing, whilst improving cost-effectiveness. The reasoning for this simplification lies in the ability to disregard the balancing condition, even as the applied voltage changes cause the band-gap edge to shift, the chosen operating point relative to this band-gap edge remains constant and consequently keeps the radiation angle same. Subsequently, as balancing is not required for such operation, this provides improved flexibility in the design, and

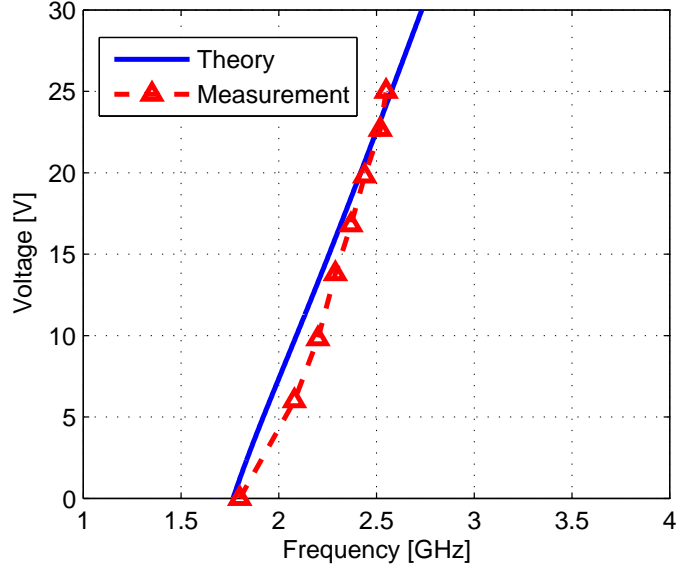


Figure 2.11: Theoretical and measurement results of the relation function between the voltage and the frequency.

subsequent simplification of the antenna. It is further noted that similar operation may also be achieved by placing the varactor along the series branch.

2.5 Conclusion

In summary, a distinct leaky-wave antenna based on the tuneable CRLH TL structure has been proposed for fixed-beam operation. The fixed-beam operation has been achieved by means of varactor diodes incorporated into the structure. A 12-cell structure has been fabricated, and is shown to radiate at a particular direction at different frequencies. The fixed radiation angle is obtained through manipulation of the reverse biasing voltage for the varactors which counters the effect of frequency variation and helps reposition the beam. We have demonstrated that for a radiation angle of -52° the antenna offers a radiation bandwidth of more than 40% while keeping beamwidth constant. Such capability might invoke applications where this type of antenna can be employed.

References

- [1] C. Caloz and T. Itoh, *Electromagnetic Metamaterials: Transmission Line theory and Microwave Applications*. NJ: Wiley-Interscience publication, 2006.
- [2] D. Sievenpiper, L. Zhang, R. Broas, N. Alexopolous, and E. Yablonovitch, “High-impedance electromagnetic surfaces with a forbidden frequency band,” *IEEE Trans. Microw. Theory Tech.*, vol. 47, pp. 2059–2074, 1999.
- [3] A. Lai, C. Caloz, and T. Itoh, “Composite right/left-handed transmission line metamaterials,” *IEEE Microwave Magazine.*, vol. 5, pp. 34–50, Sep. 2004.
- [4] Ansys. [Online]. Available: http://ansys.jp/solutions/analysis/electronics/tech_docs/meta/images/Left-Handed_Metamaterials_for_Microwave_Engineering.pdf
- [5] L. Lei, C. Caloz, and T. Itoh, “Dominant mode leaky-wave antenna with backfire-to-endfire scanning capability,” *Electron. Lett.*, vol. 38, no. 23, pp. 1414–1416, Nov. 2002.
- [6] A. Rahman, Y. Hao, Y. Lee, and C. G. Parini, “Effect of unit-cell size on the performance of composite right/left-handed transmission line based leaky-wave antenna,” *Electron. Lett.*, vol. 44, pp. 788–790, 2008.
- [7] O. Losito, M. Gallo, V. Dimiccoli, D. Barletta, and M. Bozzetti, “A tapered design of a crlh-tl leaky wave antenna,” *EUCAP 2011*, 2011.
- [8] A. Thior, X. Begaud, O. Maas, and A. C. Lepage, “Bandwidth enhancement of crlh leaky-wave antennas,” *EUCAP 2011*, 2011.
- [9] S. Lim, C. Caloz, and T. Itoh, “Metamaterial-based electronically controlled transmission-line structure as a novel leaky-wave antenna with tunable radiation angle and beamwidth,” *IEEE Trans. Microwave Theory Tech.*, vol. 53, pp. 161–173, 2005.
- [10] C. Luxey and J. M. Laheurte, “Effect of reactive loading in microstrip leaky wave antennas,” *Electron. Lett.*, vol. 36, pp. 1259–1260, 2000.
- [11] Advanced Design System 2013, Agilent Technologies, URL: <http://www.agilent.com/>.
- [12] Infineon. [Online]. Available: <http://www.infineon.com/dgdl/bb833series.pdf?folderId=db3a304313d846880113d94414f400fc&fileId=db3a304313d846880113d969a38b0112>

Chapter 3

Characterization of Active Metamaterials with Non-Foster Loads

This chapter presents a detailed assessment of characterization of active metamaterials with non-Foster loads. Typically, non-Foster elements refer to negative lumped elements (i.e., *negative capacitance*, and *negative inductance*) whose reactance-versus-frequency slope is negative, which are opposite to the ordinary positive lumped elements. Moreover, they are always realized by an active two-port device called negative impedance converter (NIC). Therefore, like any other active circuits, non-Foster loaded network suffer from the possibility of instability. Such that, in this work, the stability of active metamaterials with non-Foster loads will be analyzed, in order to achieve broadband μ -negative (MNG) or μ -near-zero (MNZ) metamaterials. Particularly, we propose a novel immittance-based stability criterion for the design of broadband active magnetic metamaterials. Furthermore, the way to achieve zero-loss and broadband magnetic properties is also provided by investigating the wave propagation in the effective medium based on the transmission line theory.

3.1 Background

In **Chapter 1**, it was shown that the realization of conventional metamaterials implies the use of the resonant structures [1–3]. Particularly, the “negative” or “near-zero” material properties (ε and μ) are possible only within a narrow frequency band near the resonance, which make the matamaterial highly dispersive and lossy. Recently, it was suggested that active metamaterials can be used as a means of overcoming these limitations [4–7].

The idea of the incorporation of active circuits into an artificial medium is not new. A fair amount of attention has been given to the active inclusions such for various potential microwave applications. They included structures with non-linear response and the broadband active absorbers [8–10].

To the best of the author’s knowledge, the original idea of using non-Foster elements in the design of broadband metamaterials was theoretically proposed by Tretyakov [4]. In his paper, it was shown analytically that a loading of a short dipole with a negative capacitance would leads to the wideband dispersionless ENG (ε -negative) behavior and the loading of a small loop with a negative inductance corresponds to the wideband dispersionless MNG behavior. Although the subsequent theoretical study [11] from the same author illustrated the inherent instability of of dispersionless ENG and MNG metamaterials based on non-Foster elements, there had been a few theoretical studies about the realization of broadband MNG metamaterials with non-Foster loads [6, 12], where both the stability and bandwidth enhancement were successfully achieved.

Another main challenge of the metamaterials is the high loss which limits its application in the microwave engineering. However, it was shown possible to obtain a metamaterial with low-loss by using power amplifiers to compensate for the losses [13, 14].

The brief review of the history of active metamaterials shows the potential advantage of the approach based on non-Foster elements and power amplifiers. However, it

should be noted that the stability investigation on the active metamaterials with practical non-Foster circuits has not been given enough attention yet. Hence, in the subsequent sections, several techniques are explored for analyzing the stability of the actively-loaded medium. A novel approach will be proposed that allows the design of stable broadband non-Foster-elements-based MNG or MNZ metamaterials. Furthermore, a broadband zero-loss magneto-inductive transmission structure will be analytically proposed, so as to achieve both low-loss and broadband properties.

3.2 Effective Medium of Loop Arrays

3.2.1 The Unit Cell

In [6], it was suggested that periodic loops with non-Foster loads could be used to create an stable low-dispersion MNG or MNZ metamaterials, although in practice the nature of the load would be limited by stability.

At a radial frequency ω , the impedance of a loop m with an arbitrary load Z_L is,[15]

$$Z_m = \left[\frac{1}{R_m + j\omega L_m} + \frac{j\omega C_m}{1 + j\omega C_m R_C} \right]^{-1} + Z_L, \quad (3.1)$$

where L_m is the self-inductance of the loop, R_m is the sum of the radiation resistance R_r and the Ohmic resistance R_w , and C_m is the loop capacitance which, despite contributing little to the effective materials properties, cannot be ignored for stability analysis of the actively loaded medium. For the case of an array of identical loops, we henceforth define L_m , R_m and C_m as L_0 , R_0 and C_0 respectively.

Mutual coupling will also have an important effect on stability, as well as the effective material properties. An equivalent circuit of N loaded loops is shown in Fig. 3.1. Interactions between any two loops (m, n) in the system are represented by a mutual impedance $Z_{mn} = j\omega M_{m,n}$ where $M_{m,n}$ represents the mutual inductance. When there is

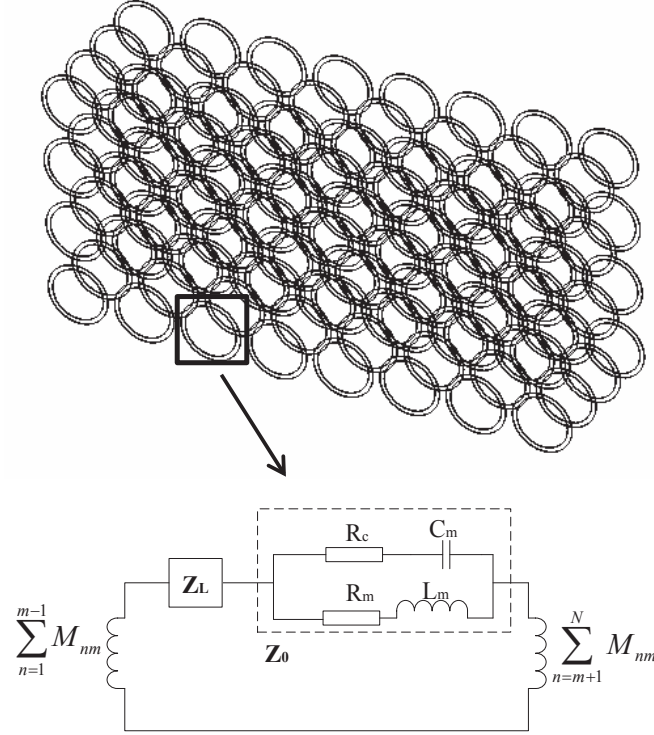


Figure 3.1: Equivalent circuit of a loop and load in a system of N coupled loaded loops[6]. Summations indicate the coupling factors between the loop m and the remaining $N - 1$ loops.

retardation of the waves due to radiation, the components of the mutual coupling matrix will be complex. For an infinite array, there will be no radiation and the mutual coupling coefficients will be real.[16, 17] For a finite array that is much shorter than a wavelength, the effects of retardation will be insignificant and so the mutual coupling coefficients can be assumed to be real. However, if an array is large and finite, retardation of the guided waves must be accounted for.[18, 19]

In [11] the stability of a small resonant antenna in close proximity to a non-Foster metamaterial shell was investigated by examining the solutions to the characteristic equation of the system. In [6] that technique was generalized to a many-bodied system, and applied to the case of a system of loaded loops. The characteristic polynomial of

the system when all loops are identical becomes,

$$|\bar{Z} - \lambda \bar{I}| = |(Z_0 + Z_L - \lambda)\bar{I} + s\bar{M}| = 0, \quad (3.2)$$

where Z_0 represents the impedance of a single isolated loop, λ is an eigenvalue of the impedance matrix, \bar{I} is an identity matrix, \bar{M} is the mutual coupling matrix, and we have defined $s = j\omega$. The problem is henceforth simplified by solving first for the N eigenvalues λ_M of the mutual coupling matrix \bar{M} and then, solving for

$$\lambda(s) = Z_0(s) + Z_L(s) + s\lambda_M. \quad (3.3)$$

For a periodic array of loops, we assume that the unit cell containing a loop and load will have a constant phase variation across it in the directions of periodicity. Taking the mutual coupling into consideration, the characteristic equation is given in [6, 20] as:

$$Z_s + 2j\omega \sum_{i \in R^N} \sum_{m=1}^{+\infty} M_{m,i} \cosh(m\gamma_i d_i) = Z_0 + Z_L + j\omega M_P = 0 \quad (3.4)$$

where $Z_s = Z_0(s) + Z_L(s)$ is the series impedance, the subscript i refers to the x , y or z directions in the Euclidean space R^N , d_i is the lattice spacing, $M_{m,i}$ is the mutual coupling between two loops a distance md_i from each other in the i direction, and $\gamma_i = \alpha_i + j\beta_i$ is the propagation constant in the i direction. Particularly, the total mutual inductance term M_P has been defined for the purpose of clarity.

3.2.2 Effective Permeability

For a periodic medium of magnetically polarizable inclusions with arbitrary loading, the effective relative magnetic permeability is given in [6] and verified by FDTD simulations[21]

$$\mu_r = 1 - \mu_b N \frac{j\omega S^2}{Z_0 + Z_L + j\omega M_p}, \quad (3.5)$$

where μ_b is the background permeability, S is the loop area, N is the volume density of loops. It was suggested in [4] that, with an appropriate selection of load the relative permeability could be controlled leading to, for example a broadband negative- μ material. Subsequent analysis showed that stability would limit the performance of such a material [6, 11]. Nevertheless, accounting for mutual coupling effects and designing the material to ensure stability, it is evident that with careful selection of the load impedance a wideband MNG or MNZ material can be designed, with performance exceeding that of a passive metamaterial [6].

3.3 Review of Prior Stability Analysis of Actively-Loaded Medium

A system is stable if and only if all roots to the N equations given by Eq. (3.3) are in the left-half of the complex plane (LHP), such that the wave amplitude is not exponentially increasing. The roots can be solved for directly, and each inspected manually to ensure that the system remains stable. The Routh-Hurwitz [22], [23] technique has been applied extensively in, for example control theory and active filter design to test stability. The Routh array of a polynomial is constructed, and providing that all coefficients in the first column have the same sign, then the roots of the polynomial all lie in the LHP. This technique has been applied to ensure the stability of a diode-modulated split-ring resonator [24], and to examine the stability of a small resonant antenna in close proximity to a non-Foster metamaterial shell [11].

3.3.1 Routh-Hurwitz Stability Criterion

In [6], the Routh-Hurwitz criterion was applied to the NIC-loaded loop geometry that is also under investigation in this section, where it was used to show that, although a negative inductor in series with the loop will in all cases be unstable, a parallel negative

RLC load can be designed to be stable. Finally, finite-difference time-domain (FDTD) simulations were used to confirm the results of the analytical theory.

Periodic boundary conditions were used to simulate the effective media, with a unit cell consisting of a loop with a non-Foster load connected in series. The load was modeled across a single mesh cell. It was shown that, for a parallel, negative RLC load, the stability bounds of the load inductor is given by [6],

$$0 > L_L > -\frac{R_L}{R_0 + R_L} \frac{[L_0 + \lambda_M]^2}{[L_0 + \lambda_M + R_0 R_L C_L]}, \quad (3.6)$$

where λ_M represents the eigenvalues of the mutual coupling matrix, as given in Eq. (3.3). For a system of N loops, Eq. (3.6) must hold for all N eigenvalues. Since the diagonal elements (and therefore the trace) of \bar{M} are 0, then the sum of eigenvalues is 0. For non-zero eigenvalues, this implies that there must be at least one negative eigenvalue. It is sufficient to check the smallest (most negative) of the eigenvalues for stability.

For the periodic case, λ_M is replaced by M_P from Eq. (3.4), so that the stability bound becomes,

$$0 > L_L > -\frac{R_L}{R_0 + R_L} \frac{[L_0 + M_P]^2}{[L_0 + M_P + R_0 R_L C_L]} \approx -(L_0 + M_P). \quad (3.7)$$

Here, a approximation is made, since $R_0 = R_w \ll |R_L|$ for an electrically small loop which makes the item $R_0 R_L C_L$ can be almost neglected, where R_w is the loop's Ohmic resistance. This is equivalent to a single eigenvalue system in which the eigenvalue is positive. As discussed in [6], this gives the surprising result that an infinitely periodic system will have a greater range of stability than a similar, but finite system. The general conclusion from these stability bounds is that the negative load inductance must not overcompensate for the self and mutual inductances. The range of stability bound for the load capacitance can similarly be found as [6],

$$C_L < -\frac{L_0}{\omega_0(L_0 + M_P)} \sqrt{\frac{M_P(L_0 + M_P)}{R_C |R_L| (L_0 + M_P)^2 + R_0 M_P^2}}, \quad (3.8)$$

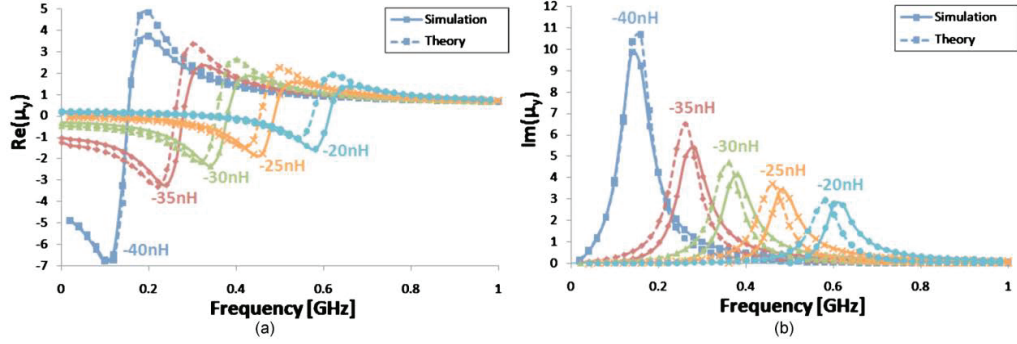


Figure 3.2: Simulated and theoretically calculated real (a) and imaginary (b) permeabilities for a range of negative load inductances [6].

where $\omega_0 = 1/\sqrt{L_0 C_0}$ is the resonant frequency of the unloaded loop. In general this expression is important as it demonstrates the need for a nonzero load capacitance (and therefore one may not use a purely inductive load). The load capacitance will also limit the bandwidth of the effective medium by introducing a resonance that will decrease in frequency as the magnitude of C_L (and thus stability margin) increases.

Assuming an infinite periodic loop array with loop size 10 mm, wire radius 1mm and coaxial loop spacing 10 mm, a stable broadband metamaterial can be designed. Loading each loop with resistance $R_L = -1000\Omega$, then the range of stable values for the load inductance can be obtained as $0 > L_L > -43.9nH$, as calculated by Eq. (3.7). Furthermore, the upper bound of the stable load capacitance is given by $C_L < -1.54pF$ according to Eq. (3.8). It is simple to see that L_L must be reduced toward the stability bound in order to achieve a more negative real part of the permeability. In Fig. 3.2, the effective parameters of the non-Foster loading medium obtained from Eq. (3.5) are plotted compared to the numerical simulations.[21] The non-Foster load is defined as a parallel negative RLC circuit with $R_L = -1000\Omega$, $C_L = -2pF$, and L_L varying discretely from -40 nH to -20 nH for all elements. It is clearly shown that, as the load inductance is decreased, the relative permeability will decrease. Bandwidth is limited by the resonance formed by the negative inductance and capacitance in parallel, and so a more negative permeability will have a smaller bandwidth.

3.3.2 Nyquist Stability Criterion

Although the stability bounds presented above may be used in the design of the actively-loaded material, difficulties arise when the load impedance becomes more complex, or when a fabricated NIC deviates from the ideal lumped element model. In these cases, the analytical stability bounds in [4, 25, 26] will no longer hold. If the lumped element model is modified with, for example the addition of further inductors, capacitors and/or resistors, the Routh-Hurwitz method must be reapplied to this modified model. And with a higher-ordered characteristic polynomial, analytical solutions will become increasingly cumbersome. Similarly, as an NIC circuit will inevitably exhibit some variation from the ideal model, application of the Routh-Hurwitz criterion or even root-finding would require potentially complicated fitting to higher-ordered equivalent circuits. As such, a frequency domain technique would be preferable, for which the measured or simulated impedance of an NIC can be tested for stability in combination with the effective medium. We will present the use of the Nyquist criterion for this purpose. The Nyquist criterion will allow stability testing in the frequency domain, while also providing stability margins and a design procedure that will allow one to engineer the composite material so as to ensure stability over a range of structural geometries and periodicities. Analysis of the Nyquist contour has been used extensively to determine small signal stability in power electronics for the design of power distribution systems.[27] The Nyquist contour of the product of the source impedance (\mathbf{Z}_s) and the load admittance (\mathbf{Y}_l) are analyzed to verify the stability at a given operating point. Cauchy's argument principle is the mathematical basis for the Nyquist criterion.[28] The product $\mathbf{Z}_s(s)\mathbf{Y}_l(s)$ maps a closed contour C into the complex plane. For the analog systems we shall examine, the contour is composed of the imaginary $j\omega$ -axis and an arc of infinite radius that completely encloses the (unstable) right-half of the complex s -plane (RHP). As $\mathbf{Z}_s(s)\mathbf{Y}_l(s)$ is analytic within and on C , except at a finite number of poles, and with neither poles nor zeros on C , then

from Cauchy's argument principle we have the result that,

$$N = Z - P, \quad (3.9)$$

where Z and P are, respectively, the number of zeros and poles of $\mathbf{Z}_s(s)\mathbf{Y}_l(s)$ in C , while N is the winding number of C , or the number of encirclements of the origin, taken in the same sense as C .

It is straightforward to show that if neither \mathbf{Z}_s nor \mathbf{Y}_l have any poles in the RHP, then the number of unstable poles of the closed loop system is equal to the number of clockwise encirclements of -1 made by the Nyquist contour of $\mathbf{Z}_s(s)\mathbf{Y}_l(s)$ [27]. We note that the determination of whether the NIC is the source or the load is not dependent on whether it is supplying or consuming power, but rather on the location of its poles and zeros. An open-circuit stable (OCS) NIC will have all impedance poles in the LHP [29] and would be defined as the source. Likewise, the admittance poles of a short-circuit stable (SCS) NIC will lie in the LHP [29] and so it is defined as a load.

Similarly, we may apply this technique in comparison to the results of the Routh-Hurwitz method. For each element, we apply the same definition of the physical size which has been proposed before. The active load consists of parallel negative resistors, inductors and capacitors. The negative resistors are $R_L = -1000\Omega$ and the negative capacitors are $C_L = -5pF$. Using the Routh-Hurwitz method, a stable range of inductances is found using Eq. (3.7) to be $0 > L_L > -41.3nH$. This is verified graphically using the Nyquist criterion in Fig. 3.3. The Nyquist contours are plotted for a range of values, from $L_L = -50nH$ to $L_L = -30nH$. Recalling that a stable contour will not encircle the -1 point, it is evident that this method agrees with the results of the Routh-Hurwitz calculation; for $L_L = -41nH$ the contour does not circle the -1 point, while for $L_L = -42nH$ it does, signifying instability.

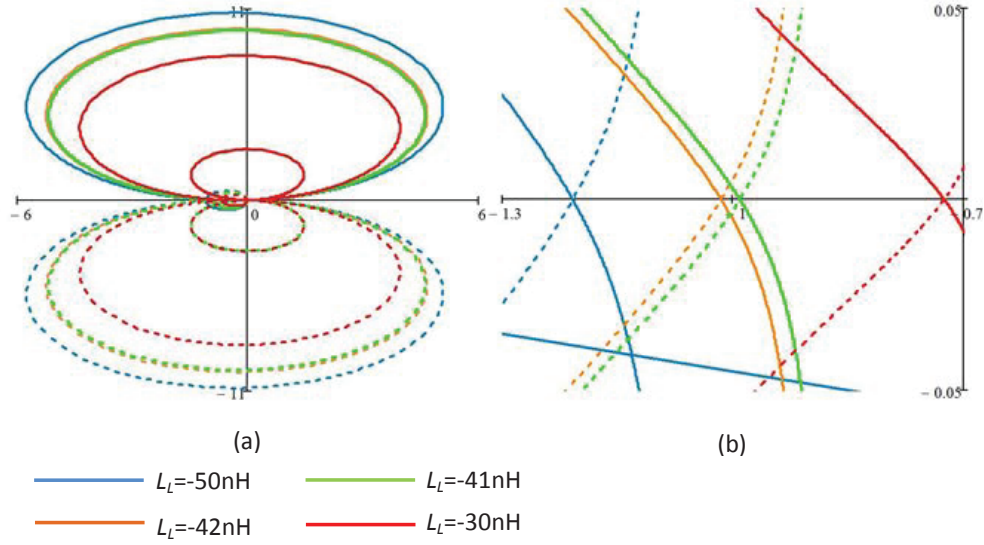


Figure 3.3: Nyquist contours of a periodic system of loops. The dotted lines are their reflections, which represent the plots in negative-frequency ($-\omega$) space. The negative inductance is varied from the unstable to the stable cases. The Routh-Hurwitz method gives a stable range of inductances at $L_L > -41.3\text{nH}$; the Nyquist method clearly agrees with that. (a) The Nyquist contours for $L_L = (-50, -42, -41, -30)\text{nH}$. (b) Magnification of the Nyquist contours around the -1 point. It is evident that for $L_L = (-50, -42)\text{nH}$ the systems are unstable, while for $L_L = (-41, -30)\text{nH}$ the systems are stable.[12]

3.4 Immitance-Based Stability Characterization of Actively-Loaded Medium

In the previous section it was shown the Nyquist stability criterion can be used as a means of checking the stability of practical NIC-loaded medium. However, deep investigation reveals that this approach suffer from some limitations. One drawback associating with this analysis method is that it is not design oriented. By inspection of encirclements of -1 made by the Nyquist contour, the stability of a single operating point can be assessed. For a static circuit network, every component has a certain impedance or admittance value at each frequency point, then the source impedance and load admittance are referred to as a single operating point. However, for most dynamic systems, the source impedance or load admittance may vary with the time, therefore the application of the Nyquist criterion is

restrained. Another disadvantage of this method is that the Nyquist evaluation needs enough frequency points to construct a enclosed contour.

Due to these drawbacks, an impedance/admittance based approach is proposed here which can overcome these limitations and applied to the design of active broadband metamaterials. In essence, this is a method of transforming the forbidden region into a load admittance (source impedance) specification for a given source impedance (load admittance). Similar as [27], there are two aspects to this method, which can be employed separately or together. First, a new stability criterion named as Exponential Peak Stability Criteria (EPSC) is developed to ensure robust stability, which is less artificially conservative than the heretofore available methods. However, like many other Nyquist based stability criteria, one of the shortcomings of this method is that it is not conducive to an easy design formulation. Hence, an admittance space based design process is demonstrated as the second contribution, which allows design specifications to be readily derived for an arbitrary stability criterion. In addition, it can be used to explicitly address operating points and parameter variations. Finally, a sample NIC-loaded material is implemented and simulated to provide an accurate portrayal of the stability of these active metamaterials, as well as broadband material properties.

3.4.1 Principle of Imittance-Based Stability Analysis

It is appropriate to begin this section with a brief review of the generalized imittance-based stability analysis of dc power systems. This technique was set forth in a series of publications [30–35]. Although it is readily extendible to complex multi-bus system,[33] here we begin our analysis in terms of a simple source-load system. As shown in Fig. 3.4, there is a source with input impedance $Z_s(\theta_s, s)$ and a load with admittance $Y_l(\theta_l, s)$, where θ_s and θ_l are vectors of variables which define a steady-state operating point of the source and load respectively and where s is complex frequency. Formally, the source impedance and load admittance are linearized transfer functions relating a change in

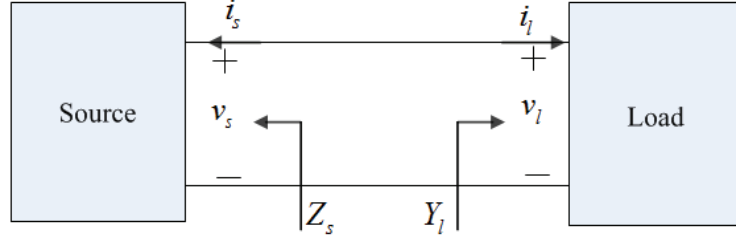


Figure 3.4: Source-load system.

voltage to a change in current at the terminals [34],

$$\begin{aligned} Z_s(\theta_s, s) &= \left. \frac{\Delta v_s}{\Delta i_s} \right|_{X_s=\theta_s} \\ Y_l(\theta_l, s) &= \left. \frac{\Delta i_l}{\Delta v_l} \right|_{X_l=\theta_l} \end{aligned} \quad (3.10)$$

where X_s and X_L denote the state vectors of the source and load.

It is known that given a source is stable at an operating point θ_s when supplying a constant current load (which is compatible with θ_l) and that the load is stable at an operating point θ_l when fed from a constant voltage source (which is compatible with θ_s) then the source-load system will be stable at operating point $\theta = [\theta_s^T \ \theta_l^T]^T$ provided that the Nyquist contour of $Z_s(\theta_s, s)Y_l(\theta_l, s)$ does not encircle the -1 point in the s -plane.

While the Nyquist evaluation of $Z_s(\theta_s, s)Y_l(\theta_l, s)$ and inspection for encirclements of -1 can be used as a stability test which has been discussed in previous section, another important application is that it can be extended to a number of stability criteria which can be used to formulate design specifications. As an example, given a source impedance or a load admittance and a stability criterion, a constraint on a load admittance or source impedance can be determined and used as a design specification. The concept behind immittance-based stability analysis is to, in a single analysis, show that all operating points of interests are stable. To formulate this answer, the generalized source impedance

and load admittance are defined as [34]

$$\begin{aligned}\mathbf{Z}_s(s) &= \{Z_s(\theta_s, s)|_{\theta_s \in \Omega_s}\}, \\ \mathbf{Y}_l(s) &= \{Y_l(\theta_l, s)|_{\theta_l \in \Omega_l}\},\end{aligned}\tag{3.11}$$

where Ω_s and Ω_l denote the set of all possible operating points. In essence, a generalized immittance is a closed set of complex numbers, rather than being a complex number at a given frequency. This set arises from the fact that the dynamic model of most power electronics based components is non-linear and so the linearized model is a function of operating point. Furthermore, generalized immittances can be used to represent the effects of parameter uncertainties.

If the Nyquist evaluation of the product of $Z_s(s)Y_l(s)$ does not encircle -1, then all operating points of the source load system are stable. Hence, in each case, the function of the stability criterion is to prevent the Nyquist evaluation of a source-impedance load-admittance product from circling the -1 point. Thus systems that meet these criteria have models which have stable equilibrium points. Fig. 3.5 illustrates a number of these criteria in the s -plane, such as the Middlebrook Criterion[35], the Gain and Phase Margin (*GM**PM*) Criterion[36], the Opposing Argument Criterion[31, 32], and the Energy Source Analysis Consortium (ESAC) Criterion[27, 30]. All these criteria define various forbidden regions. According to Fig. 3.5, the least restrictive criterion is the ESAC criterion.

In this work, a novel stability criterion is proposed, the Exponential Peak Stability Criterion (EPSC) which is a development of the maximum peak criterion (MPC) [37, 38]. By applying a circle-like forbidden region in terms of PM and GM, the MPC has been widely used in control engineering to design loop gains for ensuring robust stability. Although the forbidden region of the MPC occupies much less space in the complex plane than the previous criteria depicted in Fig. 3.5, it also has shortcomings. In order to guarantee the stability, it is shown that the Nyquist contour of $Z_s(s)Y_l(s)$ shall stay out

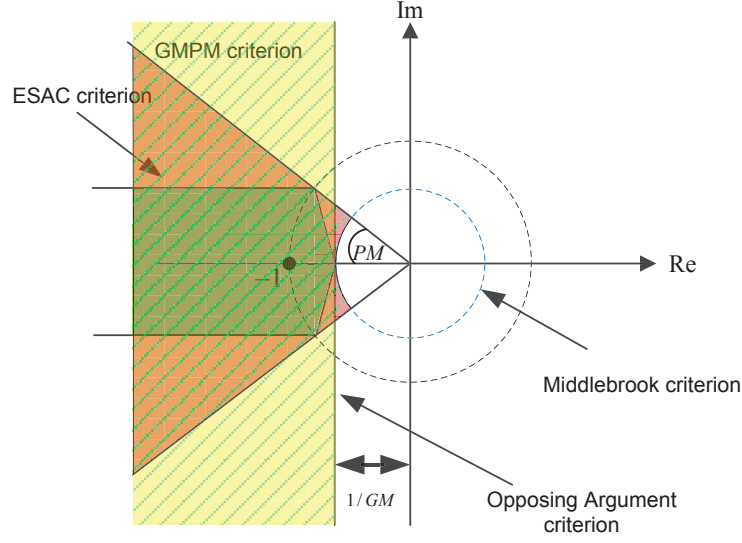


Figure 3.5: Various stability criteria and their forbidden regions in the complex plane [27].

of the defined MPC-based forbidden region and also satisfy the Nyquist stability criterion which therefore make this method become overly cumbersome. However, the EPSC can overcome the limitations of the MPC criterion in that it gives a sufficient condition for robust stability to exist by keeping the Nyquist contour outside the forbidden regions only.

As shown in Fig. 3.6, the boundary between allowable and forbidden regions of the EPSC in the complex plane is formed by a half circle and two exponential function curves which start at infinity, and terminate at the boundary of the half circle. The methodology of shaping the forbidden region of the EPSC is based on the principle of preventing the Nyquist contour from encircling the -1 point, thus ensuring robust stability. Meanwhile, we want to define the stability criterion that allows the Nyquist diagram to occupy a smaller region and hence reduces artificial conservativeness. A natural derivation here is using two exponential function curves to form the boundary, which toward to the real axis as $s \rightarrow -\infty$. The circle is defined by the MPC specifying the gain and phase margins. Moreover, the EPSC-based forbidden region (green area)

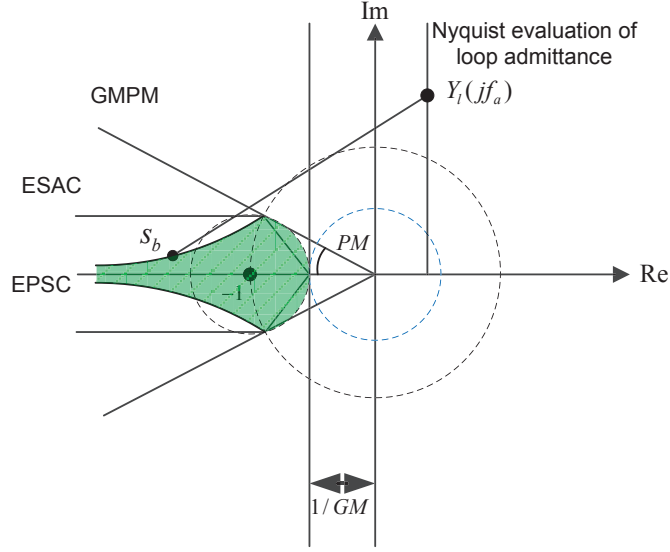


Figure 3.6: EPSC-based forbidden region versus ESAC and GMPM regions.

is compared to the ESAC and GMPM regions defined in [27, 36], and hence leads to a less artificially conservative immittance-based stability criterion.

Mathematically, the EPSC boundary can be defined by introducing a piecewise implicit function

$$\begin{cases} (1 + \operatorname{Re}(s))^2 + \operatorname{Im}(s)^2 = \frac{1}{M_S^2} & \text{if } -\cos(PM) < \operatorname{Re}(s) \leq -1/GM, \\ |\operatorname{Im}(s)| = \sin(PM)e^{k[\cos(PM) + \operatorname{Re}(s)]} & \text{if } \operatorname{Re}(s) \leq -\cos(PM). \end{cases} \quad (3.12)$$

where $\operatorname{Re}(s)$ and $\operatorname{Im}(s)$ denote the real and imaginary parts of a complex variable s , and

$$M_S = |S_{max}| = \frac{1}{2 \sin(PM/2)} = \frac{1}{1 - 1/GM}$$

is the amount of peaking specified by the MPC with the desired phase margin PM and gain margin GM [38], k is the index coefficient of the exponential branches which can be used to control the size of the forbidden area. It is noted that in order to for the EPSC to be less conservative than the ESAC criterion, it is necessary that k is positive real constants. Furthermore, it is shown that the path of the EPSC in the s -plane

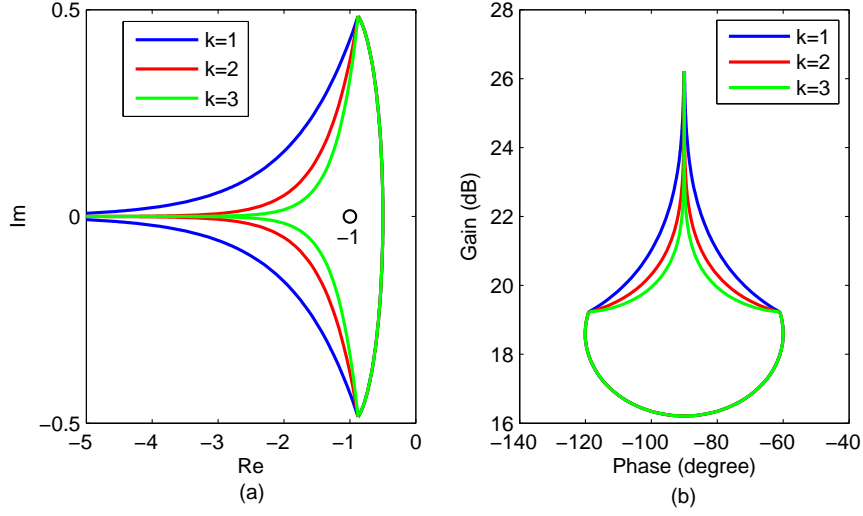


Figure 3.7: (a) The EPSC boundary in the complex plane where $M_S = 2$, and k is varied from 1 to 3. (b) The corresponding impedance constraint of the active load at a given frequency of 300MHz

will not close, as $\text{Re}(s) \rightarrow -\infty$, $\text{Im}(s) \neq 0$. Fig. 3.7 (a) depicts the EPSC boundary with different values of k where the peaking M_S is set at 2 for each case by specifying $PM \approx 29^\circ$ and $GM = 6\text{dB}$. Hence, it is straightforward to see that the forbidden region gets smaller as the index coefficient k increases.

Now we shall apply the EPSC to give the design specifications for an actively-loaded loop array. By inspection of the locations of their poles and zeros, one can notice that the active load for each loop should be defined as the source of the EPSC system whilst an unloaded loop gives the corresponding system load, which is similar as the Nyquist stability analysis. As shown in Fig. 3.6, the source impedance $Z_s(s)$ of an actively-loaded loop based on the load admittance $Y_l(s)$ for a given frequency f_a can be derived using the methods set forth in [27, 30, 34], which will cause the Nyquist contour of $Z_s(s)Y_l(s)$ to touch the stability criterion curve specified by Eq. (3.12) at point s_b

$$Z_s(jf_a) = \frac{s_b}{Y_l(jf_a)}, \quad (3.13)$$

where $Y_l = 1/(Z_0 + j\omega M_p)$ is the equivalent system load admittance accounting the

mutual couplings. By sweeping the point s_b over the entire boundary, the source impedance constraint at frequency f_a is consequently obtained as depicted in Fig. 3.7 (b), resulting in the forbidden region of the active load at the frequency of $300MHz$. Therein, the same physical definitions for the loop array are taken as proposed before. Moreover, the same values of the peaking and index coefficients are set for comparison, where $M_S = 2$ and $k = (1, 2, 3)$. Clearly, it is shown that an increasing k leads to a less conservative design because it gives more allowable source impedances. Another important factor when define the EPSC boundary is the peaking M_S , which however has the opposite effect as compared to the index coefficient.

By repeating this construction for all frequencies of interest, the EPSC forbidden volume in three dimensional impedance space can be depicted which is similar as the ESAC criterion [27]. In this method, a stability constraint is developed in terms of three-dimensional imittance space in which the three axis refer to frequency (x), phase (y) and magnitude (z). As shown in Fig. 3.8, the stability constraint of the NIC load for an actively-loaded loop array in the impedance space is depicted. Here, the gain margin, phase margin, and the index coefficient are set at 0.467 dB , 3° , and 2, respectively. To ensure robust stability, the load impedance must lay outside the forbidden volume. However, as a conservative design rule, it should be noted that the EPSC gives only sufficient, but not necessary stability conditions which is also the main drawback of any imittance-based stability criteria. To overcome this difficulty, an optimized EPSC boundary should be specified so as to encompass more allowable generalized impedance and admittance sets (denoted $\mathbf{Z}_s(s)$ and $\mathbf{Y}_l(s)$, respectively). This can be done by manipulating the parameter values of the EPSC including both the peaking and index coefficient.

To verify this stability analysis technique, we shall compare the results to the other analysis as proposed in last section. Again, assuming that each loop is loaded with a parallel negative RLC circuit, specifying resistance $R_L = -1000\Omega$ and $C_L = -5pF$ in advanced, then the range of stable values for the load inductance can be derived as $0 > L_L > -41.3nH$ by Eq. (3.7). Fig. 3.8 also shows two load impedance curves where

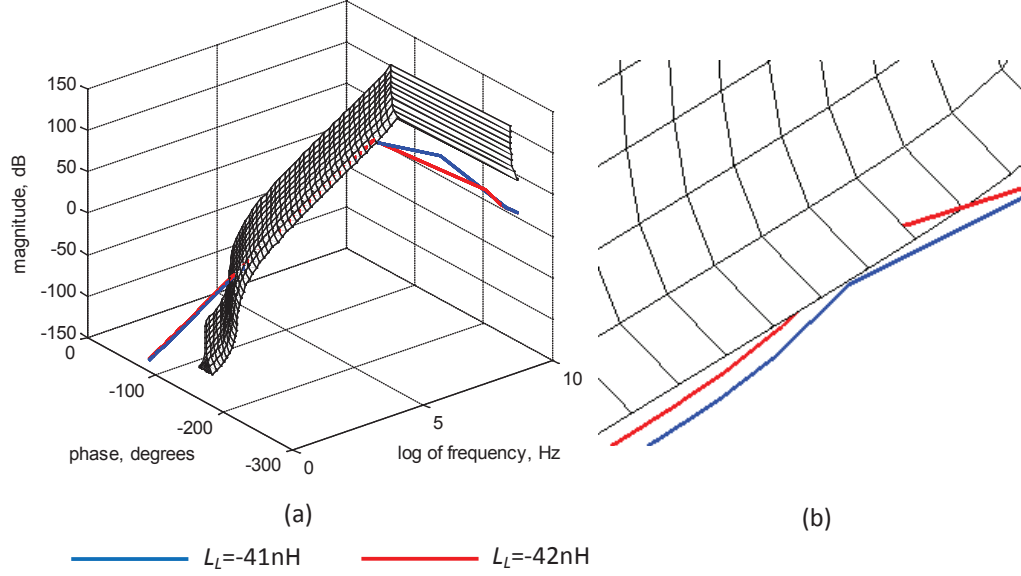


Figure 3.8: (a) Stability constraint of the active load in the impedance space. In this space, the x-axis is frequency s , the y-axis is phase PM in degree, and z-axis is magnitude GM in dB. Thus, any arbitrary impedance can be expressed by $GM(s)\angle PM(s)$. The load is defined as a parallel negative RLC circuits with $R_L = -1000\Omega$, $C_L = -5\text{pF}$ and $L_L = (-41\text{nH}, -42\text{nH})$. (b) Magnification of the stability constraint around the intersection region. It shows that the red curve penetrates the forbidden region (unstable case) whereas there is no intersection for the blue curve and the forbidden region (stable case), which is in agreement with Routh-Hurwitz criterion.

the load inductances are chosen to be $L_L = -41\text{nH}$ (blue curve) and $L_L = -42\text{nH}$ (red curve). The magnification shows that the red curves penetrates the forbidden region (unstable case) whereas there is no intersection of the blue curve and the region (stable case). Hence, it is clear that this method agrees with the Routh-Hurwitz and Nyquist stability criteria.

3.4.2 Application in the Design of Broadband Active Metamaterials

It is now straightforward to extend this stability analysis technique to the practical design of broadband active metamaterials. A concern with the previous example as shown in Fig. 3.8 is the fact that it is based on the ideal non-Foster loads. In general, the negative

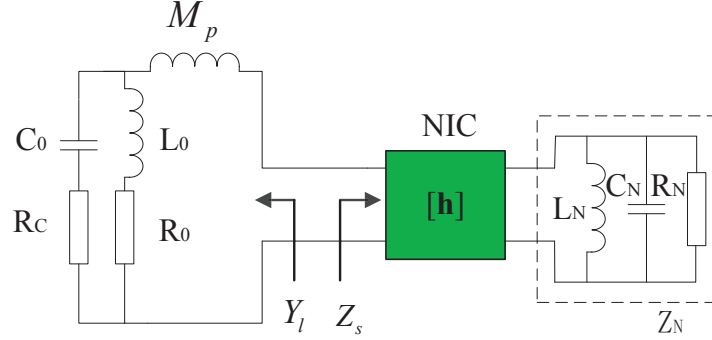


Figure 3.9: Equivalent circuit of a coupled loop with non-Foster loads. The non-Foster elements are obtained as the output of a NIC circuit terminated in a parallel positive RLC load Z_N .

non-Foster elements are realized by terminating a two-port called a negative impedance converter (NIC) in the corresponding positive elements. It is, by analogy, a form of an ideal transformer with an impedance transformation ratio of -1 . Fig. 3.9 shows the equivalent circuit of a coupled loop loaded with non-Foster elements which are realized by terminating a NIC with an ordinary positive load Z_N . In agreement with the previous analysis, the system source impedance and load admittance can be thereby obtained

$$\begin{aligned} Z_s(s) &= h_{11}(s) - \frac{h_{12}(s)h_{21}(s)Z_N(s)}{1 + h_{22}(s)Z_N(s)} \\ Y_l(s) &= \frac{1}{Z_0(s) + j\omega M_p(s)}, \end{aligned} \quad (3.14)$$

where $h_{ij}(s)$ ($i, j = 1, 2$) is the corresponding element of the h-parameters which are used to represent the NIC network, and M_P denotes the total mutual inductance term. For Z_L to be the ideal negative of Z_N , it is required that $h_{11} = h_{22} = 0$ and $h_{12} = h_{21} = \pm 1$. However, the practical NIC always accompanies the parasitics and nonlinearity thus leading to non-ideal circuit models.

Clearly, the NIC performance is crucial for an successful design of active metamaterials with non-Foster loads, hence a separate chapter detailed on the NIC design will be given later. In this section, however, we just employ the NIC output as the source impedance which is obtained from the electromagnetic (EM) simulations by Agilent ADS

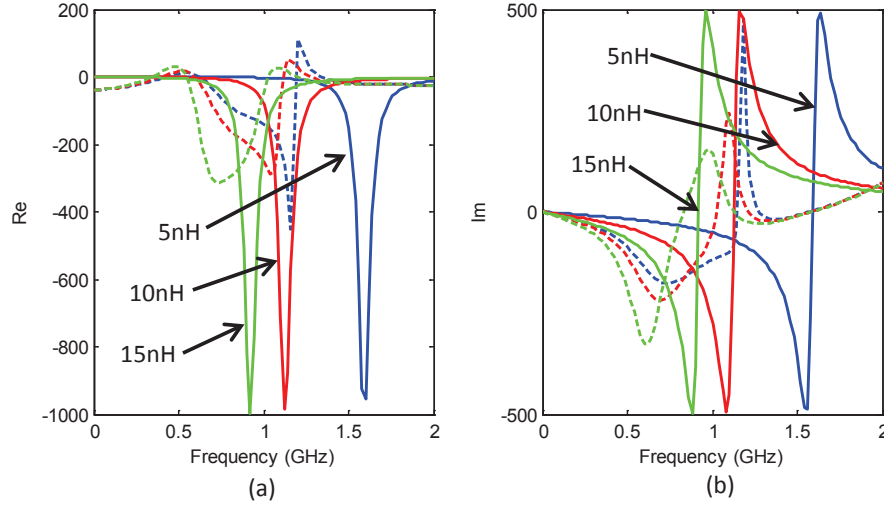


Figure 3.10: Impedance of the NIC circuits simulated using Agilent ADS, as compared to the ideal models. In all cases, the ideal NIC output is a parallel-RLC circuit with $R_L = -1000\Omega$ and $C_L = -2pF$. The negative inductance is $L_L = (-5, -10, -15)nH$. The simulation results are obtained as the output of the practical NIC network terminated a parallel RLC load with $R_N = 1000\Omega$ and $C_N = 2pF$ and $L_N = (5, 10, 15)nH$, and are represented by solid lines, while the ideal cases are represented by dashed lines. (a) Resistance. (b) Reactance.

[39] to illustrate how the EPSC can be applied in the design of active metamaterials. The simulation results of the NIC circuits are depicted in Fig. 3.10 which clearly shows the error between the ideal and practical cases. Here, a floating NIC is simulated with ADS momentum tools [39]. Although it can be noted that the simulated NIC output can be modeled as an ideal parallel negative RLC circuit consisting of different lumped elements to some extent, by comparing the shapes of the ideal and simulated results with the same NIC input.

As shown in Fig. 3.11, a full-wave simulation by HFSS [40] is performed to obtain the impedance parameters of the loop $Z_s(s)$, as compared to the analytical results calculated by Eq. (3.1). Henceforth, the system load admittance $Y_l(s)$ can be accurately given according to Eq. (3.14). Note that with periodic boundary conditions used to affect a bulk medium, this provides a more accurate model as compared to the circuit equivalent in Fig. 3.1 and allows more accurate simulation of the effective medium properties as

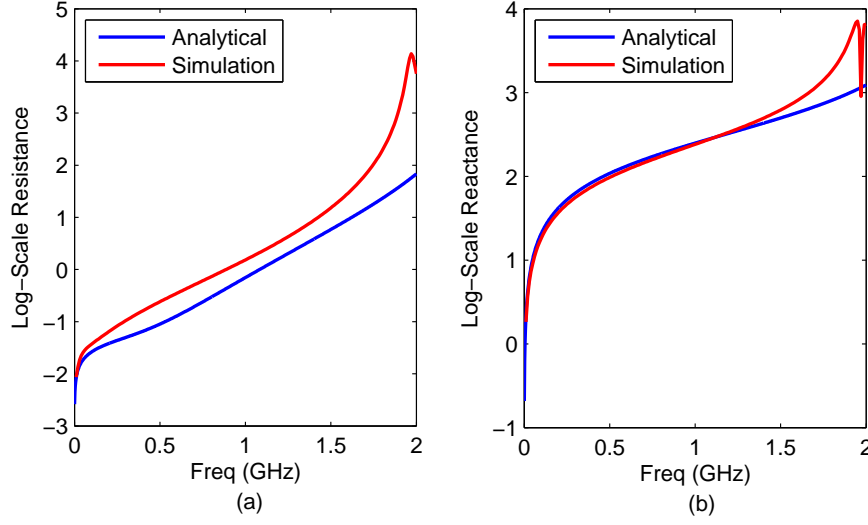


Figure 3.11: Impedance of the unloaded loop simulated by HFSS (red line), as compared to the analytical calculation (blue line). Here, we use (a) log-scale resistance and (b) reactance with linear-scale frequency to give a more clear demonstration.

well as a more reliable analysis of the stability of the composite structure.

Based on the given system load admittance, stability of this structure can be investigated by interpreting the stability constraint of the active load in a three dimensional impedance space, thus, representing the generalized source impedance and load admittance which encompass the full range of possible plants. The generalized impedance/admittance is defined as the bounded region. As mentioned earlier, in addition to the capabilities of deriving the design specification for a given source impedance or load admittance to ensure robust stability, this technique can also be used to explicitly address the operating points and parameter variations. The stability constraint of the active load specified by the EPSC is depicted in Fig. 3.12 and the simulation impedance obtained from the practical NIC circuit with varying terminated inductance are also plotted. Note that the corresponding ideal cases are ignored here, since they have already been proved to be stable by inspection the consistency between this technique and prior stability criteria as discussed before. Clearly the stability margins for the simulated cases are significantly reduced comparing with the ideal cases. This is primarily due to parasitics and non-linearity of the active NIC circuit. Nevertheless, stability can still be achieved over a

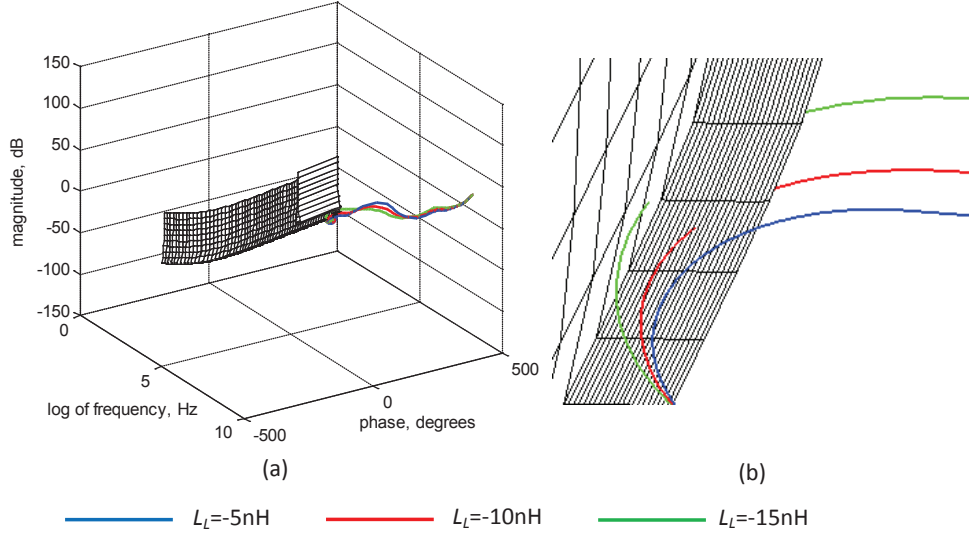


Figure 3.12: (a) Stability constraint of the NIC load in the impedance space. As before, a three dimensional space is depicted where the x-axis is frequency s , the y-axis is phase PM in degree, and z-axis is magnitude GM in dB. The simulated impedance of the practical NIC circuit are plotted. (b) Magnification of the stability constraint around the intersection region. It is shown that the impedance profiles for both the $10nH$ (red curve) and $15nH$ (green curve) cases penetrate the forbidden region, which means they are unstable, whereas the $5nH$ case (blue curve) is stable because there is no intersection with the forbidden region.

reasonable range of NIC input inductance values. Moreover, it is noted that the stability will be improved as the NIC input inductance is decreased (hence the equivalent negative inductance is increased) that agrees with the theory.

Subsequently, the complex impedance parameters may then be used to determine the effective permeability of the bulk medium in a similar manner to Eq. (3.5), such that

$$\mu_r(s) = 1 - \mu_b N \frac{j\omega S^2}{Z(s)}, \quad (3.15)$$

where $Z(s) = Z_s(s) + 1/Y_l(s)$ is the simulated impedance of the loops with the NIC loads. These results are shown in Fig. 3.13. For comparison, both stable and unstable cases are plotted corresponding to the different NIC input inductances ($L_N = (5, 10, 15)nH$). The introduction of a realistic NIC circuit reduces the range of stable negative impedance

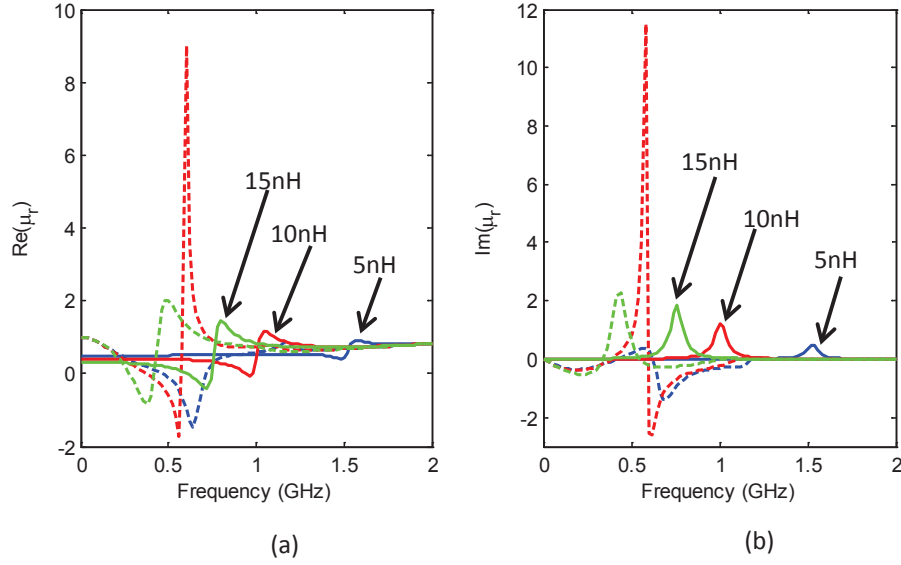


Figure 3.13: (a) Real and (b) imaginary parts of the effective permeability. For the $L_N = (5, 10, 15)nH$, the simulation results are plotted with dashed lines whereas the ideal cases are solid. From these results we can see that a stable MNG performance may be achieved over a relatively large frequency bandwidth (for the $L_N = 5nH$), which are not present in the corresponding ideal case. Moreover, it is shown that the magnetic gain ($Im(\mu_r) < 0$) can be achieved at certain frequencies for the simulated case due to the parasitics while the ideal case only exhibits losses ($Im(\mu_r) > 0$).

values, and so it is not possible to achieve quite the range and bandwidth of negative or near-zero permeability. However, for the $L_N = 5nH$ case, the medium does exhibit relatively MNG properties over a reasonably large bandwidth, and certainly more than what would be possible with a passive medium. Furthermore, due to the parasitics in the practical NIC circuits, it is interesting to see that there is a magnetic gain created around the MNG frequency band which is exhibited as negative imaginary permeability, thus make the design of stable broadband metamaterials with gain achievable for engineers.

We also note that the error between the simulated and ideal cases leads to a smaller range of stable NIC load inductors, and so it is quite conceivable that, with the use of improved fabrication techniques and higher quality transistors, and in particular MMIC technology, the contribution of the parasitics and nonlinearities could be significantly reduced. This could improve stability quite considerably while reducing the unnecessary

parasitic effects. However, the parasites can be useful in the design of active metamaterials to achieve some specific goals such as the gain increasing, thus they should be considered for retaining in those cases.

3.5 Wave Propagation in Actively-Loaded Medium

Wave propagation in active metamaterials may exhibit different phenomena from metamaterials based on ring resonators (SRRs) or other passively-loaded medium. Starting from one-dimensional periodic actively-loaded loop array including both coaxial and coplanar cases, their wave dispersion characteristics are analytically derived and investigated to present the novel properties. Subsequently, the equivalent circuit of the effective medium with the active inclusions based on the transmission line (TL) model is then presented. Accounting all the interactions, we can predict the wave propagation in the active medium with non-Foster loads as well as the effective magnetic properties. Verified by the numerical simulations, we will further extend to the mechanism of how powered active unit cells incorporating both NIC circuits and negative resistance amplifiers can reduce the loss in the materials while retaining the same magnetic properties as the negative parallel-RLC loaded metamaterials [6, 12]. Henceforth, the way to achieve zero-loss and broadband active metamaterials is analytically provided.

3.5.1 Dispersion Characteristics

In this section, we start our analysis on the wave propagation in periodic active arrays by considering the one-dimensional case of an infinitely long line of magnetically-coupled identical non-Foster loaded loops. As proposed by Shamonina *et al.* [41], waves propagating in an array of magnetically-coupled resonators such as SRRs [1], and capacitively-load loops [42] are referred to as magneto-inductive (MI) waves, since the coupling is due to the induced voltages. Replacing the unit cells by the actively-loaded loops, thus, the dispersion equation of an one-dimensional actively-loaded loop array can be analytically

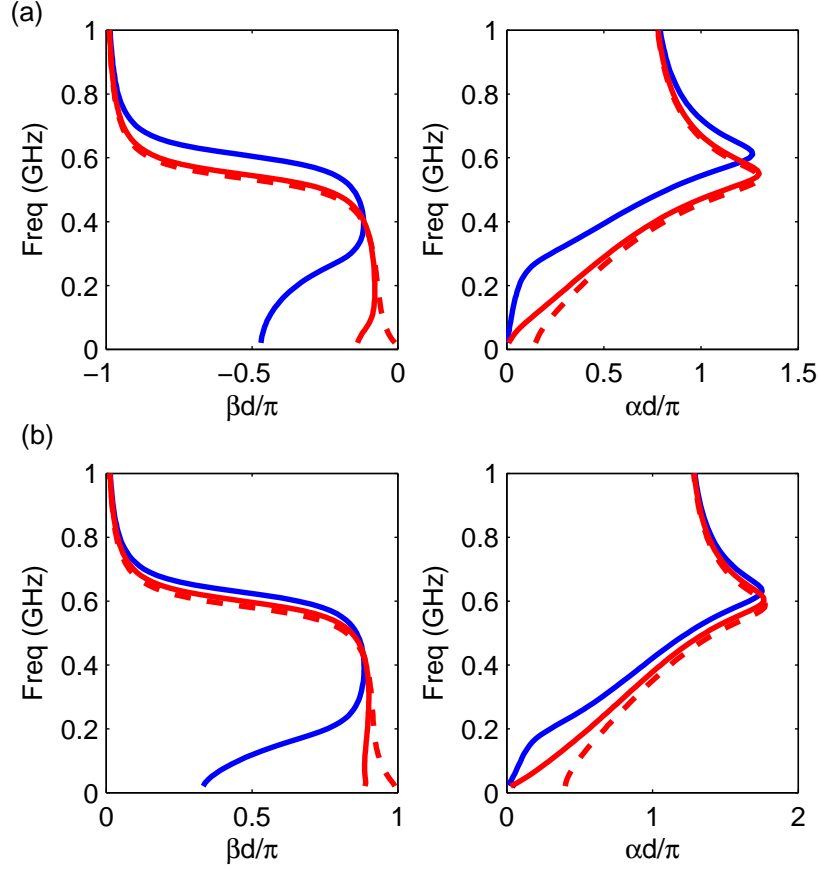


Figure 3.14: Dispersion characteristics of 1D infinite periodic active loop arrays. (a) The active array consist of periodic coaxial non-Foster loaded loops, where each load is defined as a parallel-RLC circuit with $R_L = -1000\Omega$, and $C_L = -2pF$, and $L_L = [-34(blue), -43(red), -44(red - dashed)]nH$. (b) The coplanar array, only replacing the load inductance by $L_L = [-32(blue), -35(red), -36(red - dashed)]nH$.

derived in a similar manner to Eq. (3.4)

$$Z_s + 2j\omega \sum_{m=1}^{+\infty} M_m \cosh(m\gamma_{MI}d) = 0, \quad (3.16)$$

where $Z_s = Z_0 + Z_L$ is the series impedance of the loop circuit, d is the lattice spacing, M_m is the mutual coupling between two loops a distance md from each other, and γ_{MI} is the propagation constant.

Assuming the same physical definitions for each loop, we shall compare the dispersion

characteristics of 1D periodic actively-loaded loop arrays for both coaxial and coplanar cases as depicted in Fig. 3.14. The active load consists of a parallel negative RLC circuit with load resistance and capacitance defined as $R_L = -1000\Omega$ and $C_L = -2pF$ respectively. The negative inductance is varied from stable to unstable cases, while the range of stable values is given by Eq. (3.7). For an infinite periodic coaxial array with 10mm spacing, it is straightforward to derive the stable range of the load inductance as $0 > L_L > -43.9nH$ [6]. The corresponding dispersion diagrams with varying load inductances are plotted in Fig. 3.14 (a) in terms of wave number (β) and attenuation coefficient (α), respectively. It is noted that an actively-loaded coaxial array allows only the MI wave with negative wave number to propagate over the frequency of interest, but it supports both forward and backward wave under the stable conditions which is totally different from the passive resonator arrays [42]. Furthermore, it is not difficult to see that the attenuation coefficient reaches the maximum at the angular resonant frequency of the parallel-RLC load

$$\omega_L = 1/\sqrt{L_L C_L}. \quad (3.17)$$

For the coplanar case, however, similar phenomena can be observed as shown in Fig. 3.14 (b), except that the wave propagating in an actively-loaded coplanar array exhibits positive wave number within the same frequency band.

Now we shall further our analysis to the effective medium embedded with actively-loaded loop arrays. The physical model assumed consists of an EM wave propagating in a waveguide past a one-dimensional loop array with non-Foster loads. The EM wave is polarized so that its magnetic field may interact with the active inclusions, which then provide an effective magnetic medium. In a similar manner to Refs. [43] and [44], Fig. 3.15 shows the equivalent circuit, which consist of a pair of coupled lines. The active inclusions are represented as a 1D lattice of lumped-element circuits of period d , coupled to each other by mutual inductance M_m . Such a line supports MI wave as discussed before. The EM wave is represented by a lossless transmission line of the same period, with series inductance $L = \mu_0 d$ and shunt capacitance $C = \epsilon_0 d$ in each section of length

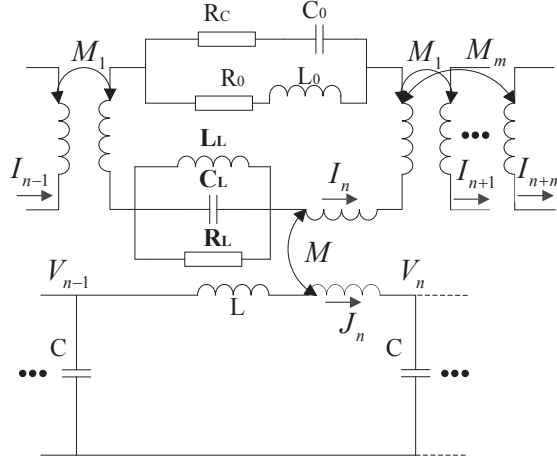


Figure 3.15: Equivalent circuit for a transmission line loaded with 1D non-Foster loaded loop array.

d , where μ_0 and ε_0 are the permeability and permittivity of free space. The coupling between the active inclusions and the EM wave is modeled by mutual inductance M .

A mathematical model corresponding to Fig. 3.15 may be constructed by using Kirchhoff's voltage law to generate a set of equations relating the voltage V_n and currents I_n and J_n in the n th section to values in other sections, thus, we obtain

$$\begin{aligned} Z_s I_n + j\omega \sum_{m=1}^{+\infty} M_m (I_{n-m} + I_{n+m}) + j\omega J_n &= U_n \\ j\omega L J_n + j\omega M I_n &= V_{n-1} - V_n \\ V_n &= \frac{J_n - J_{n+1}}{j\omega C}. \end{aligned} \quad (3.18)$$

Assuming the traveling wave solutions $I_n = I_0 \exp(-n\gamma d)$, and $J_n = J_0 \exp(-n\gamma d)$, the dispersion equation of the effective medium can be thereby obtained after a fair amount of algebraic manipulations

$$\left[Z' + \sum_{m=1}^{+\infty} k_m \cosh(m\gamma d) \right] \left[1 - \frac{2\omega_0^2}{\omega^2} + \frac{2\omega_0^2}{\omega^2} \cosh(\gamma d) \right] = q^2. \quad (3.19)$$

Here, $\omega_0 = 1/\sqrt{LC}$ is the angular resonant frequency of free space, $Z' = Z_s/(j\omega L_0)$ is the normalized impedance of the loop, $k_m = 2M_m/L_0$ is the coupling coefficient between

the active inclusions, and $q^2 = M^2/LL_0$ is the normalized coupling coefficient between the EM and MI waves. This equation may be solved for any value of ω , allowing the complex propagation constant γ to be found.

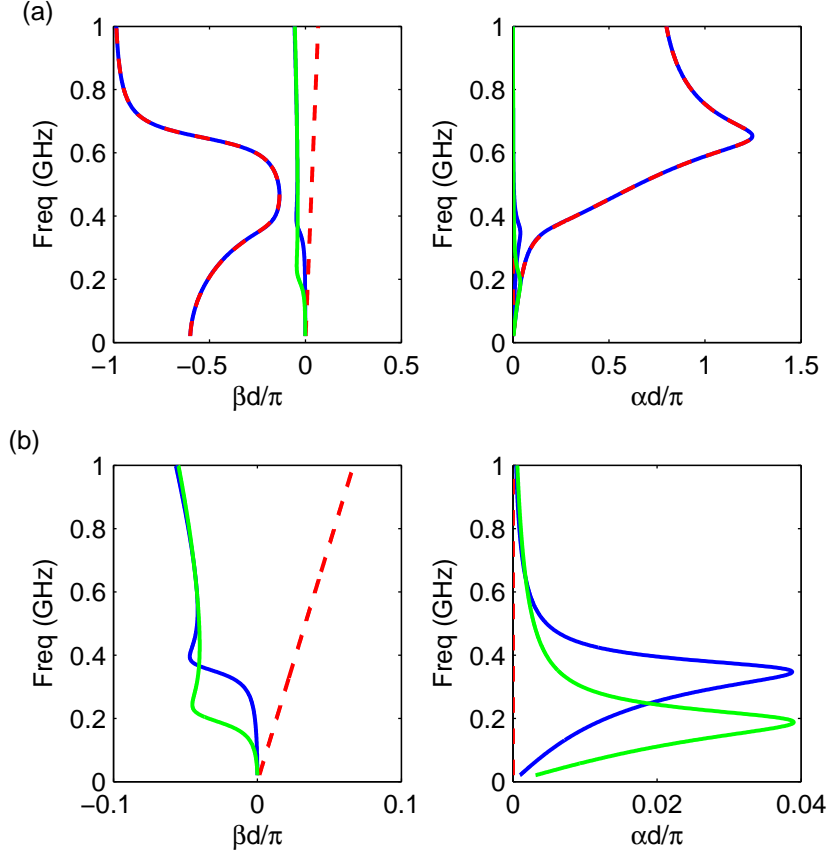


Figure 3.16: (a) Dispersion diagrams for the model of Fig. 3.15 with (I) $q^2 = 0.6$ and $k_m \neq 0$ (blue line), (II) $q^2 = 0$ and $k_m \neq 0$ (red dashed line), and (III) $q^2 = 0.6$, $M_m = 0$ (green line). For the case (I) and (II), it is shown that two branches can be obtained, one correspond to an EM-like wave, the other to an MI-like wave. (b) The dispersion diagrams of the EM branches for all cases are again plotted, respectively.

Fig. 3.16 shows the frequency variations of the dispersion characteristics for different cases, for the example a periodic coaxial array is employed as the active inclusions. Clearly, when the loop array elements are coupled ($k_m \neq 0$), the dispersion equation may yield an ω - γ program with two branches. In particular, for the parameters $q^2 = 0$ and $k_m \neq 0$, the left side of Eq. (3.19) yields two waves propagating independently of

each other, one is the EM wave in free space and the other is the MI wave. Conversely, if the loop array are uncoupled ($k_m = 0$), it is shown that only the EM-like wave can propagate. Furthermore, by comparing the case (I) and (II), it is interesting to see that the interaction between the EM wave and the loop array may affect the EM branch only thus altering the effective medium parameters, without significantly perturbing the MI-like wave supported by the array. The dispersion characteristic of the EM branches for all cases are detailed in Fig. 3.16 (b) which clearly shows that the effective medium consisting of an actively-loaded coaxial loop array supports both forward and backward waves, no matter whether the elements are coupled or not.

3.5.2 Effective Medium Properties

As proposed by Syms *et al.* [43], a new method for finding the effective permeability of metamaterials is given from the the dispersion equation as

$$\mu_r = \left(\frac{\gamma}{\gamma_{EM}} \right)^2, \quad (3.20)$$

where γ is the propagation constant of the EM branch of the effective medium which can be numerically solved from Eq. (3.19), and $\gamma_{EM} = j\omega\sqrt{\mu_0\epsilon_0}$ is the corresponding value for an unloaded EM wave. The frequency dependence of the effective medium parameters obtained from Eq. (3.20) (case I) for the same physical definitions as before is shown in Fig. 3.17, which is excellent agreement with the results from Eq. (3.5) (case II). Here, two sets of data are shown for μ_r : with coupling between the elements ($k_m \neq 0$) and without coupling ($k_m = 0$). The results clearly show the effect of the mutual coupling on the effective medium parameters.

Now we shall research in-depth the relation between the wave dispersion characteristics and the effective medium properties. Replacing the propagation constant γ by its

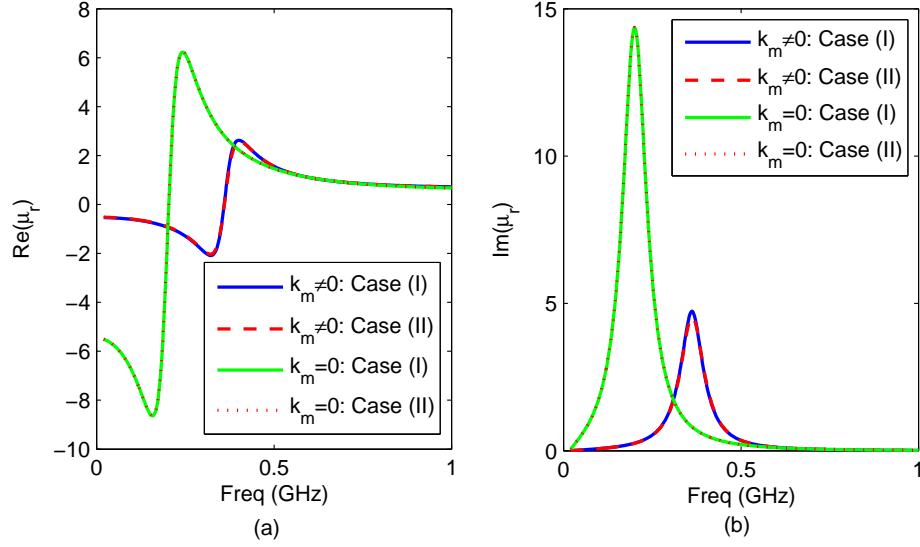


Figure 3.17: (a) Real and (b) imaginary parts of the relative permeability extracted from the effective medium. The case I and II correspond to Eq. (3.20) and Eq. (3.5), respectively.

expansion $\gamma = \alpha + j\beta$, therefore, the relative permeability $\mu_r = \mu'_r - j\mu''_r$ is equal to

$$\mu_r = \frac{\beta^2 - \alpha^2 - 2j\alpha\beta}{\omega^2 \mu_0 \varepsilon_0}, \quad (3.21)$$

which simply yields the real and imaginary part of the relative permeability

$$\begin{aligned} \mu'_r &= \frac{\beta^2 - \alpha^2}{\omega^2 \mu_0 \varepsilon_0} \\ \mu''_r &= \frac{2\alpha\beta}{\omega^2 \mu_0 \varepsilon_0}. \end{aligned} \quad (3.22)$$

Clearly, in order to achieve the left-handed (LH) magnetic properties ($\mu'_r < 0$), the following condition must be satisfied

$$0 < |\beta| < |\alpha|. \quad (3.23)$$

Meanwhile, due to the positive α and negative β as depicted in Fig. 3.16, the imaginary magnetic susceptibility sign becomes negative ($\mu''_r < 0$), thus the effective medium

exhibits losses at all frequencies. In general, the phase velocity $v_p = \omega/\beta$, associated with the direction of phase propagation, has to be negative in the LH medium while the attenuation coefficient is always positive without additional power compensation [45]. This result implies that the LH magnetic behaviour always accompanies a material loss. Particularly, it is noted that for more negative μ'_r , a larger attenuation coefficient α is required, thus resulting in a metamaterial with higher losses.

3.5.3 Design of Zero-Loss and Broadband Active Metamaterials

One may now pose the question: is there any solution available to achieve a material that not only has zero magnetic loss but also exhibits broadband magnetic behaviour? The answer is that, it is possible when the wave propagation losses are overcome by additional powered devices while keeping the phase propagation unperturbed (see, e.g., Ref. [5, 46]), since it has been asserted that the phenomena of the negative medium parameters can be explained by using nothing more complicated than the wave propagation methods based on the transmission line theory [44].

Here, we may henceforth propose a technique by applying both the NIC circuits and negative resistance amplifiers as the active loads to design a zero-loss and broadband metamaterial. Fig. 3.18 depicts the corresponding transmission line model which consists of an infinite chain of actively-loaded unit cells. For each unit cell, a parallel negative LC circuit ($L_L \parallel C_L$) is used to achieve the broadband magnetic properties [6, 12], whilst a negative resistance amplifier is employed as the power supply to excite a MI wave and gradually transfer its power to an EM wave. As suggested in Ref. [47], the negative amplifier may be represented as a negative resistor R_L which is also used to maintain the stability, with a shunt current source i_n . Such that, the characteristic equation relating the current source and currents I_n and J_n in the n th section to values in other sections

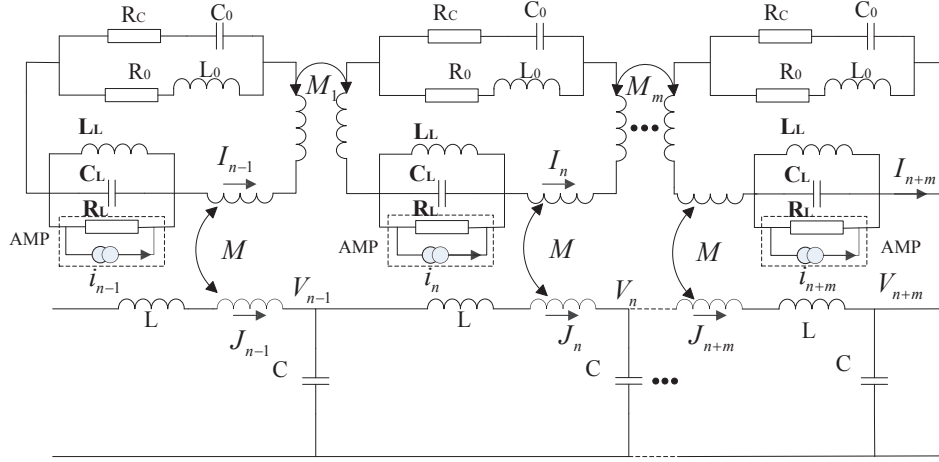


Figure 3.18: Transmission line model of a 1D zero-loss and broadband metamaterials.

is given by

$$Z_s I_n + j\omega \sum_{m=1}^{+\infty} M_m (I_{n-m} + I_{n+m}) + j\omega J_n = i_n \frac{Z_s Z_p}{Z_0},$$

$$j\omega L J_n + j\omega M I_n = \frac{J_{n+1} + J_{n-1} - 2J_n}{j\omega C}, \quad (3.24)$$

where $Z_p = Z_0 \parallel Z_L$, and $Z_s = Z_0 + Z_L$ are the parallel and series impedance of a loaded loop, respectively. Similarly, the dispersion equation in the effective medium can be obtained, which is the same as Eq. (3.19). Therefore, the same frequency variations of the material properties shall be derived as depicted in Fig. 3.17 from Eq. (3.20), which clearly exhibits a magnetic medium with high losses. It should be noted that, the above analysis is not complete since it is assumed that only a single current source in the loop array is used as the excitation, resulting in an evanescent wave propagating in the medium. In our case, however, it is described that each element of the loop array is load with an negative resistance amplifier which provides a current source, then the combined effects due to the multiple excitations must be accounted. Starting by considering the effect of the the current sources on the MI wave, as described in Ref.[20], we here assume an infinite 1D array with $-\infty < n < +\infty$, containing a single current source $i_n = i_\delta \exp[j(\omega t + \phi_n)]$ at the element n . Since the MI wave will propagate from the source

to either side, the MI wave solution can be rewritten as $I_m = I_n \exp(-|n - m|\gamma_{MI}d)$. Substituting into Eq. (3.24), it is straightforward to derive the current response in the n th element

$$I_n = -\frac{Z_s Z_p i_\delta \exp[j(\omega t + \phi_n)]}{2j\omega Z_0 \sum_{m=1}^{+\infty} M_m \sinh(m\gamma_{MI}d)}, \quad (3.25)$$

where γ_{MI} is the propagation constant of the MI wave obtained from Eq. (3.19). Here, we should note that, the induced voltage from the EM wave are ignored due to the little effect of the interaction between the EM and MI waves on the wave propagating in the loop array as discussed before. Consequently, the current response at the m th element due to the source at element n can be obtained. Moreover, since it is clear that there is uniformity in the effect from different sources due to the periodicity of the loop array, the overall response in element n can be found by summing independent contributions from all sources, such that

$$I_n = -\frac{Z_s Z_p i_\delta \sum_{m=-\infty}^{+\infty} \exp[j(\omega t + \phi_n) - |m - n|\gamma_{MI}d]}{2j\omega Z_0 \sum_{m=1}^{+\infty} M_m \sinh(m\gamma_{MI}d)}. \quad (3.26)$$

Provided that each current source has the same initial phase defined as $\phi_n = \phi$ (with $-\infty < n < +\infty$), we can rewrite the above as

$$I_n = -\frac{Z_s Z_p i_\delta \exp[j(\omega t + \phi_n)]}{2j\omega Z_0 \tanh(\gamma_{MI}d/2) \sum_{m=1}^{+\infty} M_m \sinh(m\gamma_{MI}d)}. \quad (3.27)$$

which clearly shows that the overall current response for each element is independent of the position in an infinite array.

We may now apply this result to the investigation of the current response in the EM wave due to the current sources in 1D infinite loop arrays. Note that, a single current I_n in the n th element will excite a pair of wave into the EM line, traveling in either direction. With the assumption $J_m = J_n \exp(-|m - n|\gamma_{EM}d)$, the corresponding response J_n can

be thereby derived from Eq. (3.18)

$$J_n = \frac{\omega^2 MCI_n}{2 - 2\exp(-\gamma_{EM}d) - \omega^2 LC}, \quad (3.28)$$

where γ_{EM} is the propagation constant of the EM branch described by Eq. (3.19). Subsequently, the current response in the n th section of the EM wave excited by all the current sources can be similarly derived

$$J_n = \frac{\omega^2 MCI_n}{\tanh(\gamma_{EM}d/2) [2 - 2\exp(-\gamma_{EM}d) - \omega^2 LC]}, \quad (3.29)$$

where I_n is given by Eq. (3.27). Clearly, the EM wave has the same current response for each section in the effective medium, thus, overcoming the wave propagation loss ($\alpha = 0$). However, it is not difficult to see that the phase propagation β is not altered. Therefore, the same phenomena due to the negative parameters can be observed but it will not decay as the wave propagates, hence we can have the following expression of the relative permeability

$$\mu' < 0, \mu'' = 0, \quad (3.30)$$

which is not possible for conventional metamaterials due to the wave propagation theory. Since the broadband magnetic properties has been verified by Refs. [6, 12], we therefore have analytically proposed a technique to achieve a zero-loss and broadband metamaterials. Moreover, we may now quantify the relation between the current sources and the MI and EM waves, represented by I_n and J_n , to better illustrate the effects of the negative resistance amplifier loading. The ratio of the magnitude of the wave currents to the source current is defined as

$$\begin{aligned} T_{MI} &= \frac{|I_n|}{|i_n|} \\ T_{EM} &= \frac{|J_n|}{|i_n|}. \end{aligned} \quad (3.31)$$

The frequency dependence of these quantities is plotted in Fig. 3.19, for (a) the MI wave

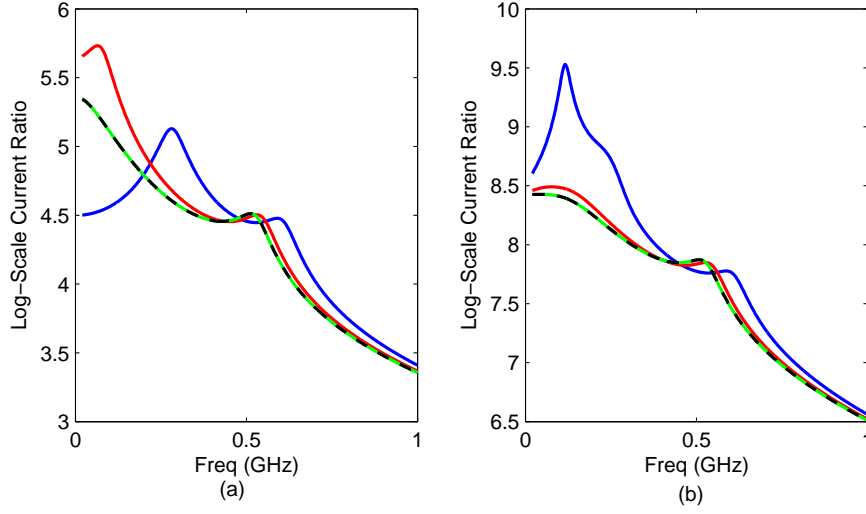


Figure 3.19: The ratio of the magnitude of the currents (a) I_n (the MI wave) and (b) J_n (the EM wave) to the source current i_n under stable and unstable conditions. Once again, the parameters are generally as before, and results are computed for an array loaded with negative resistance amplifier where $R_L = -1000\Omega$, and NIC circuits, in that $C_L = -2pF$ for all cases, and $L_L = [-34(\text{blue}), -43(\text{red}), -44(\text{green} - \text{dashed}), -45(\text{black})]nH$.

ratio T_{MI} and (b) the EM wave ratio T_{EM} . Four sets of data are provided with the varying NIC load inductance L_L from stable and unstable cases. Clearly, for both the MI and EM waves, it is shown that their currents have been greatly amplified due to the multiple excitations and the EM wave exhibits a much higher level in the magnitude. However, it is interesting to note that for both waves, the current ratio of the unstable cases tends to remain unchanged when varying the load inductance, as compared to the change of the dispersion characteristics plotted in Fig. 3.14.

Furthermore, we should note that the above analysis is based on an infinite system which is certainly not available in practice. For a finite loop array based medium, an imittance matrix will be provided by relating the sources and the current response of the EM wave in different sections. In such case, it can be predicted that the EM wave current must actually depend on position in a finite system. Thus, the wave propagation loss can only be reduced but not canceled, resulting in a material with low losses. Note that, as the section number increases, the material properties should tend to the infinite

case as another expectation. Finally, it is possible to extend our analysis to 2D and 3D cases following the proposed approach.

3.6 Conclusions

The characteristics of non-Foster loaded metamaterials is studied in this chapter. Based on the the circuit model of the effective medium, a few criteria are given to investigate the stability of the actively-loaded medium. Note that, although the Routh-Hurwitz criterion is able to provide the analytical design rules for broadband metamaterials, it is not suitable for practical applications due to the parasitics and nonlinearities of the practical NIC circuits, whilst the Nyquist stability criterion is found as a method to solve these problems. However, there are also drawbacks associated with the Nyquist stability criterion which restrict its applications. One of them is that it is not design oriented, only can test the stability of a single point, such that, it is unable to represent the effects of the parameter uncertainties. In our work, an immitance-based stability analysis technique is applied in the design of a material with broadband MNG or MNZ properties which is the extension of Nyquist stability criterion, in that a novel stability criterion named the Exponential Peaking Stability Criterion (EPSC) is proposed which imposes a forbidden region in the complex plane, so as to give the design specifications of an arbitrary load for a given unloaded loop structure. It is shown that the EPSC is less conservative than all the other criteria proposed for ensuring robust stability. By applying the EPSC, the design of broadband active metamaterials is demonstrated with the practical NIC circuits. The corresponding material properties are also depicted as compared to the ideal cases.

Subsequently, the wave propagation in the actively-loaded medium is investigated based on the transmission line theory. Starting from the 1D case of an infinite set of magnetically coupled identical non-Foster loaded loops, the dispersion characteristic of the so-called magneto-inductive (MI) wave are explored, in terms of the coaxial and

coplanar cases, respectively. Furthermore, waves propagating in the effective medium embedded with 1D loop arrays are studied further to derive the dispersion equation. We should note here that there are two solution to this equation, one corresponding to an EM-like wave; the other to an MI-like wave. The material properties can then be extracted from the EM wave, which are in excellent agreement with the other proposed methods. Moreover, by inspection of the relation between the wave propagation and the effective medium properties, we give an analytical method to design zero-loss and broadband metamaterials based on the combination of the NIC circuits and negative resistance amplifiers. Such that, the NIC circuit is used to generate the negative LC elements to achieve the broadband properties, as the negative resistance amplifier provides the additional power sources to overcome the wave propagating loss, thus eliminating the material loss while retaining the phenomena due to the negative parameters.

References

- [1] J. Pendry, A. Holden, D. Robbins, and W. Stewart, "Magnetism from conductors and enhanced nonlinear phenomena," *IEEE Trans. Microw. Theory Tech.*, vol. 47, p. 2075, 1999.
- [2] E. Ozbay, K. Aydin, E. Cubukcu, and M. Bayindir, "Transmission and reflection properties of composite double negative metamaterials in free space," *IEEE Trans. Antennas Propag.*, vol. 51, p. 2592, 2003.
- [3] F. Bilotti, A. Toscano, and L. Vegni, "Design of spiral and multiple split-ring resonators for the realization of miniaturized metamaterial samples," *IEEE Trans. Antennas Propag.*, vol. 55, no. 8, pp. 2258–2267, 2007.
- [4] S. Tretyakov, "Meta-materials with wideband negative permittivity and permeability," *Microwave Opt. Technology Lett.*, vol. 31, pp. 163–165, 2001.
- [5] Y. Yuan, B. Popa, and S. A. Cummer, "Zero loss magnetic metamaterials using powered active unit cells," *Opt. Exp.*, vol. 17, p. 16135, 2009.
- [6] K. Z. Rajab, Y. Hao, D. Bao, C. G. Parini, C. Vazquez, J. Philippakis, and M. Philip-

- pakis, “Stability of active magnetoinductive metamaterials,” *J. Appl. Phys.*, vol. 108, p. 054904, 2010.
- [7] S. Hrabar, I. Koris, I. Krois, and A. Kirichenko, “Negative capacitor paves the way to ultra-broadband metamaterials,” *Appl. Phys. Lett.*, vol. 99, p. 254103, 2011.
- [8] F. Auzanneau and R. Ziolkowski, “Theoretical study of synthetic bianisotropic materials,” *Journal of electromagnetic waves and applications*, vol. 12, no. 3, pp. 353–370, 1998.
- [9] R. Zislowski, “The design of maxwellian absorbers for numerical boundary conditions and for practical applications using engineered artificial materials,” *Antennas and Propagation, IEEE Transactions on*, vol. 45, no. 4, pp. 656–671, 1997.
- [10] S. A. Tretyakov and T. Kharina, “The perfectly matched layer as a synthetic material with active inclusions,” *Electromagnetics*, vol. 20, no. 2, pp. 155–166, 2000.
- [11] S. A. Tretyakov and S. I. Maslovski, “Veselago materials: What is possible and impossible about the dispersion of the constitutive parameters,” *IEEE Antennas and Propagation Magazine*, vol. 49, pp. 37–43, 2007.
- [12] K. Z. Rajab, Y. Fan, and Y. Hao, “Characterization of active metamaterials based on negative impedance converters,” *J. Opt.*, vol. 14, p. 114004, 2012.
- [13] L. Jelinek and J. Machac, “An fet-based unit cell for an active magnetic metamaterial,” *IEEE Antennas and Wireless Propag. Lett.*, vol. 10, pp. 927–930, 2011.
- [14] R. Syms, L. Solymar, and I. Young, “Three-frequency parametric amplification in magneto-inductive ring resonators,” *Metamaterials*, vol. 2, pp. 122–134, 2008.
- [15] S. Tretyakov, F. Mariotte, C. R. Simovski, T. G. Kharina, and J. P. Heliot, “Analytical antenna model for chiral scatterers: comparison with numerical and experimental data,” *IEEE Trans. Antennas Propag.*, vol. 44, pp. 1006–1014, 1996.
- [16] C. R. Simovski, A. J. Viitanen, and S. A. Tretyakov, “Resonator mode in chains of silver spheres and its possible application,” *Phys. Rev. E*, vol. 72, p. 066606, 2005.
- [17] P. A. Belov and C. R. Simovski, “Subwavelength metallic waveguides loaded by uniaxial resonant scatterers,” *Phys. Rev. E*, vol. 72, p. 036618, 2005.
- [18] W. H. Weber and G. W. Ford, “Propagation of optical excitations by dipolar interactions in metal nanoparticle chains,” *Phys. Rev. B*, vol. 70, p. 125429, 2004.

- [19] O. Zhuromskyy, O. Sydoruk, E. Shamonina, and L. Solymar, “Slow waves on magnetic metamaterials and on chains of plasmonic nanoparticles: Driven solutions in the presence of retardation,” *J. Appl. Phys.*, vol. 106, p. 104908, 2009.
- [20] Y. Fan, K. Z. Rajab, and Y. Hao, “Noise analysis of broadband active metamaterials with non-foster loads,” *J. Appl. Phys.*, vol. 113, p. 233905, 2013.
- [21] Y. Hao and R. Mittra, *FDTD Modelling of Metamaterials: Theory and Applications*. Artech House, 2009.
- [22] E. J. Routh, *A Treatise on the Stability of a Given State of Motion, Particularly Steady Motion*. London: Macmillan and Co., 1877.
- [23] A. Hurwitz, “On the conditions under which an equation has only roots with negative real parts,” *Selected Papers on Mathematical Trends in Control Theory* (R. Bellman and R. Kalaba, eds.), vol. 65, 1964.
- [24] A. Boardman, Y. Papoport, N. King, and V. Malnev, “Creating stable gain in active metamaterials,” *J. Opt. Soc. Am. B.*, vol. 24, p. A53, 2007.
- [25] B. Nistad and J. Skaar, “Causality and electromagnetic properties of active media,” *Phys. Rev. E*, vol. 78, p. 036603, 2008.
- [26] A. Govyadinov and V. Podolskiy, “Active metamaterials: Sign of refractive index and gain-assisted dispersion management,” *Appl. Phys. Lett.*, vol. 91, p. 191103, 2007.
- [27] S. Sudhoff, S. Glover, P. Lamm, D. H. Schmucker, and D. Delisle, “Admittance space stability analysis of power electronic systems,” *Aerospace and Electronic Systems, IEEE Transactions on*, vol. 36, no. 3, pp. 965–973, 2000.
- [28] C. L. Philips and R. D. Harbor, *In Feedback Control Systems*. Upper Saddle River, NJ: Prentice-Hall, 2000.
- [29] J. G. Linvill, “Transistor negative impedance converters,” *Proc. IRE.*, vol. 41, pp. 725–729, 1953.
- [30] S. Sudhoff and S. Glover, “Three-dimensional stability analysis of dc power electronics based systems,” in *Power Electronics Specialists Conference, 2000. PESC 00. 2000 IEEE 31st Annual*, vol. 1, 2000, pp. 101–106.
- [31] X. Feng, Z. Ye, K. Xing, F. Lee, and D. Borojevic, “Impedance specification and

- impedance improvement for dc distributed power system,” in *Power Electronics Specialists Conference, 1999. PESC 99. 30th Annual IEEE*, vol. 2, 1999, pp. 889–894.
- [32] X. Feng, J. Liu, and F. Lee, “Impedance specifications for stable dc distributed power systems,” *Power Electronics, IEEE Transactions on*, vol. 17, no. 2, pp. 157–162, 2002.
- [33] R. Chane, Y. Lee, S. Sudhoff, and E. Zivi, “Evolutionary optimization of power electronics based power systems,” *Power Electronics, IEEE Transactions on*, vol. 23, no. 4, pp. 1907–1917, 2008.
- [34] S. Sudhoff and J. Crider, “Advancements in generalized immittance based stability analysis of dc power electronics based distribution systems,” in *Electric Ship Technologies Symposium (ESTS), 2011 IEEE*, 2011, pp. 207–212.
- [35] R. Middlebrook, “Input filter considerations in design and application of switching regulators,” *IEEE IAS Annual Meeting*, 1976.
- [36] C. Wildrick, F. Lee, B. Cho, and B. Choi, “A method of defining the load impedance specification for a stable distributed power system,” *Power Electronics, IEEE Transactions on*, vol. 10, no. 3, pp. 280–285, 1995.
- [37] S. Skogestad and I. Postlethwaite, *Multivariable Feedback Control-Analysis and Design*. Chichester, UK: Wiley, 1998.
- [38] S. Vesti, T. Suntio, J. Oliver, R. Prieto, and J. Cobos, “Impedance-based stability and transient-performance assessment applying maximum peak criteria,” *Power Electronics, IEEE Transactions on*, vol. 28, no. 5, pp. 2099–2104, 2013.
- [39] Advanced Design System 2013, Agilent Technologies, URL: <http://www.agilent.com/>.
- [40] Ansoft *HFSSTM* 12.1, Ansoft, Inc. URL: <http://www.ansoft.com/>.
- [41] E. Shamonina, V. A. Kalinin, K. H. Ringhofer, and L. Solymar, “Magnetoinductive waves in one, two, and three dimensions,” *J. Appl. Phys.*, vol. 92, p. 6252, 2002.
- [42] M. Wiltshire, E. Shamonina, I. Young, and L. Solymar, “Dispersion characteristics of magneto-inductive waves: Comparison between theory and experiment,” *Electron. Lett.*, vol. 39, p. 215, 2003.
- [43] R. Syms and L. Solymar, “Effective permeability of a metamaterial: Against con-

- ventional wisdom,” *Appl. Phys. Lett.*, vol. 100, no. 124103, 2012.
- [44] R. Syms, E. Shamonina, V. Kalinin, C. G. Parini, and L. Solymar, “A theory of metamaterials based on periodically loaded transmission lines: Interaction between magnetoinductive and electromagnetic waves,” *J. Appl. Phys.*, vol. 97, p. 064909, 2005.
- [45] C. Caloz and T. Itoh, *Electromagnetic Metamaterials: Transmission Line theory and Microwave Applications*. NJ: Wiley-Interscience publication, 2006.
- [46] B. Popa and S. Cummer, “An architecture for active metamaterial particles and experimental validation at rf,” *Microwave Opt. Technology Lett.*, vol. 49, pp. 2574–2577, 2007.
- [47] E. Rostas and F. Hulster, “Microwave amplification by means of intrinsic negative resistances,” *Proceeding of the IEE- Part B: Radio and Electronic Engineering*, vol. 105, pp. 665–672, 1958.

Chapter 4

Noise Analysis of Active Metamaterials with Non-Foster Loads

Active metamaterials loaded with non-Foster inclusions may exhibit broadband and low-loss material properties, as compared to their passive counterparts. However, the study of their noise performance still remains to be explored. In addition to the Johnson-Nyquist noise from lossy conductors, active components used for the design of negative impedance converters (NICs) will give rise to noise as well. In this chapter, a general analytical model is developed for the prediction of the noise performance of broadband, stable active metamaterials based on negative impedance converters (NICs). The noise performance is analyzed in relation to stability, and the effective material properties. The techniques developed in this chapter can be applied generally to metamaterials for which equivalent circuit models exist, and results are shown demonstrating the power spectral density (PSD) and the noise figure of the specific case of an active metamaterial consisting of loaded loop arrays. Results are compared to and verified with circuit simulations.

4.1 Background

As it is well known, noise in any electrical systems must be given enough attention since it may have tremendous impacts on practical applications. A typical example is thermal noise, originating from the random motion of free electrons inside conductors [1]. This leads to temporary accumulation of electrons at one or the other end, and consequently a fluctuating voltage appears between the ends [2]. The theoretical explanation of thermal noise was offered by Nyquist [3]. For lumped-element circuits, the thermal noise strength determines the ultimate limit on a circuit's ability to process weak signals. As for passive metamaterials based on periodic and electrically-small resonant structures, Syms *et al.* proposed the idea of “noise waves” to describe the noise performance of this medium. Therein, noise from conductive material of a single unit cell was taken into consideration, and coupled with each other. However, active metamaterials loaded with, for example, switches, amplifiers and negative impedance converters (NICs) will give rise to additional thermal noise that must be accounted for.

In order to accurately analyze the noise performance of active metamaterials based on NICs, a circuit model similar to those presented previously [4, 5] is used. The noise performance, represented as the Power Spectral Density (PSD) and Noise Figure (NF), of broadband metamaterials will be studied using both analytical solutions and circuit simulations. All noise parameters of active metamaterials will be presented in comparison with their passive counterparts.

4.2 Effective Properties of Active Metamaterials

As proposed in last chapter, for electrically small loops ($|k|a < 1$, where $k = \omega\sqrt{\mu\varepsilon}$ is the wave number in the background medium and a is the loop radius), an equivalent circuit representation can be used to describe the loop parameters as shown in Fig. 3.1. Again, we define L_m , R_m and C_m as L_0 , R_0 and C_0 respectively. In addition, the two

branches of the loop's self-impedance Z_0 are also denoted with $Z_1 = R_0 + j\omega L_0$ and $Z_2 = R_C + 1/(j\omega C_0)$ for future use.

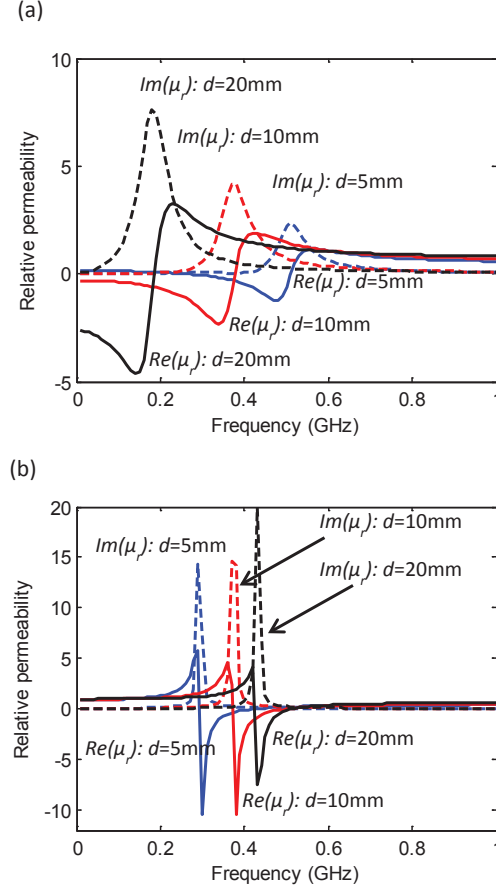


Figure 4.1: Extracted parameters of effective medium comprising infinite loaded loops corresponding to different spacing. (a) Non-Foster loading medium, (b) Passive loading medium.

In order to explore the effect of the mutual coupling between loops on the effective permeability of the periodic medium, an infinite loop array is applied here, with loop size 10 mm, wire radius 1 mm and coaxial loop spacing ranging from 5 to 20 mm. To guarantee the stability, the range of the load inductance can be obtained as $0 > L_L > -33nH$, while the stable load capacitance is given by $C_L < -1.54pF$ (see **Section 3.3.1**). In Fig. 4.1, the effective parameters of the non-Foster loading medium obtained from Eq. (3.5) are plotted corresponding to different spacing between adjacent loops. The non-Foster load is defined as a parallel negative RLC circuit with $R_L = -1000\Omega$, $L_L = -30nH$ and

$C_L = -2pF$ for all elements. For comparison, we also plot the results obtained from passively-loaded medium, constructed by replacing the non-Foster load of each loop with a positive capacitance of 4pF. It is noted that a non-dispersive negative-Re- μ (MNG) is achieved over a large frequency band for the non-Foster-loaded media, in contrast to the highly dispersive, and resonant passive metamaterials.

4.3 Analysis of Noise Performance in Active Broadband Metamaterials

4.3.1 0-Dimensional Case

In general, the noise contribution of metamaterials loaded with NICs can be considered to be the sum of both the loop resonator noise, and the NIC load noise. Fig. 4.2 shows the equivalent circuit of a single loop loaded with non-Foster circuits which are realized by terminating an NIC with a parallel positive RLC element Z_N . Since Linvill [6] designed and tested the first practical transistor-based NICs in 1953, the nonlinearity and instability have been recognised as key drawbacks of non-Foster circuit technology which has limited its application to microwave engineering areas. Recently, integrated circuit (IC) technology was proposed as a solution to reducing the parasitics of the implemented circuits [7, 8]. Moreover, the noise of the NIC itself can be almost eliminated by careful design. Therefore, two noise sources of a non-Foster loaded loop can be indicated. The first noise source S_1 is the Johnson noise arising from the load resistor R_N by assumption of an ideal noiseless NIC which is described by hybrid parameters (h-parameters). The second source S_2 , represents Johnson noise in the loop circuit R_w , along with the radiation resistance R_r , which in combination gives the resistance R_0 . Following the approach presented by Pierce[9], S_1 can be described by a mean square impressed current $\bar{I}_{nl}^2 = 4KTG_Ndf$ from an infinite-impedance source in shunt with the noise free conductance $G_N = 1/R_N$, while S_2 appears to be a noise voltage source

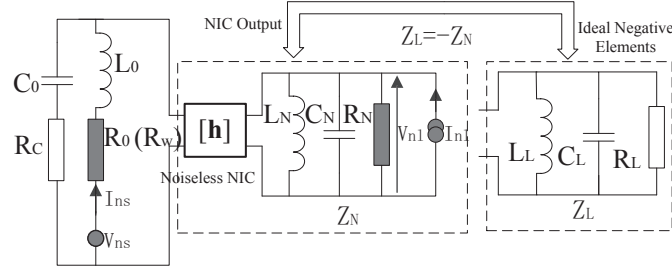


Figure 4.2: Equivalent circuit of a single loop with non-Foster load. The non-Foster circuits are obtained as the output of a noiseless NIC network terminated in a parallel positive RLC load Z_N . The impedance looking into the NIC output would ideally be $Z_L = -Z_N$. Shaded components indicate Johnson-Nyquist noise sources.

$\bar{V}_{ns}^2 = 4KTR_w df$ in series with a resistor R_w , where K is Boltzmann's constant and T is the absolute temperature (customarily taken to be 290K). Since R_w varies with frequency, a small frequency range df is taken for evaluation.

In order to analyze a linear noisy network containing more than one noise sources, Haus and Adler [10] have suggested that any noisy two-port is equivalent to an identical (but noiseless) two-port with two additional noise generators at its ports, and an impedance-matrix representation should be specified for a linear network [11]. However, due to the circuit topology, h-parameters are selected to represent the noisy network of a non-Foster loaded loop. Replacing S_1 and S_2 as terminals of a two-port network described by a voltage-current pair, a 2×2 array is thereby established

$$\begin{bmatrix} v_1 \\ i_2 \end{bmatrix} = \begin{bmatrix} h'_{11} & h'_{12} \\ h'_{21} & h'_{22} \end{bmatrix} \begin{bmatrix} i_1 \\ v_2 \end{bmatrix} \quad (4.1)$$

where

$$\begin{aligned} h'_{11} &= Z_N \parallel Z_{in2} \\ h'_{12} &= \frac{Z_2 \parallel Z_{in1} - h_{11}}{h_{12}(Z_1 + Z_2 \parallel Z_{in1})} \\ h'_{21} &= \frac{Z_N \parallel Z_{in2}(Z_0 - h_{22}Z_0Z_{in2})}{h_{21}Z_1Z_{in2}} \\ h'_{22} &= \frac{1}{Z_1 + Z_2 \parallel Z_{in1}}. \end{aligned}$$

For the purpose of clarity, some new parameters have been defined here. h_{ij} ($i, j = 1, 2$) is the corresponding element of the NIC h-parameters. Z_{in1} and Z_{in2} is the impedance looking into the NIC output and input from the loop circuit, respectively, where

$$\begin{aligned} Z_{in1} &= h_{11} - \frac{h_{12}h_{21}Z_N}{1 + h_{22}Z_N} \\ Z_{in2} &= \frac{Z_0 + h_{11}}{h_{11}h_{22} - h_{12}h_{21} + h_{22}Z_0}. \end{aligned}$$

For Z_L to be the negative of Z_N , it is required that $h_{11} = h_{22} = 0$ and $h_{12} = h_{21} = \pm 1$. When $h_{12} = h_{21} = -1$, the circuit is called a voltage inversion NIC (VNIC). On the other hand when $h_{12} = h_{21} = 1$, it is called a current inversion NIC (CNIC).

Now replacing S_1 and S_2 with the noise generators I_{nl} and V_{ns} , we can therefore obtain the noise matrix of the loop circuits whose elements are their self- and cross-averaged powers[2]

$$N = \begin{bmatrix} \langle h'_{11}h'^*_{11}\bar{I}_{nl}^2 \rangle & \langle h'_{12}h'^*_{12}\bar{V}_{ns}^2 \rangle \\ \langle h'_{21}h'^*_{21}\bar{I}_{nl}^2 \rangle & \langle h'_{22}h'^*_{22}\bar{V}_{ns}^2 \rangle \end{bmatrix}. \quad (4.2)$$

Furthermore, the resulting noise power spectral density (PSD) from the loop resonator and NIC load can be obtained, expressed as the mean square voltage variance per hertz (V^2/Hz)

$$\begin{aligned} S(V_{ns}) &= (h'_{12}h'^*_{12} + h'_{22}h'^*_{22}R_w^2)\bar{V}_{ns}^2/df \\ S(I_{nl}) &= (h'_{11}h'^*_{11} + h'_{21}h'^*_{21}R_w^2)\bar{I}_{nl}^2/df \end{aligned} \quad (4.3)$$

As discussed in Ref.[9], the noise contributions from the noise sources S_1 and S_2 should be uncorrelated since they arise from separate resistances. As a consequence, the total noise PSD results by summing the two contributions

$$\begin{aligned} S_{0_{active}} &= S(V_{ns}) + S(I_{nl}) = \\ 4KT &\left(\frac{R_w^3}{|Z_{s1}|^2} + \frac{R_w|Z_{p1}|^2}{|Z_{s1}|^2} + \frac{R_w^2|Z_p|^2}{|Z_1|^2|R_L|} + \frac{|Z_p|^2}{|R_L|} \right), \end{aligned} \quad (4.4)$$

where $Z_{p1} = Z_L \parallel Z_2$, $Z_{s1} = Z_1 + Z_{p1}$ and $Z_p = Z_0 \parallel Z_L$ are defined to simplify the expression.

From a practical point of view, it is quite useful to compare the noise between the active and passive metamaterials. Thus we also give the analytical description of the PSD

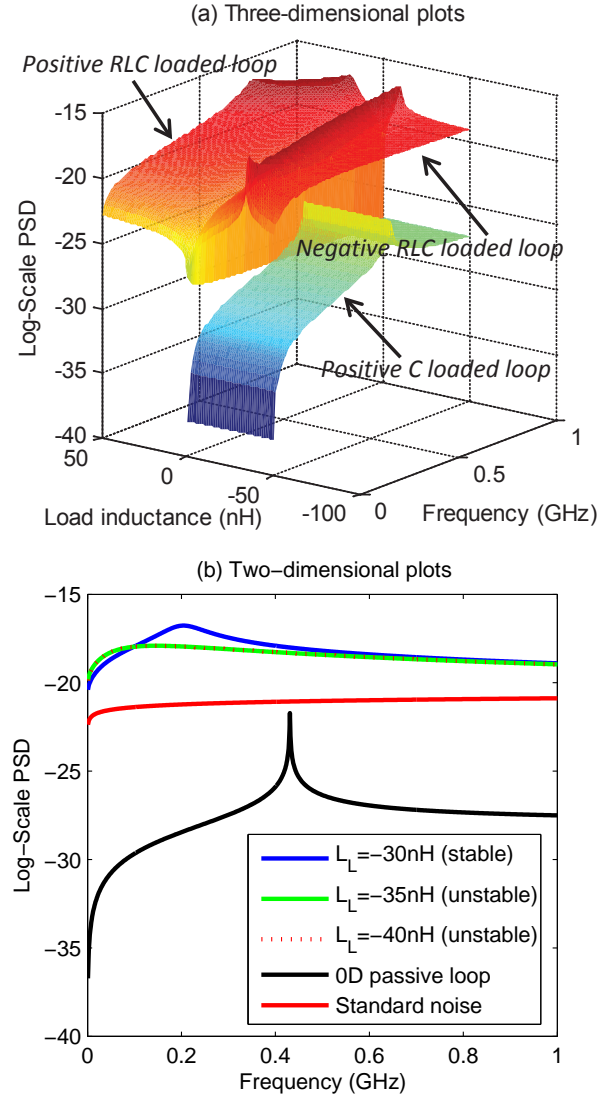


Figure 4.3: The power spectral density with the units V^2/Hz (log-scale) of noise from a single non-Foster loaded loop, as compared to a passively-loaded structure. (a) Three-dimensional plots of the PSD of the active loop with the NIC load inductance L_L changing from 0nH to -50nH while it varies from 0nH to +50nH for the positive RLC case, however having no impact on the positive C case. (b) Two-dimensional plots of the PSDs under different loading conditions, the negative inductance is varied from the stable to unstable cases.

of the noise for passive metamaterials based on the circuit model presented previously. For passive metamaterials, it is simple to see that the noise sources are due only to the Ohmic resistance of the loop since the non-Foster load was replaced by a single capacitance. In the same way, one can obtain the PSD of the noise of a single passive loaded loop

$$S_{0_{passive}} = S(V_{ns}) = 4KT \frac{R_w^3}{|Z_{s1}|^2}. \quad (4.5)$$

The analytical results of the noise PSD of a single loop under different loading conditions are plotted in Fig. 4.3. For the purpose of deeper investigation, both three-dimensional and two-dimensional results are given. The loop is made of copper with loop radius 10mm and wire radius 1mm, and we compare both passive and active loads. The active load consists of a parallel negative RLC circuit with load resistance and capacitance defined as $R_L = -1000\Omega$ and $C_L = -2pF$ respectively, while the load inductance is varied continuously from $L_L = 0nH$ to $L_L = -50nH$. Two passive loads are considered: the positive analog of active case, with $R_L = +1000\Omega$, $C_L = +2pF$ and inductance varying from $L_L = 0nH$ to $L_L = +50nH$; and a purely capacitive load $C_L = +4pF$, which resonates at the same frequency as the active case. As expected, in Fig. 4.3 (a) we see that the parallel RLC circuits exhibit power spectral densities of the same order (and we shall later see that their noise figures are identical). This would imply that active and passive metamaterials will show similar levels of noise, however the results of the purely capacitive load show that this is not the case, and in fact passive metamaterials will regularly have much lower noise levels. For the case of the active non-Foster load, the negative resistance is a requirement in order to maintain stability, and so this is an additional source of noise. For the passive case however, in order to obtain a resonance at the same location a lossless and purely reactive load is used, and so the total noise is far lower. So in order to obtain the higher bandwidth or gain of an active non-Foster metamaterial, additional noise sources are incorporated which will deteriorate the noise figure. The results are shown for specific stable and unstable cases in Fig. 4.3 (b) [4], in which the passive loop is a lossless capacitor. For comparison, the standard noise PSD

for a single loop is also given by the following expression

$$S_{0_{standard}} = 4KTR_w, \quad (4.6)$$

which appears to be lower than the active case, whereas higher than the passive case. Here we use a log-scale PSD with linear-scale frequency to give a more clarified demonstration. In agreement with the graphic description, the noise power of a non-Foster-loaded loop under stable conditions as well as the positive RLC loaded loop will reach a maximum at a specific frequency point which is given by the derivative of Eq. (4.4)

$$\omega_{0_{active}} \approx \sqrt{\frac{L_0 + L_L}{L_0 L_L (C_0 + C_L)}}. \quad (4.7)$$

However, it is interesting to note that for the active loop, the noise distribution of the unstable cases tend to remain unchanged when varying the load inductance as shown in Fig. 4.3 (b).

Moreover, the corresponding frequency point of a passive structure can be obtained as

$$\omega_{0_{passive}} \approx \frac{1}{\sqrt{L_0(C_0 + C_L)}}. \quad (4.8)$$

Furthermore, as expected, the active loaded loop exhibits higher noise levels than the passive case.

4.3.2 Noise in Infinitely Periodic Metamaterials

We begin our analysis of infinite periodic arrays of metamaterials by considering the 1D case of an infinitely long line of magnetically-coupled identical non-Foster loaded loops. As with the 0-dimensional case, an analysis of the noise effect produced by the metallic conductors as well as the active loads will be performed respectively. Assuming that the Ohmic resistance R_w is the unique noise source which provides a voltage supply to the

m th loop, the loop current related to the other currents is obtained in a similar manner to Ref[12]

$$Z_M I_n + j\omega \frac{Z_M}{Z_s} \sum_{m \neq n} M_{mn} I_m = V_n, \quad (4.9)$$

where $Z_s = Z_0 + Z_L$ is the series impedance of the loop, $Z_M = Z_{s1} Z_L / Z_{p1}$ is the impedance combination and V_n is the voltage drop in the Ohmic resistance R_w . Therefore, substituting the assumed wave solution $I_n = I_0 \exp(-n\gamma d)$ into Eq. (4.9), the characteristic equation of the noise wave due to the loop conductors can be obtained as

$$Z_s + 2j\omega \sum_{m=1}^{+\infty} M_m \cosh(m\gamma d) = 0, \quad (4.10)$$

where M_m is the mutual coupling between separate loops and d is the inner spacing.

In order to obtain the PSD due to the loop conductors for active metamaterials, as described in Ref.[13], we here assume an infinite 1D array with $-\infty < n < +\infty$, containing a single noise source V_{ns} arising from the Ohmic resistance R_w at the element zero. Since the noise wave will propagate from the source to either side, the wave solution can be rewritten as $I_n = I_0 \exp(-|n|\gamma d)$. Substituting into Eq. (4.9), one can easily obtain the corresponding noise current

$$I_0 = \frac{-V_{ns} Z_s}{2j\omega Z_M \sum_{m=1}^{+\infty} M_m \sinh(m\gamma d)}$$

Hence, the mean square value of the noise current at the n th element due to the noise source at element 0 can be obtained as

$$\bar{I}_n^2 = \frac{\bar{V}_{ns}^2 |Z_s|^2}{4\omega^2 |Z_M|^2 \left| \sum_{m=1}^{+\infty} M_m \sinh(m\gamma d) \right|^2} \exp(-2|n|\alpha d). \quad (4.11)$$

Since it is clear that there is uniformity in the noise effect from different sources due to the periodicity of the loop array, we can thereby obtain the mean square value of the

noise current at each element by summing up the overall noise response from all the elements, such that

$$\begin{aligned} \bar{I}_{oa}^2 &= \sum_{n=-\infty}^{+\infty} \bar{I}_n^2 \\ &= \frac{V_{ns}^2 |Z_s|^2}{4\omega^2 |Z_M|^2 \tanh(\alpha d) \left| \sum_{m=1}^{+\infty} M_m \sinh(m\gamma d) \right|^2}, \end{aligned} \quad (4.12)$$

where $V_{ns}^2 = 4KTR_w df$. Such that, for each element of an infinite 1D loop array, the PSD of the noise arising from the loop conductors can be derived as

$$S(V_{ns}) = \bar{I}_{oa}^2 \left(\frac{R_w^2 |Z_L|^2}{|Z_{p1}|^2} + |Z_L|^2 \right) / df. \quad (4.13)$$

We may now apply this result to the investigation of the noise effect from active loads in 1D infinite loop arrays. Assuming that the NIC load resistance R_N is the only noise source which provides a current supply to the m th loop, the voltage drop across the loop self-impedance Z_0 related to the other voltages is obtained as

$$\frac{V_n}{Z_p} + \frac{j\omega}{Z_s Z_p} \sum_{m \neq n} M_{mn} V_m = I_n, \quad (4.14)$$

where I_n is the current source produced by the active load. In a similar manner, the overall response in element zero excited by all the noise sources can be derived as

$$\bar{I}_{ob}^2 = \frac{\bar{I}_{nl}^2 |Z_s|^2 |Z_p|^2}{4\omega^2 |Z_0|^2 \tanh(\alpha d) \left| \sum_{m=1}^{+\infty} M_m \sinh(m\gamma d) \right|^2}, \quad (4.15)$$

where $\bar{I}_{nl}^2 = 4KTG_N df$. Hence, the PSD of the noise produced by the active loads can also be obtained

$$S(I_{nl}) = \bar{I}_{ob}^2 \left(\frac{R_w^2 |Z_0|^2}{|Z_1|^2} + |Z_0|^2 \right) / df. \quad (4.16)$$

Therefore, it is clear that the PSD of the noise for an infinite 1D non-Foster loading

medium is the sum of two contributions which can be written as

$$S_{1_{active}} = \theta_1(d) \left(\frac{R_w^3 |Z_s|^2 |Z_L|^2}{|Z_M|^2 |Z_{p1}|^2} + \frac{R_w |Z_s|^2 |Z_L|^2}{|Z_M|^2} + \frac{R_w^2 |Z_s|^2 |Z_p|^2}{|Z_1|^2 |R_L|} + \frac{|Z_s|^2 |Z_p|^2}{|R_L|} \right), \quad (4.17)$$

where

$$\theta_1(d) = \frac{KT}{\omega^2 \tanh(\alpha d) \left| \sum_{m=1}^{+\infty} M_m \sinh(m\gamma d) \right|^2}$$

shows the effects of the inner spacing of one-dimensional loop arrays.

Considering the noise effect of passive metamaterials, it is clear that the loop conductors are the only sources which contribute the noise power. Hence, the PSD of passive metamaterials for 1D infinite case is given by

$$S_{1_{passive}} = \theta_1(d) \frac{R_w^3 |Z_s|^2 |Z_L|^2}{|Z_M|^2 |Z_{p1}|^2}. \quad (4.18)$$

In Fig. 4.4, the PSDs for infinite lines of non-Foster-loaded loops, and passively-loaded loops are plotted. For each element, we apply the same definition of the physical size which has been proposed in the stability analysis. Furthermore, to investigate the effect of mutual coupling on the noise performance of 1D infinite effective medium, we increase the spacing between adjacent coaxial loops from 5mm to 20mm thus reasonably reducing the coupling coefficients. While the noise performance of the 1D infinite active medium differs from that of the passive medium, it is noted that in both cases, as the neighboring distance between adjacent loops tends to infinity the noise PSD tends to the 0D isolated loop case, as expected. Relating this result to the effective permeabilities of infinite periodic loop arrays, as shown in Fig. 4.1, it is clear to see that the noise power will increase as the negative permeability becomes more negative. However, noise

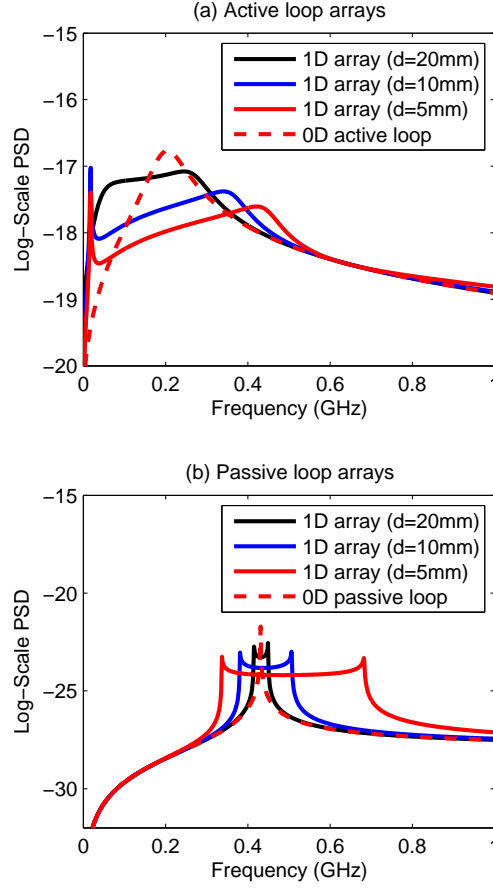


Figure 4.4: The PSD of the noise in one-dimensional infinitely-periodic loop arrays with different spacings. The spacing is varied from 5mm to 20mm. (a) The active media consist of periodic axial non-Foster loaded loops, where each load is defined as a parallel-RLC circuit with $R_L = -1000\Omega$, $L_L = -30nH$, and $C_L = -2pF$ (b) The passive media consist of loops where the loads are replaced by positive capacitances $C_L = 4pF$.

will decrease as the spacing is reduced which also results in the broadband mu-near-zero (MNZ) properties.

Subsequently the noise for the N -dimensional ($N > 1$) case will be investigated. Taking the mutual coupling from all directions into consideration, the dispersion equation can be rewritten as

$$Z_s + 2j\omega \sum_{i \in R^N} \sum_{m=1}^{+\infty} M_{m,i} \cosh(m\gamma_i d_i) = 0, \quad (4.19)$$

where the subscript i refers to the x , y or z directions in the Euclidean space R^N , d_i is the lattice spacing, $M_{m,i}$ is the mutual coupling between two loops a distance md_i from each other in the i direction, and $\gamma_i = \alpha_i + jk_i$ is the propagation constant in the i direction. Applying the method proposed in the 1D case, the N -dimensional PSD for a non-Foster loading medium can be obtained

$$S_{N_{active}} = \theta_N(d_i) \left(\frac{R_w^3 |Z_s|^2 |Z_L|^2}{|Z_M|^2 |Z_{p1}|^2} + \frac{R_w |Z_s|^2 |Z_L|^2}{|Z_M|^2} + \frac{R_w^2 |Z_s|^2 |Z_p|^2}{|Z_1|^2 |R_L|} + \frac{|Z_s|^2 |Z_p|^2}{|R_L|} \right), \quad (4.20)$$

where

$$\theta_N(d_i) = \frac{KT}{\omega^2 \prod_i \tanh(\alpha_i d_i) \left| \sum_i \sum_m M_{m,i} \sinh(m \gamma_i d_i) \right|^2}$$

is the spacing factor for the multi-dimensional case which imposes the effect of mutual coupling on the noise performance. Similarly, the PSD for a passively-loaded medium can be derived as

$$S_{N_{passive}} = \theta_N(d_i) \frac{R_w^3 |Z_s|^2 |Z_L|^2}{|Z_M|^2 |Z_{p1}|^2}. \quad (4.21)$$

We now apply the same physical definitions to the constituent elements of the 2D and 3D cases. The 2D loops are in the $x - y$ plane which results in a positive mutual inductance in the x (axial) direction and a negative one in the y (coplanar) direction, which consequently decreases the overall mutual inductance. Hence the 2D noise performance can be regarded as the 1D case with the coaxial coupling reduced. Furthermore, the 3D loops have an additional negative mutual inductance in the z direction, which will further reduce the coupling effect. Subsequent to verifying the analysis, the graphic description of the multi-dimensional noise PSDs are shown in Fig. 4.5. Irrespective of the dimensionality, a comparison of the active-load power distributions to their passive counterparts shows that the noise levels in active media are significantly (over 4dB) higher. Furthermore, it is interesting to note that in both cases, as the dimensionality is

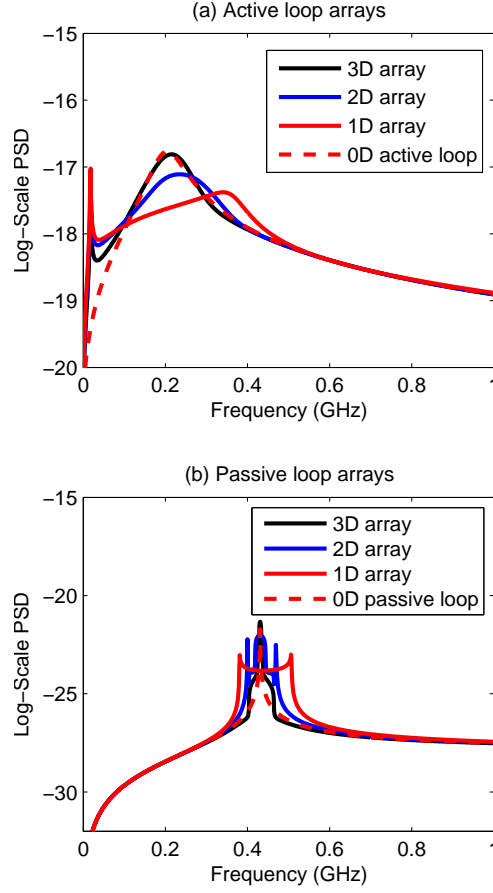


Figure 4.5: The PSD of the noise in multi-dimensional infinitely-periodic loop arrays, as compared to the single unit case. The 1D arrays consists of periodic coaxial loops with periodicity of 10mm in the x direction, while the 2D arrays have additional coplanar periodicity (25mm) in the y direction. The addition of coplanar periodicity (25mm) in the z direction results in the 3D array case. (a) Active medium consists of non-Foster loaded loops. (b) Passive medium consists of loops where the loads are replaced by positive capacitances.

increased from 1D to 3D, the spectra tend to that of the 0D case. This can be explained by considering the 0D case as a 1D case with the coaxial periodicity tending to infinity (i.e. mutual coupling is 0); for the 2D and 3D cases, the coplanar periodicity reduces mutual coupling (as described previously), and so their overall coupling coefficients will also decrease towards 0 (as with the 0D case).

4.3.3 Noise in Finite Metamaterials

Consider an N -element 1D structure consisting of identical loops loaded with NICs. As with the infinite case, the noise effect from conductors and active loads will be investigated separately. Assuming the voltage source arising from Johnson-Nyquist noise in R_w for each loop, we can derive a general relationship between the noise voltages and the corresponding currents through the loop circuit in the matrix form

$$\mathbf{V} = \bar{\mathbf{Z}}\mathbf{I}, \quad (4.22)$$

where

$$\mathbf{V} = \sum_i \mathbf{V}_i = (V_1, 0 \dots, 0) + (0, V_2, 0 \dots, 0) + \dots + (0, \dots, 0, V_N)$$

and

$$\mathbf{I} = (I_1, I_2 \dots I_N)$$

are N -dimensional vectors. Moreover, $\bar{V}_i^2 = 4KTR_w df$ ($i = 1 \dots N$) is the mean square value of the voltage source in loop i respectively. Here, however it should be stressed that the voltage vector is written as the sum of N vectors which refer to the noise sources coming from different loops since they are un-correlated. Based on Eq. (4.10), the impedance matrix $\bar{\mathbf{Z}}$ can be written as

$$\bar{Z}_{mn} = \begin{cases} Z_M & \text{if } m = n \\ \frac{j\omega M_{mn} Z_M}{Z_s} & \text{if } m \neq n \end{cases}. \quad (4.23)$$

It is now straightforward to derive the current vector by inverting the impedance matrix. Summing up all the responses from different voltage sources, we can then obtain the mean square current in element n

$$I_{na}^2 = \sum_i \left[(\bar{\mathbf{Z}}^{-1} \mathbf{V}_i)_n (\bar{\mathbf{Z}}^{-1} \mathbf{V}_i)_n^* \right], \quad (4.24)$$

where $(\bar{\mathbf{Z}}^{-1}\mathbf{V}_i)_n$ is the n th element of the current vector \mathbf{I} excited by the voltage vector \mathbf{V}_i . In other words, it represents the response at element n to a noise source at element i . As with the infinite case, the noise PSD in element n of a finite 1D loop array due to the loop conductors can thereby be obtained

$$S(V_{ns}) = I_{na}^2 \left(\frac{R_w^2 |Z_L|^2}{|Z_{p1}|^2} + |Z_L|^2 \right) / df. \quad (4.25)$$

The noise effects from the non-Foster loads will now be investigated. As discussed before, only the noise current due to the NIC load is taken into account, such that it will be the unique source for each loop. Similarly, the relationship between the current source arising from the load resistance and the voltage drop across the loop's self-impedance Z_0 can be expressed as

$$\mathbf{I} = \bar{\mathbf{Y}}\mathbf{V}, \quad (4.26)$$

where

$$\mathbf{I} = \sum_j \mathbf{I}_j = (I_1, 0, \dots, 0) + (0, I_2, 0, \dots, 0) + \dots + (0, \dots, 0, I_N)$$

is the sum of the noise current sources from different loops and

$$\mathbf{V} = (V_1, V_2, \dots, V_N)$$

is the corresponding voltage vector and $\bar{I}_j^2 = 4KTG_N df$ is the mean square value of the current source in the j th loop. From Eq. (4.14), the admittance matrix $\bar{\mathbf{Y}}$ is given by

$$\bar{\mathbf{Y}}_{mn} = \begin{cases} \frac{1}{Z_p} & \text{if } m = n \\ \frac{j\omega M_{mn}}{Z_s Z_p} & \text{if } m \neq n \end{cases}. \quad (4.27)$$

In a similar manner, the overall voltage response in element n of a finite 1D loop array

due to the NIC loads can be obtained as

$$V_{nb}^2 = \sum_j \left[(\bar{\mathbf{Y}}^{-1} \mathbf{I}_j)_n (\bar{\mathbf{Y}}^{-1} \mathbf{I}_j)_n^* \right], \quad (4.28)$$

where $(\bar{\mathbf{Y}}^{-1} \mathbf{I}_j)_n$ specifies the voltage response in element n for the current source in element j . Furthermore, the corresponding PSD produced by the NIC loads can be obtained as

$$S(I_{nl}) = V_{nb}^2 \left(\frac{R_w^2}{|Z_1|^2} + 1 \right) / df. \quad (4.29)$$

Finally, as with the infinite case, the noise PSD at the n th loop for a 1D finite NIC loaded structure is obtained by summing up both effects:

$$S_{1_{active}} = I_{na}^2 \left(\frac{R_w^2 |Z_L|^2}{|Z_{p1}|^2} + |Z_L|^2 \right) / df + V_{nb}^2 \left(\frac{R_w^2}{|Z_1|^2} + 1 \right) / df. \quad (4.30)$$

The analytical solution of the noise PSD for passively-loaded media consisting of a finite 1D loop array is given as,

$$S_{1_{passive}} = I_{na}^2 \frac{R_w^2 |Z_L|^2}{|Z_{p1}|^2} / df. \quad (4.31)$$

The constituent elements are defined by the same parameters as for the infinite case, with the coaxial lattice periodicity set at 10mm. By varying the number of the elements in the finite array, we shall give a graphic description of the noise PSD in a 1D finite loop array. As shown in Fig. 4.6, the PSDs at central element are plotted under both active and passive loading conditions. Furthermore, the 0D and 1D infinite cases are also plotted for comparison. Again, the active media exhibit higher noise levels. And as expected, as the number of elements increases, the spectral distribution tends from the 0D case to the 1D infinite case. The noise PSDs for the 2D and 3D finite structures can be obtained in a similar manner by modifying the impedance (admittance) matrix to include the additional elements, and element-to-element coupling parameters.

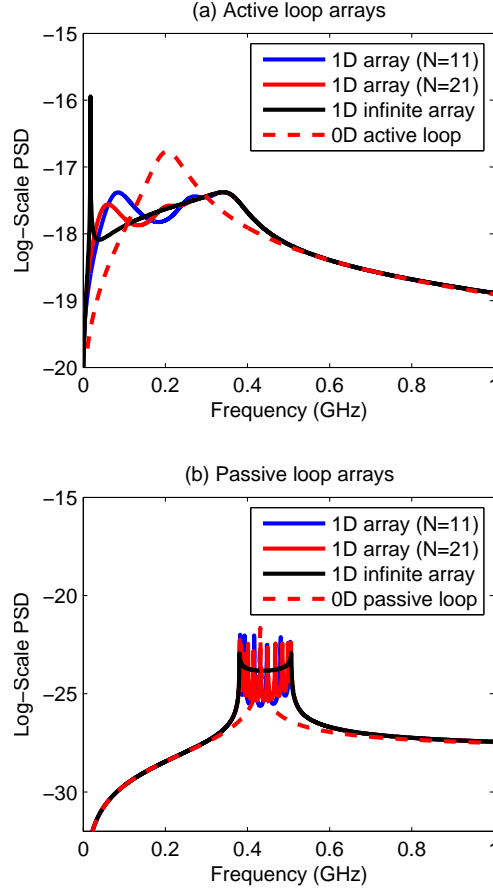


Figure 4.6: The PSD of the noise at the central element of a finite 1D loop array, as compared to the single unit and the infinite cases. The lattice spacing is 10mm, and the number of elements varies from 11 to 21. (a) Active medium consists of non-Foster loaded loops. (b) Passive medium consists of loops where the loads are replaced by positive capacitances.

4.3.4 Noise Figure for Metamaterials

We will now investigate the noise figures of active metamaterials with non-Foster loads. The noise figure is one of the key figures of merit of any active system, and is crucial for quantifying any possible improvements in performance as compared to passive structures. In order to analyze the noise figure, the complete circuit model of a single loop is shown in Fig. 4.7, as composed using a two-port network connected to a voltage source V_s , with output impedance R_{source} at port 1 and a load R_{load} at port 2.

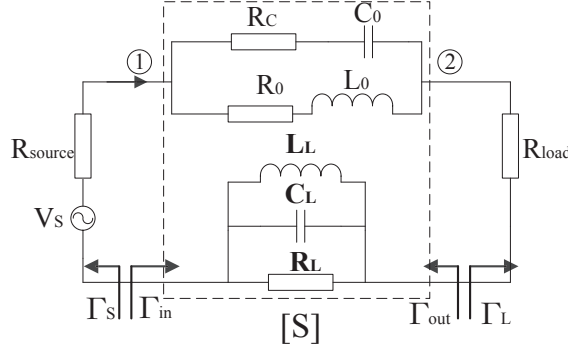


Figure 4.7: A system using a single active loop to connect a source R_{source} to a load R_{load} . As discussed before, the active load is a non-Foster element Z_L generated from the NIC, and equivalent to a parallel negative RLC circuit ($Z_L = R_L || L_L || C_L$).

The available signal power at the input can be obtained as $S_i = V_s^2 / (4R_{source})$, while the available noise power over a specified bandwidth B is given by $N_i = KTB$ [14]. It is well known that the output noise power is a sum of the transformed input noise and the internally generated noise [15], such that $N_0 = GK T df + N_{added}$, where G is the network gain, df is the differential frequency interval, and N_{added} is the output noise power generated internally by the network (referenced at port 2). The output signal power is given by $S_0 = GS_i$. Based on the analysis of the network,

$$G = \frac{4R_{source}^2}{|Z_{s2}|^2}, \quad (4.32)$$

$$\begin{aligned} N_{added} &= (\bar{I}_{n1}^2 + \bar{I}_{n2}^2) R_{load} \\ &= 4KTdf \left(\frac{R_w |Z_{p3}|^2}{|Z_{s3}|^2 |Z_{L2}|^2} + \frac{|Z_{p2}|^2}{|R_L| |Z_{02}|^2} \right) R_{load}, \end{aligned}$$

where $Z_{s2} = Z_s + Z_{source} + Z_{load}$ is the series impedance of the overall circuit, and \bar{I}_{n1}^2 and \bar{I}_{n2}^2 are the mean square values of the noise currents through the loop due to the loop conductor and the NIC load. In addition, for the purpose of convenience, we also define some new parameters as follows: $Z_{02} = Z_0 + R_{source} + R_{load}$, $Z_{p2} = Z_L || Z_{02}$, $Z_{L2} = Z_L + R_{source} + R_{load}$, $Z_{p3} = Z_{L2} || Z_2$, and $Z_{s3} = Z_1 + Z_{p3}$. Therefore, the noise

figure of the system consisting of a single non-Foster loaded loop is given by

$$\begin{aligned} F_{0_{active}} &= \frac{S_i/N_i}{S_0/N_0} = 1 + \frac{N_{added}}{GKTdf} \\ &= 1 + \frac{|Z_{s2}|^2}{R_{source}} \left(\frac{R_w|Z_{p3}|^2}{|Z_{s3}|^2|Z_{L2}|^2} + \frac{|Z_{p2}|^2}{|R_L||Z_{02}|^2} \right). \end{aligned} \quad (4.33)$$

Replacing the NIC load with the positive capacitance as before, one may obtain the noise figure for the limiting passive case:

$$F_{0_{passive}} = 1 + \frac{|Z_{s2}|^2}{R_{source}} \frac{R_w|Z_{p3}|^3}{|Z_{s3}|^2|Z_{L2}|^2}. \quad (4.34)$$

In Fig. 4.8 (a) we plot the noise figures for single-loop active and passive systems. The active system consists of a non-Foster parallel RLC circuit, in which the negative inductance is varied. As before, two passive cases are compared: a positive parallel RLC, and a lossless capacitive load. Unsurprisingly, as discussed earlier the noise figure of the lossless passively-loaded system can almost be neglected in comparison to the active structure, while the parallel RLC noise figures are identical, whether the load is positive or negative. It is also interesting to note that the noise figure for the actively-loaded loop system correlates to the gain of the network. This is demonstrated in Fig. 4.8 (b), where the inverse relationship between the noise figure and gain is clear to see. However, it should be stressed that they are not exactly opposite to each other, since the noise figure is also related to the additional noise power from the network. Further to the multi-element case, the noise can be considered as a cascaded system, in which the gain of each element will affect the noise figures of subsequent elements. Additionally it should be pointed out that the extrema of the gain and the noise figures both occur at the same frequency point which can be calculated by solving for the derivative of Eq. (4.33).

$$\omega_{0_{active}} = \omega \Big|_{\partial F_{0_{active}}/\partial \omega = 0} \approx \frac{1}{\sqrt{L_L C_L}}. \quad (4.35)$$

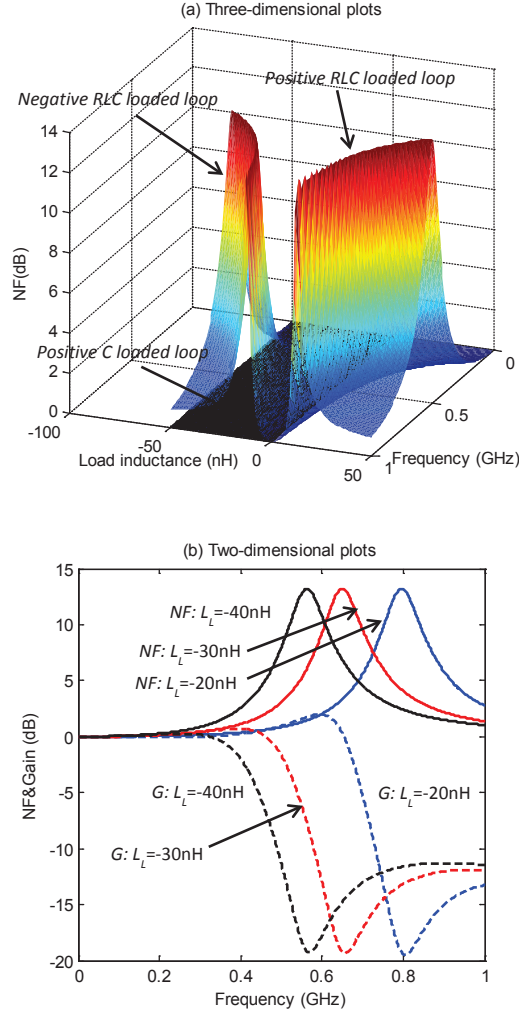


Figure 4.8: (a) The noise figure of the system consisting of a single non-Foster's loaded loop, as compared to the passive case. As proposed before, we take the same definitions for the loop and the loads, but vary the load inductance from $L_L = -50\text{nH}$ to $L_L = 0\text{nH}$. (b) The contrast between the noise figure and the gain of the network for the actively-loaded system with discrete load inductances $L_L = -20\text{nH}$, $L_L = -30\text{nH}$ and $L_L = -40\text{nH}$.

In agreement with the analytical solution, one may observe that the frequency point corresponding to the maximum noise figure of the non-Foster's loaded system will increase as the negative load inductance L_L increases towards zero. However, the peak value remains almost fixed at around 13dB.

We begin our analysis by considering a system of N -element non-Foster loaded loops, as shown in Fig. 4.9, where the source loop and the load loop are located at either end.

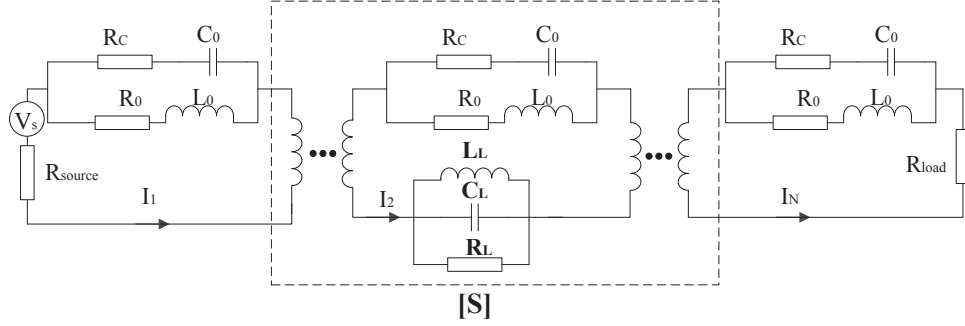


Figure 4.9: A system using a 1D active loop array to connect a source and a load.

In order to obtain the corresponding noise figure, the most straightforward way is to develop the impedance (admittance) matrix of the equivalent circuit model and make independent analysis of the noise arising from different sources of the loops. Assuming noise free conditions for all elements, the relationship between the voltages and the related currents through the loop may be derived in matrix form as

$$\mathbf{V}_0 = \bar{\mathbf{Z}}_0 \mathbf{I}_0, \quad (4.36)$$

where $\mathbf{V}_0 = (V_s, 0 \dots, 0)$ and $\mathbf{I}_0 = (I_1, I_1 \dots I_N)$ are N -dimensional vectors, and $\bar{\mathbf{Z}}_0$ is an impedance matrix in which the diagonal terms are the self-impedances of the loops, and the off-diagonal terms are given by the mutual impedances. The output signal power is thereby obtained

$$S_o = \bar{I}_N^2 R_{load}. \quad (4.37)$$

Similarly, replacing the voltage vector with $\mathbf{V}_s = (V_{s1}, 0 \dots, 0)$ where $V_{s1}^2 = 4KT R_{source} df$ is the mean square value of the voltage arising from the source resistor, the noise current vector can then be derived as $\mathbf{I}_s = (I_{s1}, I_{s2} \dots I_{sN})$. Thus, the transformed input noise due to the source resistor is obtained

$$N_{o1} = \bar{I}_{sN}^2 R_{load}. \quad (4.38)$$

As with the single unit case, the output noise power of the 1D system should also

include the additional noise generated by the transmission network which covers the noise effects from the loop conductors as well as the NIC loads respectively. The output noise produced by the loop conductors can be obtained by summing up all the contributions from each element. For the noise source at element n ($n = 1 \dots N$), an N -dimensional current vector $\mathbf{I}_1^{(n)} = (i_1, i_2 \dots i_N)$ can be solved by applying the matrix transformation

$$\mathbf{I}_1^{(n)} = \bar{\mathbf{Z}}_1^{-1} \mathbf{V}_1^{(n)}, \quad (4.39)$$

where $\mathbf{V}_1^{(n)} = (0, \dots, 0, v_n, 0, \dots, 0)$ is the corresponding voltage vector, $\bar{\mathbf{Z}}_1$ is the impedance matrix which can be obtained from Eq. (4.10), and $\bar{v}_n^2 = 4KTR_w df$ is the mean square impressed voltage arising from the ohmic resistance. Since the noise voltage sources of different loops are un-correlated, then the output noise power produced by the loop conductors can be obtained by summing up the response for all the voltage vectors

$$N_{o2} = \sum_{n=1}^N (i_N^2 R_{load}). \quad (4.40)$$

In a similar manner, the relationship between the voltages across the loop and the related noise currents produced by the NIC loads can be written as

$$\mathbf{V}_2^{(n)} = \bar{\mathbf{Y}}_2^{-1} \mathbf{I}_2^{(n)}, \quad (4.41)$$

where $\mathbf{V}_2^{(n)} = (v'_1, v'_2 \dots v'_N)$ is the N -dimensional voltage vector and $\mathbf{I}_2^{(n)} = (0, \dots, 0, i'_n, 0, \dots, 0)$ is the corresponding current vector, which takes into consideration only the noise current source arising from the load resistance R_L at element n . In the same way, the admittance matrix $\bar{\mathbf{Y}}_2$ can be derived from Eq. (4.14). In addition, one should bear in mind that the mean square value of the noise currents at the source and load loops differ from the

other loops. They are given as:

$$i_n'^{-2} = \begin{cases} 0 & \text{if } n = 1 \\ \frac{4KTdf}{|R_L|} & \text{if } 1 < n < N \\ 0 & \text{if } n = N \end{cases}$$

Following the previous analysis, one may directly derive the output noise power produced by the NIC loads

$$N_{o3} = \sum_{n=1}^N \left(\frac{v_N'^{-2}}{|Z_0 + R_{load}|^2} R_{load} \right). \quad (4.42)$$

Thus, the overall output noise power is given by $N_o = N_{o1} + N_{o2} + N_{o3}$. Now the noise figure for the 1D case can be obtained

$$\begin{aligned} F_{1_{active}} &= \frac{S_i/N_i}{S_0/N_0} = \frac{V_s^2}{4KTR_{source}df} \\ &\times \frac{I_{sN}^2 + \sum_{n=1}^N \left[(i_N^2 + v_N'^{-2}/|Z_0 + R_{load}|^2) \right]}{I_N^2}. \end{aligned} \quad (4.43)$$

In Fig. 4.10 the analytical results are plotted as the lattice periodicity, or the NIC load inductance, are varied. For comparison, we also plot the noise figure of a single non-Foster loaded loop system. Clearly the noise figure will move upward with the increasing unit-cell length as shown in Fig. 4.10 (a). However, as with the 0D case, the noise figure is related to the inverse of the gain, and the frequency of maximum noise figure is found at:

$$\omega_{1_{active}} = \omega \Big|_{\partial F_{1_{active}}/\partial \omega = 0} \approx \frac{1}{\sqrt{L_L C_L}}. \quad (4.44)$$

Comparing with the distribution of the effective parameters[4], it is not difficult to further to the relationship between the permeability and the noise figure in respect to the load

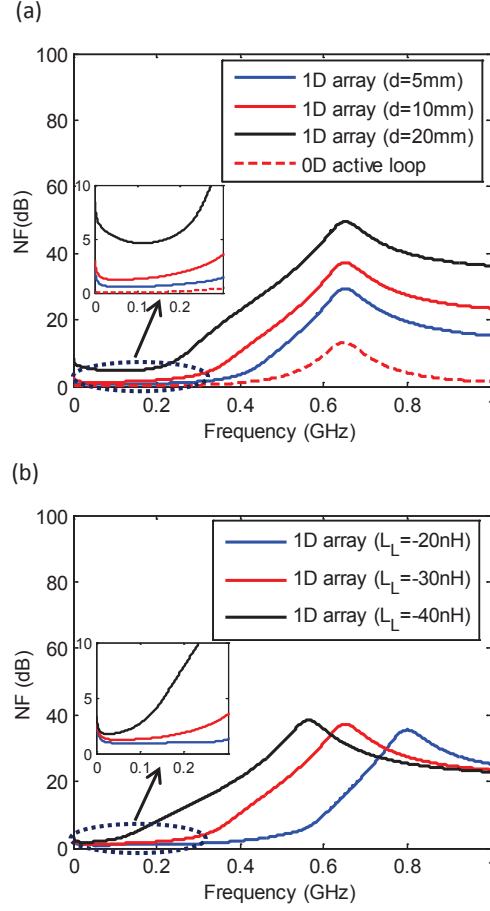


Figure 4.10: The noise figure of one-dimensional non-Foster loaded loop arrays. (a) and (b) correspond, respectively, to different distances between neighboring loops and different load inductances.

inductance as shown in Fig. 4.10 (b). In the case of a system made up of 1D non-Foster loading medium, an increased load inductance will result in a flatter but less negative MNG or MNZ medium, while the noise figure will decrease and the stability will also be improved. In contrast, the noise performance as well as the stability of the system will deteriorate in order to achieve a more negative $\text{Re-}\mu$ for the 1D active medium. Finally, it is possible to extend our analysis to 2D and 3D cases following the proposed approach.

4.4 Simulation of Noise Performance in Active Broadband Metamaterials

Since the noise of active metamaterials for 0-dimension case is the basis for subsequent noise analysis as presented before, here we will validate it again using Agilent ADS software [16], and compare the simulation results to the analytical solutions.

To study the noise of non-Foster loaded loop, it is essential to find out all the noise sources. Hence we can indicate the loop's Omic resistance R_w and NIC load resistance R_N as the two noise sources by assumption of a noiseless NIC based on the equivalent circuit. Which should be emphasized here is that the principle of non-Foster's negative elements is different with other negative resistance devices such as negative resistance amplifiers. The non-Foster's negative resistance is the output of a transformer (called NIC) terminating in positive resistance while the negative resistance are generated internally for the amplifier. Hence, the noise effect of non-Foster's negative resistance should comprise the noise contributions from the positive resistance and the NIC itself. However, recently progress on the NIC design based on integrated circuit (IC) technology can reduce the parasitics which makes the noise cancelation possible. Thus we take the noise from the positive resistance as the only noise source of the active load. To verify the circuit model, a widely used circuit design software ADS [16] is employed to construct the equivalent circuit of a single NIC loaded loop as shown in Fig. 4.11.

Here, a two-port hybrid is applied to represent the NIC circuit by its h-parameters h_{ij} ($i, j = 1, 2$). For comparison, the schematic of the circuit model of a single loop loaded with ideal negative elements are also displayed. When the h-parameters are selected as $h_{11} = h_{22} = 0$ and $h_{12} = h_{21} = -1$ which is the expression of voltage controlled NIC (VNIV), we can observe that the total impedance of NIC-loaded loop circuit is equal to the ideal negative elements loaded structure from Fig. 4.12, thus verifies our circuit model. Moreover, it should be noted that the resistances R_0 and R_c we chose here for the loop circuit are constants for the purpose of simulation, since ADS is unable to define

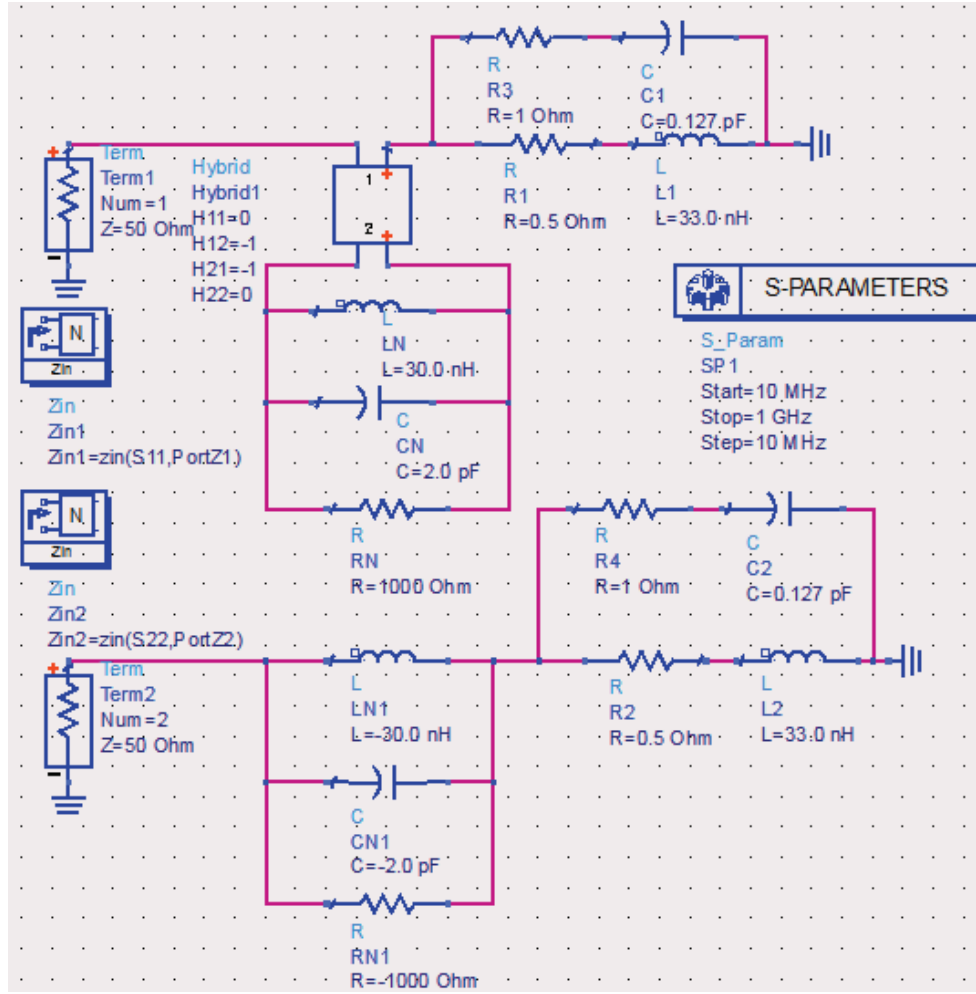


Figure 4.11: Schematic of the circuit model of a NIC-loaded loop, as compared to the loop circuit loaded with ideal negative elements. The NIC is described by its h-parameters.

lumped elements with frequency dependent variables.

Based on the equivalent circuit model, I followed the approach proposed by Haus and Adler [10] which is suitable for the analysis of a noisy circuit containing more than one noise sources. Hence, the NIC loaded loop circuit can be modeled as a noiseless two-port with the two noise sources at its ports. H-parameters are used to represent the network instead of impedance or admittance matrix due to the topology of the circuit. Subsequent to the noise analysis, a noise matrix is established whose elements are the self- and cross-average power of the different noise sources as proposed by Gabriel [2].

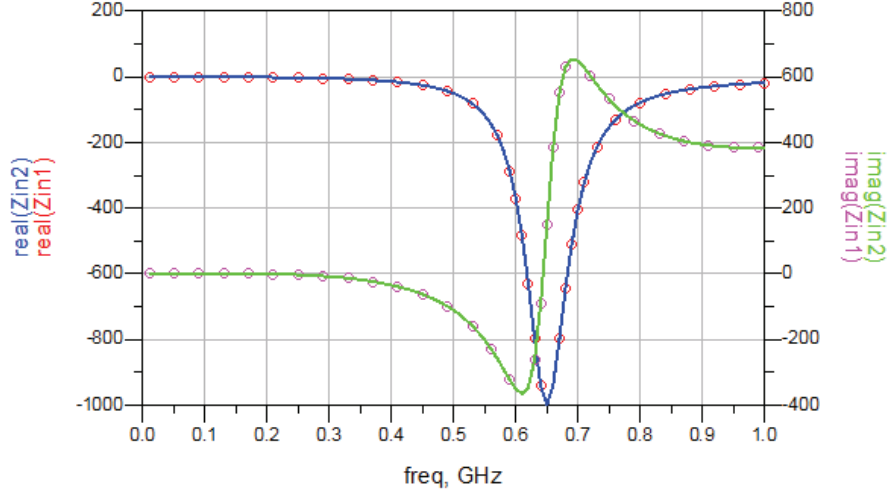


Figure 4.12: The real part and imaginary parts of the input impedance of the NIC-loaded loop circuit (circle symbols line) and ideal negative elements loaded circuit (solid line), respectively.

As a consequence, the noise power spectral density can be easily derived. Again, to verify the solution we proposed in this paper for the noise analysis of single non-Foster loaded loop, we will give the ADS simulation results for comparison. To simplify the calculation, the noisy resistance R_w is replaced by R_0 ignoring the radiation resistance R_r . Hence, R_0 and R_N are the two noise sources of the loop circuit. Since the noise power spectral density cannot be read directly from ADS, the node noise voltage will be analyzed instead. As shown in Fig. 4.13, we appoint node V_{out} as the noise voltage to be investigated. Since the two noise sources are uncorrelated as stated in the paper, the total noise power is the summation of both contributions. Similarly, we can derive the noise voltage arising from different sources separately. Assuming the Omic resistance R_0 is the only noise source, the mean square noise voltage at node V_{out} can be obtained

$$\overline{V_{out}(R_0)^2} = \overline{V_{ns}^2} \left| \frac{Z_2 \parallel Z_{in1}}{Z_2 \parallel Z_{in1} + Z_1} \right|. \quad (4.45)$$

Then taking the NIC load resistance R_N as the only noise generator, we may have

$$\overline{V_{out}(R_N)^2} = \overline{I_{nl}^2} \left| \frac{h_{11}(1 - h_{22}Z_{in2})Z_N \parallel Z_{in2}}{h_{21}Z_{in2}} + h_{12}(Z_N \parallel Z_{in2}) \right|, \quad (4.46)$$

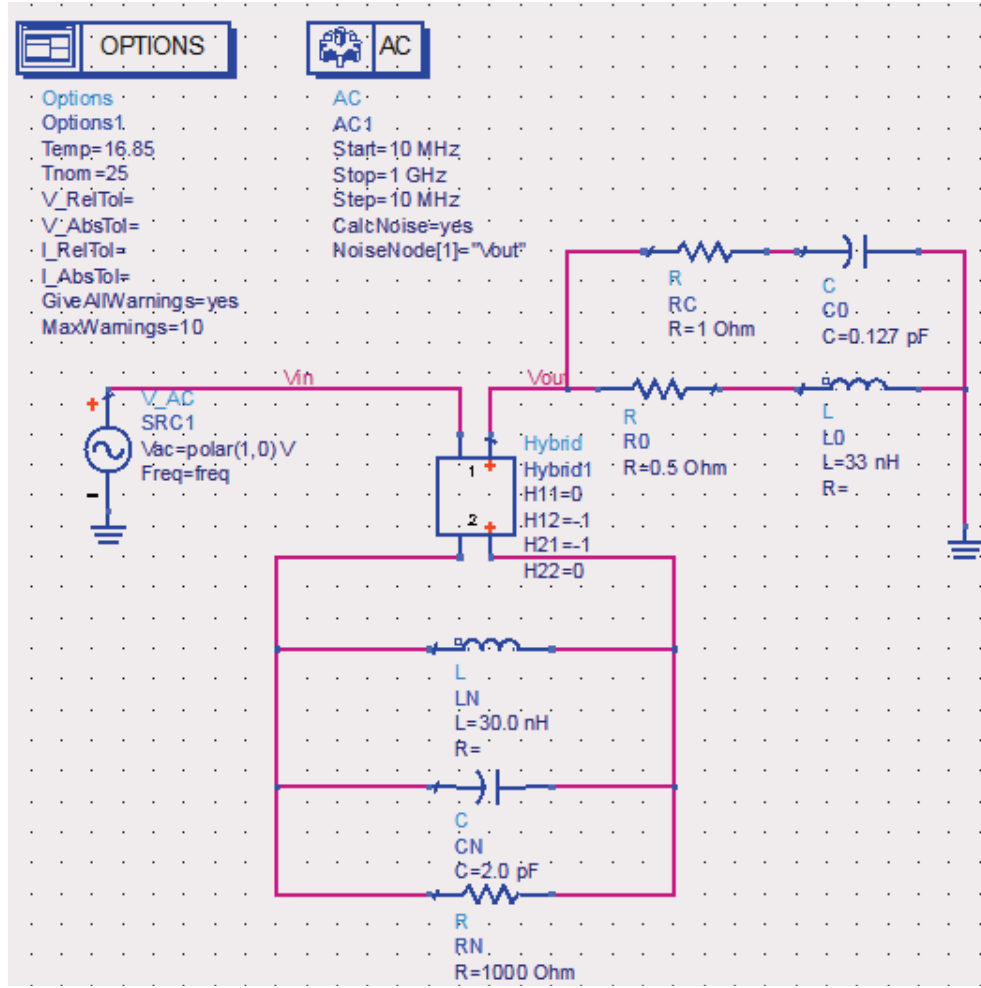


Figure 4.13: Schematic of the noisy network where R_0 and R_N are the two noise sources.

where all of the variables has been defined in the paper. Thus the node noise voltage results by summing up the both contributions like the power spectral density (PSD)

$$\overline{V_{out}^2} = \overline{V_{out}(R_0)^2} + \overline{V_{out}(R_N)^2}. \quad (4.47)$$

As shown in Fig. 4.14, the simulation and analytical results of the node noise voltage V_{out} at different frequencies are displayed which obviously are in agreement with each other. Furthermore, parts of the node noise voltages at discrete frequencies simulated by ADS are displayed in Fig. 4.15, not only verifies the node voltage at 70 MHz as shown in Fig. 4.14, but also demonstrates that the total noise effect is the summation of the two

noise contributions. Thus our methodology proposed in the report on the noise analysis of 0-dimensional case is verified.

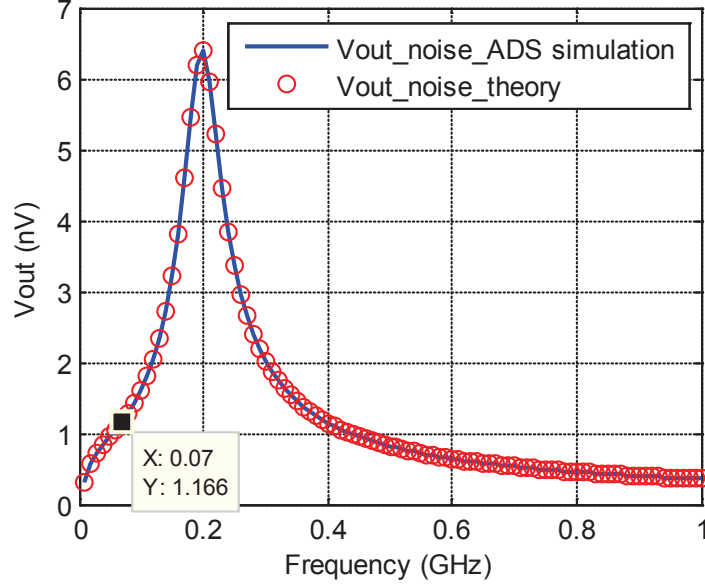


Figure 4.14: The root mean square (RMS) node noise voltage V_{out} at different frequencies. The solid blue line represents the ADS simulation results while the red circle symbols line represents the theoretical results.

4.5 Conclusions

The noise performance of active broadband metamaterials consisting of loops with NIC loads are analyzed based on the circuit model established in this chapter. Starting from a zero-dimensional case, we use the power spectrum density (PSD) to demonstrate the noise effect of active metamaterials. As opposed to their passive counterparts, the noise source arising from the active load should be taken into account for an active medium. Summing up the effects of noise from both the NICs and conductive materials, we have provided the analytical solutions for one, two and three dimensional cases, and for finite and infinite domains. Our results correlate with the expectation that noise figure will remain unchanged whether a resistive load is positive or negative. However

index	name	vnc
freq=10.00 MHz		
0	_total	319.2 pV
1	R0	317.8 pV
2	RN	30.31 pV
3	SRC1	0.0000 V
freq=20.00 MHz		
0	_total	560.5 pV
1	R0	550.9 pV
2	RN	102.9 pV
3	SRC1	0.0000 V
freq=30.00 MHz		
0	_total	725.7 pV
1	R0	699.0 pV
2	RN	195.1 pV
3	SRC1	0.0000 V
freq=40.00 MHz		
0	_total	848.1 pV
1	R0	795.0 pV
2	RN	295.4 pV
3	SRC1	0.0000 V
freq=50.00 MHz		
0	_total	953.4 pV
1	R0	864.8 pV
2	RN	401.4 pV
3	SRC1	0.0000 V
freq=60.00 MHz		
0	_total	1.056 nV
1	R0	923.0 pV
2	RN	514.0 pV
3	SRC1	0.0000 V
freq=70.00 MHz		
0	_total	1.166 nV
1	R0	978.3 pV
2	RN	635.4 pV
3	SRC1	0.0000 V

Figure 4.15: Parts of the list of the node noise voltage V_{out} where the first column indicates the frequency, the second column shows the noise contributions are from R_0 and R_N and the third column gives the voltage value corresponding to the noise sources.

for a passive metamaterial resonance is typically obtained using lossless reactive loads (in this case loading the loop with a capacitor), while stability requirements necessitate a loss component for the non-Foster active load. Therefore it was shown that in order to obtain the same resonant frequency, the noise level for active metamaterials is significantly higher than for practical passive structures. However, we should note that it is also possible to obtain a wide frequency band and gain with the active load, and so there exists a tradeoff between these parameters and the noise figure of the structures. We can

now conclude that, active metamaterials with NICs demonstrate much higher noise levels in comparison with passive metamaterials consisting of resonant structures. However, active metamaterials possess extraordinary material properties which are impossible to implement with passive media, over such broad frequency ranges. The impact of active broadband metamaterials to the design of innovative devices for applications such as the perfect lens, electrically small antennas and thin absorbers should be rigorously quantified in the context of breaking fundamental laws of physics.

References

- [1] J. B. Johnson, “Thermal agitation of electricity in conductors,” *Phys. Rev.*, vol. 32, pp. 97–109, 1928.
- [2] G. Vasilescu, *Electronic Noise and interfering Signals: Principles and Applications*. Springer-Verlag Berlin Heidelberg, 2005.
- [3] H. Nyquist, “Thermal agitation of electric charge in conductors,” *Phys. Rev.*, vol. 32, pp. 110–113, 1928.
- [4] K. Z. Rajab, Y. Hao, D. Bao, C. G. Parini, C. Vazquez, J. Philippakis, and M. Philippakis, “Stability of active magnetoinductive metamaterials,” *J. Appl. Phys.*, vol. 108, p. 054904, 2010.
- [5] K. Z. Rajab, Y. Fan, and Y. Hao, “Characterization of active metamaterials based on negative impedance converters,” *J. Opt.*, vol. 14, p. 114004, 2012.
- [6] J. G. Linvill, “Transistor negative impedance converters,” *Proc. IRE*, vol. 41, pp. 725–729, 1953.
- [7] E. Yuce, “Negative impedance converter with reduced nonideal gain and parasitic impedance effects,” *IEEE Trans. Circuits and Systems-I: Regular papers*, vol. 55, pp. 276–283, 2008.
- [8] C. R. White, J. W. May, and J. S. Colburn, “A variable negative-inductance integrated circuit at uhf frequencies,” *IEEE Microw. and Wireless Compon. Lett.*, vol. 22, pp. 35–37, 2012.

- [9] J. R. Pierce, “Physical sources of noises,” *Proc. IRE.*, vol. 44, p. 601, 1956.
- [10] H. A. Haus and R. B. Adler, *Circuit Theory of Linear Noisy Networks*. Technology Press, Mass. Inst. Tech and John Wiley and Sons, Inc., N. Y., 1959.
- [11] K. Kurokawa, “Power waves and the scattering matrix,” *IEEE Trans. Microw. Theory Tech.*, vol. 13, pp. 194–202, 1965.
- [12] E. Shamonina, V. A. Kalinin, K. H. Ringhofer, and L. Solymar, “Magnetoinductive waves in one, two, and three dimensions,” *J. Appl. Phys.*, vol. 92, p. 6252, 2002.
- [13] R. R. A. Syms and L. Solymar, “Noise in metamaterials,” *J. Appl. Phys.*, vol. 109, p. 124909, 2011.
- [14] H. T. Friis, “Noise figure of radio receivers,” *Proc. IRE*, vol. 32, pp. 419–C422, 1944.
- [15] D. M. Pozar, *Microwave Engineering*, 4th ed. New York: Wiley, 2011.
- [16] Advanced Design System 2013, Agilent Technologies, URL: <http://www.agilent.com/>.

Chapter 5

Characterization of Active High Impedance Surfaces with Non-Foster Loads

In this chapter, a detailed investigation on the characterization of active high impedance surface (HIS) with non-Foster loads is presented. Comparing with conventional HIS, it is shown that this actively-loaded metamaterial surface structure incorporating negative impedance components may overcome the inherent physical limitations of passive HIS, thus exhibits broadband and other outstanding properties. However, similar to the active magnetic metamaterials as discussed in Chapter 3, the active HIS performance may be restricted due to the stability issue which needs to be explored. Therefore, based on the accurate circuit model of the HIS structure, the way to achieve a broadband active HIS whilst maintaining the stability will be analytically provided, further to give the design sample verified by full-wave simulation results.

5.1 Background

High impedance surface (HIS) or artificial magnetic conductor (AMC) is a type of meta-material based on planar periodic arrays of metal strips or patches, that exhibits the performance of magnetic walls over a limited bandwidth [1–5]. Such special texture may be applied to artificial dielectrics [6], antenna radomes [7] and radiation enhancement [8] due to the properties of their in-phase reflection and suppression of surface waves. Other typical applications include frequency selective surfaces [9], phase shifters [10, 11], TEM wave guides [12], planar reflect-arrays [13] and absorbers [14–17].

For a normal conductive surface (as the ground) based antenna, we should note that in order to cancel the destructive interference effect in the antenna radiation, one-quarter wavelength space between the radiating element and the ground plane is required, resulting in a large thickness structure. However, by incorporating the special texture over the upper surface, also referred to as an HIS, the structure thickness may be reduced since the electromagnetic surface properties are altered. This can be explained by investigating the plane-wave reflection from a boundary characterized by a scalar surface impedance Z_s . For the normal incident of plane waves, the reflection coefficient for the electric field is [18]

$$\Gamma = \frac{Z_s - \eta}{Z_s + \eta} \quad (5.1)$$

where η is the wave impedance in free space ($\eta = \sqrt{\mu_0/\epsilon_0} = 377\Omega$). As we know, the electrical wall realized from good conductors corresponds to $Z_s = 0$, which gives $\Gamma = -1$, that is zero tangential electric field on the interface. However, in the case of magnetic wall which can reflect electromagnetic waves without any change in the electric field phase, we should have $\Gamma = 1$, which corresponds to zero tangential magnetic field. It is straightforward that this happens when $Z_s \rightarrow \infty$, which is referred to as *artificial high-impedance surfaces* [1].

Assuming a dielectric layer of thickness d covered with a metal ground plane shown in Fig. 5.1 (a), the input impedance seen at the upper surface by normally incident plane

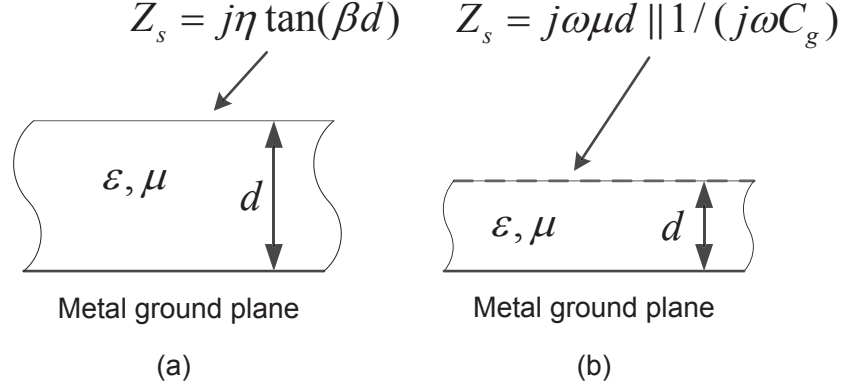


Figure 5.1: Realized of a magnetic wall as a dielectric layer covered with a metal ground plane and as an artificial high-impedance surfaces. (a) Without HIS texture at the upper surface and (b) With HIS texture at the upper surface. Clearly, the thickness is reduced by using textured surface. [19]

wave is [19]

$$Z_s = j\eta \tan(\beta d) = j\sqrt{\frac{\mu}{\epsilon}} \tan\left(\frac{2\pi}{\lambda} d\right). \quad (5.2)$$

which leads to an infinite surface impedance at $d = \lambda/4$, achieving a magnetic wall. However, it is evident that a quarter-wavelength cover is prohibitively thick in practical applications, thus making the design of a magnetic wall with reduced thickness necessary. Fig. 5.1 (b) gives the system using HIS texture at the upper surface. Here, the thickness of the layer is much smaller than the wave-length ($\sqrt{\mu\epsilon}\omega d \ll 1$) which gives an inductive input impedance $Z_{sub} \approx j\omega\mu d$, while the textured surface (e.g., an array of metallic squares) may be modeled by a capacitive grid impedance $Z_g = 1/(j\omega C_g)$. The total surface impedance is expressed as the parallel connection of the inductive input impedance and the capacitive grid impedance [19]

$$Z_s = \frac{j\omega\mu d}{1 - \omega^2 C_g \mu d}. \quad (5.3)$$

Clearly, the imaginary part of the surface impedance tends to infinity at the resonant frequency $\omega_0 = 1/\sqrt{C_g \mu d}$, thus realizing a magnetic wall. Such composite layers referred to as artificial magnetic conductors or high impedance surfaces were proposed by Siven-

piper *et al.* [1, 20] and they are called *mushroom structure*. In that design, the texture surface formed as metal plates are arranged in a two-dimensional lattice, connected to the ground by vias as shown in Fig. 5.2. Note that the vias connectors are important for obliquely incident waves which can prevent waves with non-zero vertical electric field component to travel between the patch array and the ground.

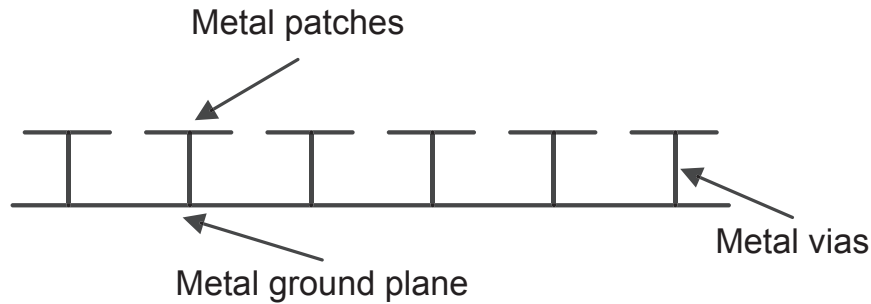


Figure 5.2: Cross-section of a high impedance surface [20].

Another advantage of the composite layered structures is that they may present a stopband for surface waves along the HIS surface. Such surface waves may interact with the space wave when they reach an edge or corner for a finite size structure at microwave or radio frequencies, thus reduce the radiation efficiency. Moreover, if multiple antennas share the same ground plane, surface waves may cause unwanted mutual coupling between them. Typically, bandwidth of HIS referred to as the stopband is defined as the frequency range that the reflection phase lies between $\pm\Delta\phi/2$, and the values of $\Delta\phi$ depends on the application.

It is desirable for the HIS bandwidth to be as wide as possible. Therefore, there has been a fair amount of research to increase the bandwidth of HIS [21–23]. However, we should note that neither of these approaches is able to achieve real broadband since passive HIS suffer from inherent physical limitations, as their upper limit of bandwidth was derived in Ref. [24]. Recently, active HIS loaded with non-Foster circuits have been proposed as an effective means to overcome these limitations, thus achieving ultra-wide bandwidth [25, 26]. In essence, this technique applies negative impedance components to

equalize the reactance response of the HIS structure and thus flatten its phase response with respect to frequency. However, as any active devices, the performance of an active HIS is limited due to the possibility of instability which has not been given enough attention yet. Therefore, in our work, a detailed stability analysis on the active HIS is presented based on the effective medium model, further to give the design specifications to achieve broadband properties. Furthermore, a sample design of active HIS with non-Foster loads is demonstrated and verified by full-wave simulations.

5.2 Effective Medium of Loaded HIS

Many properties of the HIS structure can be explained using an effective medium model. In general, the structure can be assigned a surface impedance equal to the impedance of a parallel connection of both grid impedance and the surface impedance of the grounded dielectric layer, thus leading to the equivalent circuit model of loaded HIS structure in terms of mushroom-type structures.

5.2.1 Equivalent Circuit Model

Based on the mushroom structure which is formed by grids of metallic square patches separated by dielectric slabs and connected to the ground plane with metallic vias, we may propose the loaded HIS structure while the geometry is shown in Fig. 5.3. Here, D is the period of the patches and the vias, L is the patch size, w is the gap between the patches, d is the thickness of the dielectric layer, and ε_r is the permittivity of the dielectric slab.

As proposed in Refs. [27, 28], the response of a loaded HIS can be accurately described using an equivalent parallel circuit with the grid impedance of the textured surface Z_g , the substrate impedance of a metal-backed dielectric slab with embedded vias Z_s , and the load impedance Z_L . Hence, the input (surface) impedance of an loaded HIS is given

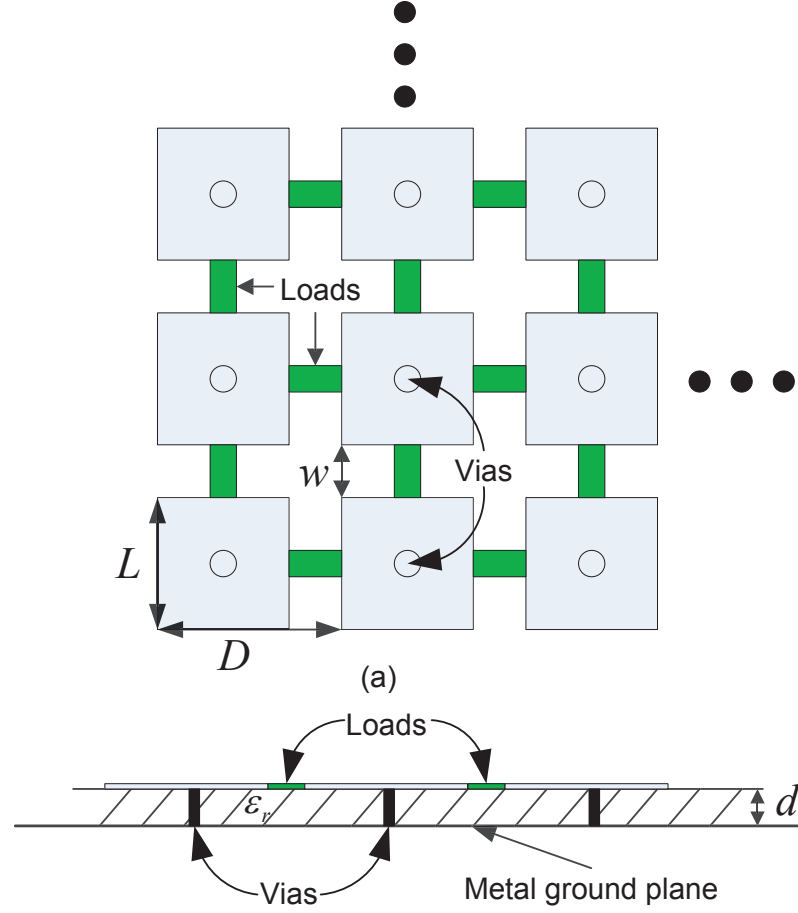


Figure 5.3: (a) View from the top of the actively-loaded HIS based on mushroom structure. (b) View from the side.

by

$$Z_{inp}^{-1} = Z_g^{-1} + Z_s^{-1} + Z_L^{-1}. \quad (5.4)$$

From Eq. (5.3), one might conclude that for a mushroom-type HIS, a highly capacitive element such as a patch with a very small gap would be modeled using a capacitor only which gives

$$Z_g = \frac{1}{j\omega C_g}, \quad (5.5)$$

while the thin grounded dielectric slab behaves as an inductor, thus leading to the sub-

strate impedance of the dielectric layer

$$Z_s \approx j\omega\mu d = j\omega L_s. \quad (5.6)$$

However, the accuracy of these equations is limited, since the simple LC parallel circuit is only valid as long as the wavelength is much longer than the size of the single unit cell, and also requires perfect metal patches. Moreover, the LC circuit model fails to predict the response of the structure for oblique incidence of TE and TM polarized waves.

The angle-dependent scattering properties of the mushroom-like structure can be accurately predicted using a homogenization model such as the one proposed in Ref. [27]. Thus, for an array of ideally conducting patches on the top of a dielectric substrate, the grid impedance of the TE and TM modes reads [27]

$$\begin{aligned} Z_g^{TM} &= -j \frac{\eta_{eff}}{2\alpha} \\ Z_g^{TE} &= -j \frac{\eta_{eff}}{2\alpha \left(1 - \frac{k_0^2 \sin^2 \theta}{2k_{eff}^2} \right)}, \end{aligned} \quad (5.7)$$

where $\eta_{eff} = \eta_0 / \sqrt{\varepsilon_{eff}}$ is the wave impedance of the substrate material, and $k_{eff} = k_0 \sqrt{\varepsilon_{eff}}$ is the wave number of the incident wave vector in the effective host medium. μ_0 , ε_0 and k_0 correspond to the permittivity, permeability and the wave number in free space, respectively. Here, the relative effective permittivity is defined by

$$\varepsilon_{eff} = (\varepsilon_r + 1)/2, \quad (5.8)$$

and α is the grid parameter

$$\alpha = \frac{k_{eff} D}{\pi} \ln \left(\frac{1}{\sin(\frac{\pi\omega}{2D})} \right) \quad (5.9)$$

Note that, in case of a lossless host medium, Eq. (5.7) can be written in the form of a single capacitance as shown in Eq. (5.5). For a normal incidence wave, since the response

of the HIS is the same for both TE and TM modes, the capacitance value reads

$$C_g^{TM,TE} = \frac{D\varepsilon_0(\varepsilon_r + 1)}{\pi} \ln \left(\frac{1}{\sin(\frac{\pi\omega}{2D})} \right). \quad (5.10)$$

However, by considering a normal lossy substrate material with the complex relative permittivity

$$\varepsilon_r = \varepsilon'_r - j\varepsilon''_r = \varepsilon'_r(1 - j \tan \delta), \quad (5.11)$$

the grid impedance should be represented through a parallel-RG circuit

$$Z_g^{TM,TE} = \frac{1}{G + j\omega C}. \quad (5.12)$$

By substitution of Eq. (5.11) into Eq. (5.7), the values of the lumped elements can be thereby obtained

$$\begin{aligned} C &= \frac{D\varepsilon_0(\varepsilon'_r + 1)}{\pi} \ln \left(\frac{1}{\sin(\frac{\pi\omega}{2D})} \right) \\ G &= \frac{\omega D\varepsilon_0\varepsilon''_r}{\pi} \ln \left(\frac{1}{\sin(\frac{\pi\omega}{2D})} \right). \end{aligned} \quad (5.13)$$

Subsequently, the substrate impedance Z_s for TM and TE cases from Ref. [29] is shown as

$$\begin{aligned} Z_s^{TM} &= j\omega\mu_0 \frac{\tan(\gamma_{TM}d)}{\gamma_{TM}} \frac{k^2 - \beta^2 - k_p^2}{k^2 - k_p^2} \\ Z_s^{TE} &= j\omega\mu_0 \frac{\tan(k_y\sqrt{\varepsilon_r}d)}{k_y\sqrt{\varepsilon_r}} \end{aligned} \quad (5.14)$$

where $k = k_0\sqrt{\varepsilon_r}$ is the wave number in the host medium, and

$$\gamma_{TM}^2 = \omega^2\varepsilon_0\varepsilon_t\mu_0 - \frac{\varepsilon_t}{\varepsilon_n}\beta^2 \quad (5.15)$$

$$k_p = \frac{1}{D\sqrt{\frac{1}{2\pi} \ln \frac{D^2}{4r_0(D-r_0)}}} \quad (5.16)$$

are the related parameters. In addition, r_0 is the radius of the vias, ε_t is the relative

permittivity for the fields along the transversal plane equal to ε_r for thin and vertical vias, and ε_n is the relative permittivity for the fields along the normal of the medium

$$\varepsilon_n = \varepsilon_t \left(1 - \frac{k_p^2}{k^2 \varepsilon_t} \right). \quad (5.17)$$

Similarly, we may rewrite the substrate impedance in form of a single inductance as shown in Eq. (5.6). For the normal incidence, the inductance value is given by

$$L_s^{TM,TE} = \mu_0 \frac{\tan(kd)}{k}. \quad (5.18)$$

Note that L_s is a frequency-dependent parameter, although it is approximate to $L_s \approx \mu_0 d$ for thin substrate with $kd \ll 1$. As before, by accounting the effect of substrate losses, we may present a more accurate model of the substrate impedance using a series-RL circuit

$$Z_s^{TM,TE} = R_s + j\omega L_s, \quad (5.19)$$

Once again, substitution of Eq. (5.11) into Eq. (5.14) gives the corresponding circuit parameters of the substrate impedance

$$\begin{aligned} L_s &= \mu_0 d \frac{\sqrt{\sin^2 x + \sinh^2(y)}}{\sqrt{\cos^2 x + \sinh^2(y)} \sqrt{x^2 + y^2}} \\ &\quad \times \cos \left[\tan^{-1} \left(\frac{\sinh(2y)}{\sin(2x)} \right) - \tan^{-1} \left(\frac{y}{x} \right) \right] \\ R_s &= \omega \mu_0 d \frac{\sqrt{\sin^2 x + \sinh^2(y)}}{\sqrt{\cos^2 x + \sinh^2(y)} \sqrt{x^2 + y^2}} \\ &\quad \times \sin \left[\tan^{-1} \left(\frac{\sinh(2y)}{\sin(2x)} \right) - \tan^{-1} \left(\frac{y}{x} \right) \right], \end{aligned} \quad (5.20)$$

where x and y are defined by

$$\begin{aligned} x &= k_0 d \sqrt{\frac{\epsilon'_r}{\cos \delta}} \cos \frac{\delta}{2} \\ y &= k_0 d \sqrt{\frac{\epsilon'_r}{\cos \delta}} \sin \frac{\delta}{2}. \end{aligned}$$

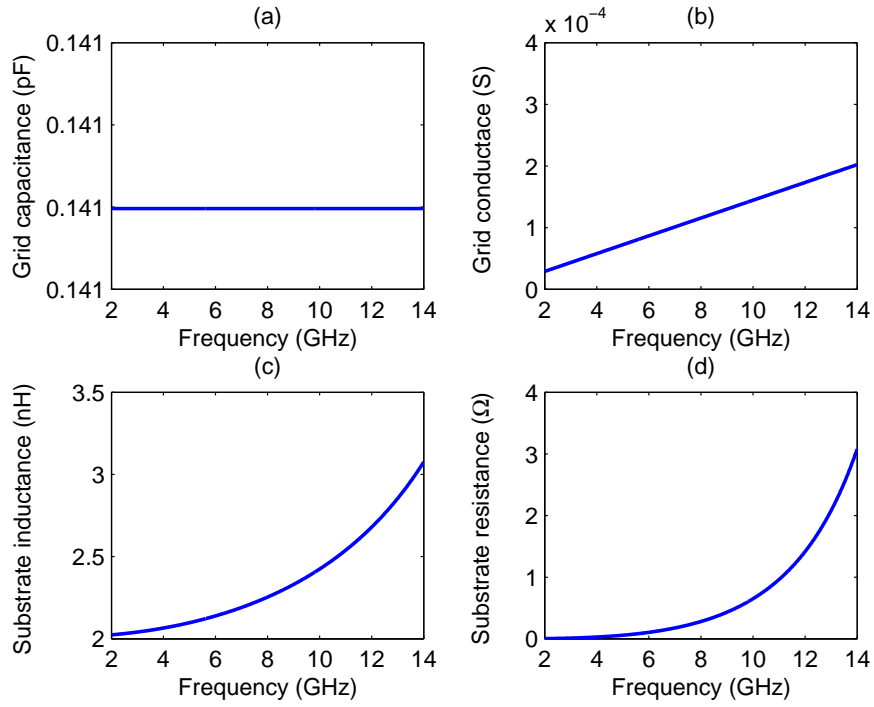


Figure 5.4: Equivalent circuit parameters extracted from an unloaded HIS. (a) Grid capacitance C . (b) Grid conductance G . (c) Substrate inductance L_s . (d) Substrate resistance R_s .

To demonstrate this equivalent circuit model, here we may apply it to an unloaded HIS with lossy patch-type surface and compare to the simulation results by HFSS. The substrate parameters are $\epsilon_r = 4.4 - j0.088$ and thickness $d = 1.6\text{mm}$ (typical of the commercial FR4). Patch elements are characterized by the periodicity $D = 6\text{mm}$, and the gap spacing $w = 0.9\text{mm}$. The corresponding circuit parameters can be extracted from Eqs. (5.13) and (5.20), as shown in Fig. 5.4. Clearly, it is shown that both the

substrate impedance and grid capacitance are not purely imaginary, although the values of the grid conductance and substrate resistance are relatively small. Furthermore, we note that, except the grid capacitance, all other parameters are frequency dependent which should be taken into account during the stability analysis for an actively-loaded HIS. Fig. 5.5 shows the simulated input impedance of this HIS structure, as compared to the results obtained from the circuit models. It is shown that there is good agreement between the simulation results and the proposed circuit model, although we should note that the parallel-LC circuit model is very limited in modeling a practical HIS.

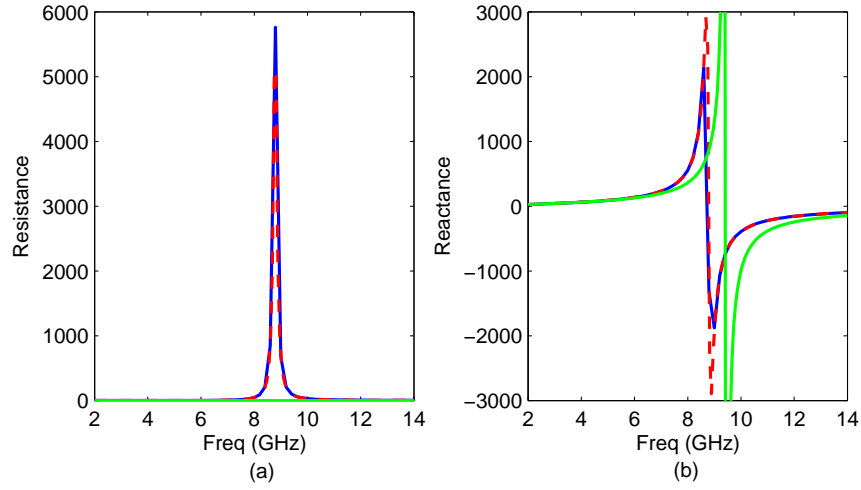


Figure 5.5: Input impedance of an unloaded mushroom-type HIS simulated using HFSS, as compared to the circuit models. Here, two different circuit models are presented: One is the proposed accurate circuit model represented by red-dashed lines, and the other one corresponds to the simple parallel-LC circuit model represented by green-solid lines. The simulated case is plotted with blue-solid lines. (a) Resistance. (b) Reactance. Clearly, the simulation results fits the proposed circuit model very well, and disagree with the LC model.

5.2.2 Reflection Properties

We now consider the reflection properties of the actively-loaded HIS based on the effective circuit model. As shown in Fig. 5.6, the wave reflection at the HIS surface can be modeled

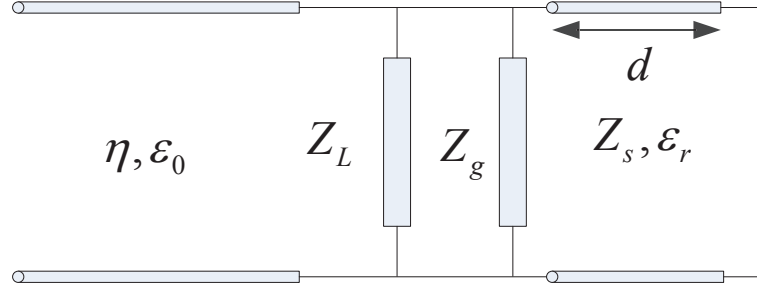


Figure 5.6: Transmission-line model for modeling the wave reflection at an actively-loaded HIS. η is the free-space impedance.

through a transmission-line model [29], which leads to the reflection coefficient

$$\Gamma = \frac{Z_{inp} - \eta}{Z_{inp} + \eta}. \quad (5.21)$$

Here, Z_{inp} is the input impedance of the HIS, as referred to Eq. (5.4).

As proposed in Ref. [1], the bandwidth of a HIS structure is defined as the frequency range where the absolute value of the impedance is larger than the free-space impedance. This condition corresponds to the reflection phase crossing through $\pm\pi/2$, when the surface impedance is equal in magnitude to the impedance of free space. Hence, for a loaded HIS structure, we can define the bandwidth BW by solving two positive frequencies $\omega_{+\eta}$ and $\omega_{-\eta}$ for which the impedance Z_{inp} is equal to $+\eta$ and $-\eta$, respectively. Starting from the unloaded case, we now express the surface impedance in the form of lumped elements as follows:

$$Z_{inp} = \frac{R_s + j\omega L_s}{1 + R_s G + j\omega(L_s G + C R_s) - \omega^2 L_s C}. \quad (5.22)$$

As is well known, the resonant frequency ω_0 corresponding to an infinite surface impedance occurs when the denominator of Eq. (5.22) is null. In particular, the grid conductance G and the substrate resistance R_s for a normal HIS structure is small and

can be neglected when evaluating the bandwidth of an unloaded HIS structure. Hence, we can have the following equation which can be solved for the resonant frequency ω_0

$$1 - \omega^2 L_s(\omega) C = 0. \quad (5.23)$$

Here, it should be noted that $L_s(\omega)$ is a frequency dependent inductance, which is different from the LC model expression. The frequency variation of this parameter is described by Eq. (5.20). In a similar manner to Ref. [1], we may derive the fractional bandwidth of an unloaded HIS in the following approximation

$$\frac{\Delta\omega}{\omega_0} \approx \frac{1}{\eta} \sqrt{\frac{L_{s0}}{C}}, \quad (5.24)$$

where L_{s0} is the inductance value corresponding to the resonant frequency. Clearly, one may conclude that an increase of the substrate inductance or a decrease of the grid capacitance leads to an increase of the fractional bandwidth, which will be used as the principle of the actively-loaded HIS structure.

As proposed in Ref. [25, 26], here, we assume the load impedance Z_L connected between patch pairs consists of a parallel negative LC network with the values of L_L and C_L , thus the total equivalent inductance and capacitance of the loaded HIS can be approximated as

$$\begin{aligned} L_{HIS} &= \frac{L_s L_L}{L_s + L_L} \\ C_{HIS} &= C + C_L. \end{aligned} \quad (5.25)$$

Clearly, $\sqrt{L_{HIS}/C_{HIS}}$ can be manipulated to improve the bandwidth, and ideally an infinite bandwidth can be achieved in the limit when $L_L = -L_s$ or $C_L = -C$. However, this cannot be achieved in practice due to the stability conditions.

Once again, we may validate the above analysis by full-wave simulations based on an unloaded HIS with the same physical definitions as before. As shown in Fig. 5.7, the

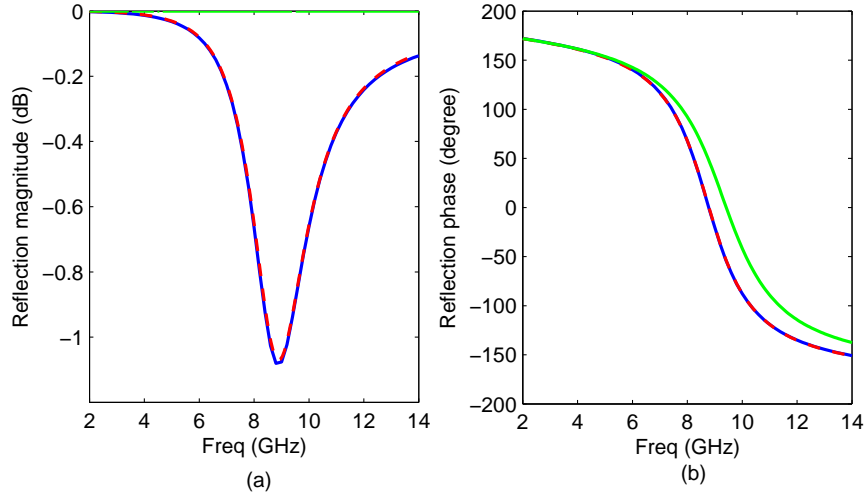


Figure 5.7: Reflection coefficient of an unloaded mushroom-type HIS. As before, the simulated case is represented by blue-solid lines, and the proposed circuit model is represented by red-dashed lines, while the simple parallel-LC circuit model is green-solid. (a) Reflection Magnitude. (b) Reflection phase. It is evident that the reflection coefficient calculated using the proposed circuit model matches very well with the simulation results.

reflection coefficient of the HIS structure obtained from Eq. (5.21) is plotted based on the circuit models, as compared to the simulation results from HFSS. It is evident that the simulation results agree with the analysis based on the proposed circuit model, although the LC model again proves to be invalid for this HIS structure. By inspection of Fig. 5.7, one may notice that the resonance frequency of this HIS structure is $f_0 = \omega_0/2\pi = 8.8\text{GHz}$, and fractional bandwidth $FBW = 29.6\%$, exhibited as narrow bandwidth.

5.2.3 Surface Waves

For many applications, the properties of wave propagating in structures are very important. Here, we shall study the surface wave along an loaded HIS, further to derive the dispersion relation for both TM and TE waves, using the expressions for surface wave on an impedance surface.

In a similar manner to Ref. [19], the loaded HIS structure can be modeled by giving

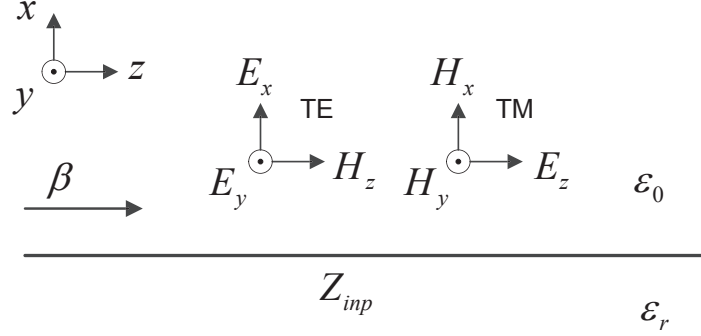


Figure 5.8: Surface TE and TM waves along a planar impedance surface.

an isotropic surface in the YZ plane with the impedance Z_{inp} , as shown in Fig. 5.8. We assume the half-space $x > 0$ is filled by air, with the parameter ϵ_0 and μ_0 . Thus, in the interface $x = 0$, the following equations can be derived in terms of Cartesian components due to the boundary conditions

$$\begin{aligned} E_z &= Z_{inp} H_y \quad (\text{TM waves}) \\ E_y &= -Z_{inp} H_z \quad (\text{TE waves}). \end{aligned} \quad (5.26)$$

For TE waves, we assume the Y component of the electric field as follows

$$E_y = A e^{-j\beta z - \alpha x} \quad (5.27)$$

where A is a constant, α is the decay factor, and β is the propagation vector. Applying the Helmholtz equation

$$(\nabla^2 + k_0^2) E_y = 0, \quad (5.28)$$

we can derive the dispersion relation for TE surface waves by relating α , β and ω

$$\alpha^2 - \beta^2 + k_0^2 = 0 \quad (5.29)$$

Moreover, following the Maxwell equation

$$\vec{H} = -\frac{1}{j\omega\mu_0}\nabla \times \vec{E}, \quad (5.30)$$

we may have

$$H_z = \frac{\alpha}{j\omega\mu_0}E_y. \quad (5.31)$$

Substitution of Eq. (5.31) into Eq. (5.26) gives the decay factor for TE waves

$$\alpha = -\frac{j\omega\mu_0}{Z_{inp}}, \quad (5.32)$$

while the propagation vector can be obtained from Eq. (5.29)

$$\beta = k_0 \sqrt{1 - \frac{\eta^2}{Z_{inp}^2}} \quad (\text{TE waves}) \quad (5.33)$$

where $k_0 = \omega\sqrt{\mu_0\epsilon_0}$ is the wave vector in free space. Similarly, the dispersion parameters for TM waves can be derived as

$$\begin{aligned} \alpha &= -j\omega\epsilon_0 Z_{inp} \quad (\text{TM waves}) \\ \beta &= k_0 \sqrt{1 - \frac{Z_{inp}^2}{\eta^2}} \quad (\text{TM waves}). \end{aligned} \quad (5.34)$$

These equations imply that, propagating surface waves with real propagation vectors β only occur when the surface impedance Z_{inp} is purely imaginary. Therein, the decay factor α becomes purely real (see Eqs. (5.32) and (5.34)). Furthermore, it can be seen that, only a surface whose impedance is purely capacitive can support TE waves, while TM waves can only occur on an inductive surface. However, we should note that these phenomena may not occur in practical HIS structures with lossy substrates, since the effect of loss from the host medium inevitably leads to an complex surface impedance as discussed before. Fig. (5.9) shows the dispersion diagram for bound surface waves

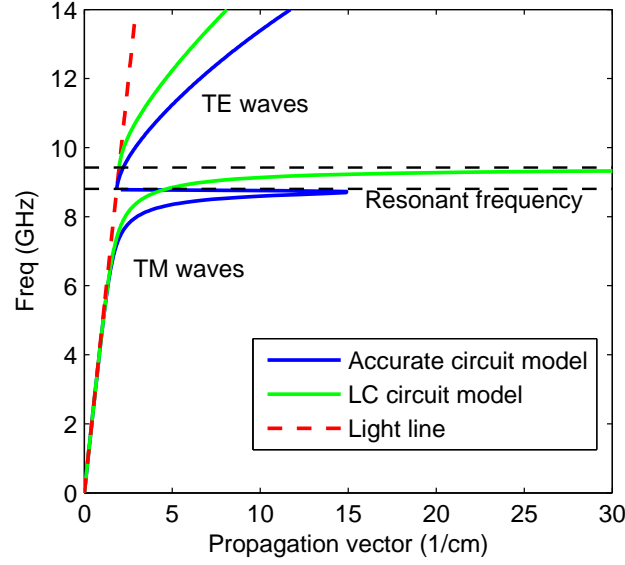


Figure 5.9: Dispersion diagrams for TE and TM waves along an unloaded HIS structure based on its equivalent circuit model.

along a HIS structure with the physical parameters defined as before. Here, both the accurate circuit model accounting the material loss and the simple LC model are used for comparison. clearly, the results obtained from the LC model agree with Sivenpiper's work [1, 20], both TE and TM waves lie below the light line and isolated by the resonant frequency ω_0 . Near the resonant frequency, the TM dispersion curve extends to an infinitely large wave vector. However, the accurate circuit model predicts a different performance, that is, the addition of loss has now allowed propagation in the gap which fits the lossy medium theory [30]. Moreover, it is shown that the propagation vector of the TM wave will hold at a fixed value, without extending to an infinity. Finally, it should be emphasized that the effective medium model is actually inaccurate when modeling the surface waves of an HIS structure since it does not predict an actual bandgap. Nevertheless, a surface-wave bandgap can always be found in both measurements and numerical simulations.

5.3 Stability Characterization of Actively-Loaded HIS

5.3.1 Stability of HIS with Non-Foster Loads

By inspection of the effective medium of an loaded HIS structure, it is shown that an increase of the substrate inductance or a decrease of the grid capacitance always correspond to an increase of the bandwidth, although we can notice that the achievable bandwidth for a passive HIS structure is actually very limited [24]. Recently, actively-loaded HIS have been proposed as a means to overcome these limitations by incorporating non-Foster elements, thus, altering the surface properties [25, 26]. However, very little attention were given to the stability issue of the actively-loaded HIS structures. In particular, the previous stability analysis are based on a parallel-LC circuit model which is inaccurate to model a real HIS structure with losses as we mentioned previously. Here, we will now investigate the stability of an active HIS with parallel negative RLC loads based on the proposed circuit model, since it can be easily seen that a load consisting of only a negative inductance or a negative capacitance will lead to instability when connected between the patch pairs on top of a lossy dielectric substrate. As shown in Fig. 5.10, the HIS structure is presented in terms of its cross-section and equivalent circuit. The load impedance is specified as a parallel-RLC network, with the resistance R_L , the inductance L_L and the capacitance C_L .

Here, we assume that all the circuit parameters in Fig. 5.10 are ideal lumped elements, then the Routh-Hurwitz technique can be applied in the determination of the stability bounds for the active load, by examining the solutions to the characteristic equation of the system. As was suggested in Ref. [31], here, we define the impedance of a closed loop circuit as follows

$$Z(s) = Z_0(s) + Z_L(s) = Z_g(s) \parallel Z_s(s) + Z_L(s), \quad (5.35)$$

which is the series of the unloaded HIS impedance Z_0 and load impedance Z_L . Clearly,

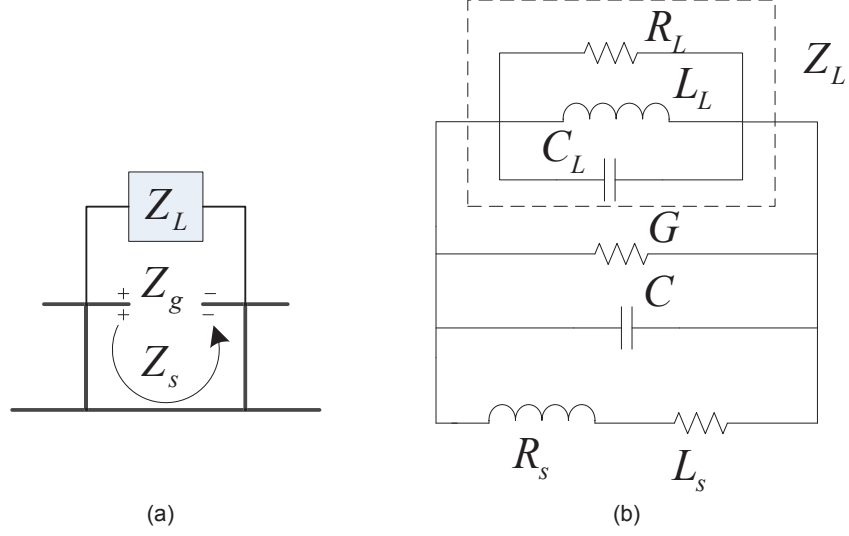


Figure 5.10: An active HIS loaded with negative inductors. (a) Cross-section. (b) Equivalent circuit.

the input surface impedance Z_{inp} is equal to $Z_0 \parallel Z_L$. Writing $Z(s) = Z_n(s)/Z_d(s)$, thus, the numerator and denominator of the impedance will be found, respectively. Finally, the characteristic polynomial of the system is given by the following expression

$$Z_n(s) = \sum_{k=0}^K a_k s^k = 0 \quad (5.36)$$

where its coefficients are obtained as follows

$$\begin{aligned} a_3 &= RR_L L_s L_L (C + C_L) \\ a_2 &= R(L_s L_L + R_s R_L L_L C_L) + R_L L_L (R R_s C + L_s) \\ a_1 &= R(R_L L_s + R_s L_L) + R_L L_L (R + R_s) \\ a_0 &= R R_s R_L \end{aligned}$$

where $R = 1/G$ is the grid resistance. The system is stable if and only if all roots of Eq. (5.36) are in the left-hand side (LHS) of the complex plane. By applying the Routh-Hurwitz criterion [32], such that, a Routh array is constructed using the coefficients of

the characteristic polynomial. It is said that, all roots are in the LHS of the complex plane if and only if all coefficients in the first column have the same sign, thus leads to the following stability conditions

$$C_L < -C \quad (5.37)$$

$$0 > L_L > -\frac{(R + R_L)L_s^2}{(R + R_L)L_s + R_L R R_s (C + C_L)}, \quad (5.38)$$

with $R_L < 0$. It is evident that the range of the stable values for the load inductance is restricted by the determination of the load capacitance. Assuming a fixed load resistance, we note that an increase of the negative capacitance must correspond to an decrease of lower limit of the negative inductance, in other words, a greater range of stable L_L can be obtained. In particular, as the load capacitance approaches its limit where $C_L = -C$, it follows the maximum stable range of the load inductance $0 > L_L \gtrsim -L_s$, thus, the resonant frequency becomes 0 and an infinite bandwidth can be achieved. However, it is not achievable for a practical HIS design since the the circuit parasitics always accompany the realization of negative impedance components. Furthermore, we should note that the analytical stability bound from Eqs. (5.37) and (5.38) will no longer hold in practical cases, since the negative impedance components obtained from NIC circuits may deviate from the ideal element model. Such that, a higher-ordered equivalent circuit fit must be applied to model the system which makes the application of the Routh-Hurwitz criterion very complicated. To deal with such situations, the frequency domain technique would be preferable, for which the measured or simulated impedance of an NIC can be tested for stability in combination with the effective medium. As proposed before, two ways of investigating the stability of active metamaterials with practical non-Foster loads have been introduced which are also applicable for the active-loaded HIS structures, one is the Nyquist stability analysis and the other is the immitance-based stability analysis.

We will now apply the above analysis to a practical example. Once again, a mushroom-type HIS is used, for which the physical parameters are defined as before. The structure consisted of an array of ideally conducting square patches, with a period of 6 mm and

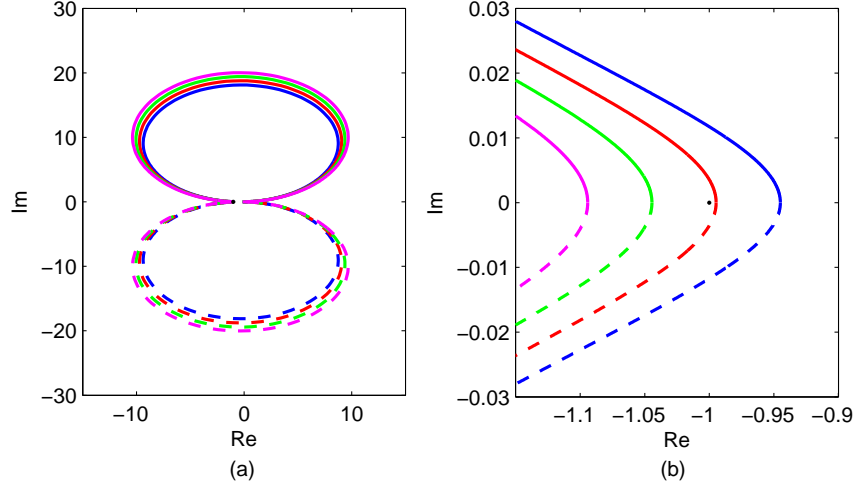


Figure 5.11: Nyquist contours of a mushroom-type HIS loaded with negative inductors. The inductance value is varied from the unstable to the stable cases. The Routh-Hurwitz method gives a stable range of inductances at $L_L < -2.02nH$; the Nyquist method clearly agrees with that. (a) The Nyquist contours for $L_L = (-1.9$ (blue), -2.0 (red), -2.1 (green), -2.2 (magenta)) nH . (b) Magnification of the Nyquist contours around the -1 point. It is evident that for $L_L = (-1.9, -2.0)nH$ the systems are unstable, while for $L_L = (-2.1, -2.2)nH$ the systems are stable.

a gap between the patches of 0.9 mm. The thickness of the board was 1.6 mm, and the dielectric permittivity was $\epsilon_r = 4.4 - j0.088$. A load is added to each patch pair with $R_L = -1000\Omega$ and $C_L = -1pF$. Using the Routh-Hurwitz method, the range of stable values for the load inductance can be found from Eq. (5.38) as $L_L < -\mu d < -2.01nH$. Subsequently, the Nyquist criterion is applied to verify this stable range values. By inspection the locations of the poles and zeros, we can therefore define the Nyquist evaluation of a source-impedance load-admittance product as Z_L/Z_0 . Here, the input impedance of an unloaded HIS structure Z_0 is defined as the Nyquist load, and Z_L is defined as a source due to the properties of OCS NIC as mentioned earlier in the active metamaterials design. However, it should be noted that for practical cases, the determination of whether Z_L is the source or the load may change. As shown in Fig. 5.11, the Nyquist contours are plotted for a range of values, from $L_L = -2.1$ to $-1.9nH$. Since a stable contour will not encircle the -1 point, it is shown that this method agrees with the results of the Routh-Hurwitz calculation; for $L_L = -2.1nH$ the contour does not

circle the -1 point, while for $L_L = -2.0nH$ it does, signifying instability. Moreover, the stability check using immittance-based analysis is omitted here since we found that the variation of the inductance value is too sensitive to be detected in the immittance-space.

5.3.2 Application in the Design of Broadband Active HIS

It is now straightforward to include the stability analysis in the design of broadband active HIS. In contrast to the previous work which gives individual attention to the increase of the equivalent inductance by incorporating the negative inductance components [25, 26], we will present a technique by controlling both the inductance and the capacitance of the HIS circuit, to achieve a broadband with fixed resonance HIS design. Such that, the HIS inductance needs to be increased while the capacitance must be decreased. By employing the parallel negative RLC loads as proposed earlier, we shall rewrite Eqs. (5.23) and (5.24) by replacing the circuit parameters as follows

$$1 - \omega^2 \frac{L_s L_L}{L_s + L_L} (C + C_L) = 0 \quad (5.39)$$

$$\frac{\Delta\omega}{\omega_0} \approx \frac{1}{\eta} \sqrt{\frac{L_s L_L}{(L_s + L_L)(C + C_L)}}. \quad (5.40)$$

Here, it is noted that the resistance components from the unloaded HIS structure and active loads may contribute a negligible effect when evaluating the bandwidth of a normal HIS structure, thus can be ignored for this analysis. Furthermore, we assume that the bandwidth of the actively-loaded HIS is increased by N ($N > 1$), while the resonant frequency remains unchanged, as compared to the unloaded case. Thus, the values of the load inductance and capacitance can be derived as

$$L_L = -\frac{N}{N+1} L_s \quad (5.41)$$

$$C_L = -\left(\frac{1}{N} + 1\right) C. \quad (5.42)$$

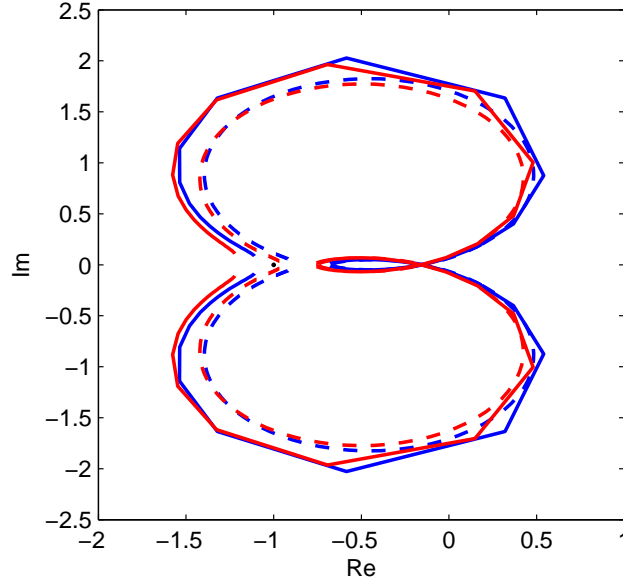


Figure 5.12: Simulated Nyquist stability plots of the HIS structure with NIC loads, as compared to the analytical results obtained from the circuit model. In all cases, the solid lines represent the simulation results, while the dashed line represents the analytical solution based on the circuit model. The $N = 2$ case is plotted in blue, while the $N = 3$ case is plotted in red. It is evident that in all cases the Nyquist contour does not encircle the -1 point no matter what it is from, thus conforming stability.

From the above equations, it is apparent that an increase of the bandwidth implies an increase of the load capacitance but, at the same time, a reduction of the load inductance. We also conclude that the bandwidth may be limited due to the stability bound for the load inductance, whereas, for the load capacitance, the bandwidth will not be affected since the stability condition is always satisfied as was suggested by Eq. (5.37).

In order to illustrate how the load inductance and capacitance can be manipulated to achieve the desired bandwidth, a simulation example from HFSS is presented here, as compared to the circuit model analysis. Once again, the parameters of the unloaded structure are as before. The active loads can then be obtained from Eqs. (5.41) and (5.42) by defining the increase factor N . For $N = 2$, the parallel RLC network can be analytically derived as follows

$$R_L = -1000\Omega, L_L = -1.34nH, C_L = -0.2pF, \quad (5.43)$$

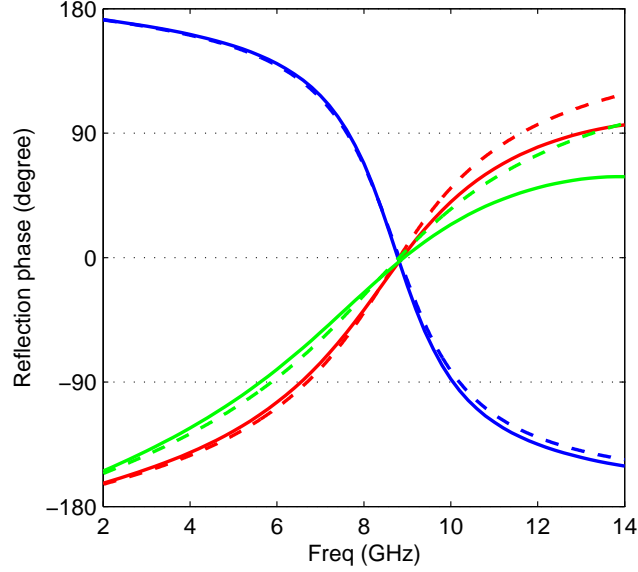


Figure 5.13: Simulated reflection phase of the actively-loaded HIS, as compared to the analytical results obtained from the circuit model. In all cases, the simulation results are plotted by solid lines, while the dashed lines represent the analytical results. Here, three cases are plotted. Case (I) (blue line) corresponds to the unloaded HIS, while case (II) (red line) and (III) (green line) correspond to the actively-loaded HIS with an increased bandwidth of 2 and 3, respectively.

while for $N = 3$, we may have

$$R_L = -1000\Omega, \quad L_L = -1.5nH, \quad C_L = -0.18pF. \quad (5.44)$$

From Eqs. (5.37) and (5.38), it can be easily seen that both cases satisfy the stability conditions. However, we may use the Nyquist stability criterion to verify these results. The stability contours are plotted in Fig. 5.12 including both simulation and analytical results, and confirms the stability for both cases.

Fig. 5.13 shows the corresponding reflection phases. Clearly, it is shown that the surface properties have been altered by incorporating the active loads. Furthermore, we note that an appropriate selection of the RLC circuit elements will achieve a broadband but with fixed resonance HIS design. Comparing to the unloaded case with the fractional bandwidth 29.6%, the active structure shows that the HIS bandwidth can be increased to

61.8% and 84% with different loading circuits, respectively. Finally, we should note that, for actual actively-loaded HIS design, the resonant frequency need to be cut down to be compatible with the NIC design. Also, the ideally negative circuit elements should be replaced by the actual NIC circuit which make the stability check using Nyquist stability criterion or immitance-based stability analysis necessary.

5.4 Conclusions

This chapter presents the characterization of active high impedance surfaces with non-Foster loads. Starting from the effective medium of loaded HIS structure, we have proposed an accurate circuit model accounting the effect of losses from the substrate materials. Comparing with the conventional LC circuit model, it is shown that our circuit model agrees very well with the simulation results. Furthermore, the reflection properties and surface wave of the loaded HIS are studied and verified by simulations based on the effective medium. It is shown that the bandwidth of a normal unloaded HIS is dependent on the inductance and capacitance of the equivalent circuit by ignoring the resistance parts, which also gives the principle of active-loaded HIS.

However, as in the design of active metamaterials, the stability of actively-loaded HIS also needs to be examined. Here, we apply the Routh-Hurwitz technique to give the stability conditions for a parallel negative RLC loaded HIS structure based on the equivalent circuit model, where the stability bounds for the negative inductance and capacitance are derived. Furthermore, the Nyquist criterion is used to verify the proposed stability conditions.

Finally, the application of the stability analysis in the design of actively-loaded HIS is introduced. It is shown by choosing appropriate NIC loads, we can achieve a broadband but with fixed resonance HIS design, while keeping the system stable. Simulation results have verified our technique for the ideally NIC case. In the future, the practical NIC circuit will be applied so as to provide the experimental demonstration.

References

- [1] D. Sievenpiper, L. Zhang, R. F. Broas, N. G. Alexopolous, and E. Yablonovitch, “High-impedance electromagnetic surfaces with a forbidden frequency band,” *Microwave Theory and Techniques, IEEE Transactions on*, vol. 47, no. 11, pp. 2059–2074, 1999.
- [2] S. Tretyakov and C. Simovski, “Dynamic model of artificial reactive impedance surfaces,” *Journal of electromagnetic waves and applications*, vol. 17, no. 1, pp. 131–145, 2003.
- [3] C. Sochava, “High-impedance surfaces based on self-resonant grids. analytical modelling and numerical simulations,” *Progress In Electromagnetics Research*, vol. 43, pp. 239–256, 2003.
- [4] C. R. Simovski, P. de Maagt, and I. V. Melchakova, “High-impedance surfaces having stable resonance with respect to polarization and incidence angle,” *Antennas and Propagation, IEEE Transactions on*, vol. 53, no. 3, pp. 908–914, 2005.
- [5] S. Maci and P.-S. Kildal, “Hard and soft surfaces realized by fss printed on a grounded dielectric slab,” in *Antennas and Propagation Society International Symposium, 2004. IEEE*, vol. 1. IEEE, 2004, pp. 285–288.
- [6] Z. A. Kaprielian, “Dielectric properties of a lattice of anisotropic particles,” *Journal of Applied Physics*, vol. 27, no. 1, pp. 24–32, 1956.
- [7] C.-C. Chen, “Transmission through a conducting screen perforated periodically with apertures,” *Microwave Theory and Techniques, IEEE Transactions on*, vol. 18, no. 9, pp. 627–632, 1970.
- [8] Y. Huang, A. De, Y. Zhang, T. K. Sarkar, and J. Carlo, “Enhancement of radiation along the ground plane from a horizontal dipole located close to it,” *Antennas and Wireless Propagation Letters, IEEE*, vol. 7, pp. 294–297, 2008.
- [9] B. A. Munk, *Frequency selective surfaces: theory and design*. John Wiley & Sons, 2005.
- [10] J. A. Higgins, H. Xin, A. Sailer, and M. Rosker, “Ka-band waveguide phase shifter using tunable electromagnetic crystal sidewalls,” *Microwave Theory and Techniques, IEEE Transactions on*, vol. 51, no. 4, pp. 1281–1288, 2003.

- [11] D. Chicherin, S. Dudorov, D. Lioubtchenko, V. Ovchinnikov, S. Tretyakov, and A. V. Räisänen, “Mems-based high-impedance surfaces for millimeter and submillimeter wave applications,” *Microwave and optical technology letters*, vol. 48, no. 12, pp. 2570–2573, 2006.
- [12] F.-R. Yang, K.-P. Ma, Y. Qian, and T. Itoh, “A novel tem waveguide using uniplanar compact photonic-bandgap (uc-pbg) structure,” *Microwave Theory and Techniques, IEEE Transactions on*, vol. 47, no. 11, pp. 2092–2098, 1999.
- [13] D. F. Sievenpiper, J. H. Schaffner, H. J. Song, R. Y. Loo, and G. Tangonan, “Two-dimensional beam steering using an electrically tunable impedance surface,” *Antennas and Propagation, IEEE Transactions on*, vol. 51, no. 10, pp. 2713–2722, 2003.
- [14] N. Engheta, “Thin absorbing screens using metamaterial surfaces,” in *Antennas and Propagation Society International Symposium, 2002. IEEE*, vol. 2. IEEE, 2002, pp. 392–395.
- [15] S. Tretyakov and S. Maslovski, “Thin absorbing structure for all incidence angles based on the use of a high-impedance surface,” *Microwave and Optical Technology Letters*, vol. 38, no. 3, pp. 175–178, 2003.
- [16] Q. Gao, Y. Yin, D.-B. Yan, and N.-C. Yuan, “A novel radar-absorbing-material based on ebg structure,” *Microwave and optical technology letters*, vol. 47, no. 3, pp. 228–230, 2005.
- [17] S. Simms and V. Fusco, “Thin radar absorber using artificial magnetic ground plane,” *Electronics Letters*, vol. 41, no. 24, pp. 1311–1313, 2005.
- [18] D. M. Pozar, *Microwave engineering*. Wiley. com, 2009.
- [19] S. Tretyakov, *Analytical modeling in applied electromagnetics*. Artech House, 2003.
- [20] D. Sievenpiper, *High-impedance electromagnetic surfaces*. Dept. Elect. Eng., Univ. California, Los Angeles, CA, 1999.
- [21] L. Yousefi, B. Mohajer-Iravani, and O. M. Ramahi, “Enhanced bandwidth artificial magnetic ground plane for low-profile antennas,” *Antennas and Wireless Propagation Letters, IEEE*, vol. 6, pp. 289–292, 2007.
- [22] G. Gampala and A. B. Yakovlev, “Wideband high impedance surface for x-band antenna applications,” in *Antennas and Propagation Society International Sympo-*

- sium*, 2007 *IEEE*. IEEE, 2007, pp. 1329–1332.
- [23] D. J. Kern, D. H. Werner, A. Monorchio, L. Lanuzza, and M. J. Wilhelm, “The design synthesis of multiband artificial magnetic conductors using high impedance frequency selective surfaces,” *Antennas and Propagation, IEEE Transactions on*, vol. 53, no. 1, pp. 8–17, 2005.
 - [24] M. F. Samani and R. Safian, “On bandwidth limitation and operating frequency in artificial magnetic conductors,” *Antennas and Wireless Propagation Letters, IEEE*, vol. 9, pp. 228–231, 2010.
 - [25] D. J. Gregoire, C. R. White, and J. S. Colburn, “Wideband artificial magnetic conductors loaded with non-foster negative inductors,” *IEEE Antennas and Wireless Propagat. Lett.*, vol. 10, pp. 1586–1589, 2011.
 - [26] Y. Ding and V. Fusco, “Loading artificial magnetic conductor and artificial magnetic conductor absorber with negative impedance convertor elements,” *Microwave and Optical Technology Letters*, vol. 54, no. 9, pp. 2111–2114, 2012.
 - [27] O. Luukkonen, C. Simovski, G. Granet, G. Goussetis, D. Lioubtchenko, A. V. Raisanen, and S. A. Tretyakov, “Simple and accurate analytical model of planar grids and high-impedance surfaces comprising metal strips or patches,” *Antennas and Propagation, IEEE Transactions on*, vol. 56, no. 6, pp. 1624–1632, 2008.
 - [28] F. Costa, A. Monorchio, and G. Manara, “Analysis and design of ultra thin electromagnetic absorbers comprising resistively loaded high impedance surfaces,” *Antennas and Propagation, IEEE Transactions on*, vol. 58, no. 5, pp. 1551–1558, 2010.
 - [29] O. Luukkonen, C. R. Simovski, A. V. Raisanen, and S. A. Tretyakov, “An efficient and simple analytical model for analysis of propagation properties in impedance waveguides,” *Microwave Theory and Techniques, IEEE Transactions on*, vol. 56, no. 7, pp. 1624–1632, 2008.
 - [30] R. Syms, O. Sydoruk, and L. Solymar, “Lossy metamaterials: No effective medium properties without noise,” *Physical Review B*, vol. 84, no. 23, p. 235150, 2011.
 - [31] K. Z. Rajab, Y. Hao, D. Bao, C. G. Parini, C. Vazquez, J. Philippakis, and M. Philippakis, “Stability of active magnetoinductive metamaterials,” *J. Appl. Phys.*, vol. 108, p. 054904, 2010.

- [32] A. Hurwitz, “Selected papers on mathematical trends in control theory,” 1964.

Chapter 6

Design and Analysis of Negative Impedance Converters

As mentioned before, in order to achieve broadband properties, active structures with non-Foster loads have been proposed as an effective approach to overcome the inherent limitation of passive structures. In general, the negative non-Foster elements are realized by terminating a two-port called a Negative Impedance Converter (NIC) in the corresponding positive elements. Hence, in this chapter, the basic literature review on theoretical analysis, design and stability issues of negative impedance converters (NICs) are discussed first. Subsequently, different categories of NICs are proposed and realized depending on the active elements, one is based on operational amplifiers (Op-AMPs), and the other are transistorized NICs. In particular, two types of transistor based NIC including both floating and grounded cases are designed, built and tested.

6.1 Overview of NICs

Although the concept of negative impedance converter (NIC) circuit was proposed in the 1920s, Merrill introduced the realization of a NIC comprised of vacuum tube circuits

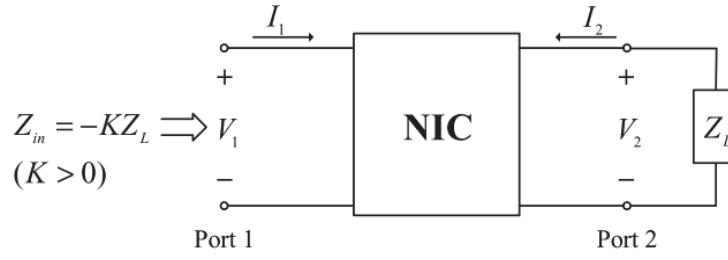


Figure 6.1: An ideal NIC modeled as a two-port network. [5]

in 1951 [1], in that a negative resistor called negative impedance repeater is created to increase transmission gains on telephone lines. The first practical transistorized NICs were designed, built and tested by Linvill [2] in 1954. He built both balanced and unbalanced voltage inversion NICs, to implement negative resistances, and showed measured data as well. Each of these two types of NICs are either open circuit stable or short circuit stable. In 1957, Larky [3] and Yanagisawa [4] presented the current inversion NICs comprised of transistors and also showed experimental results. Note that, although the topologies of NICs have been developed a long while ago, the practical realization is still difficult due to stability problems.

6.1.1 Basic Definitions

A NIC is defined as an active two-port network where the driving port impedance is converted to the negative of a load impedance connected to the other port. An ideal NIC is shown in Fig. 6.1, where the input impedance Z_{in} , seen at port 1, is the negative of K multiplied by the corresponding load impedance, Z_L at port 2, where K is the impedance transfer ratio of the NIC. For an ideal NIC, K is a positive real constant.

Another way to describe the NIC is use of hybrid h -parameters. Fig. 6.2 shows the equivalent model for a general two-port h -parameter network with an arbitrary passive

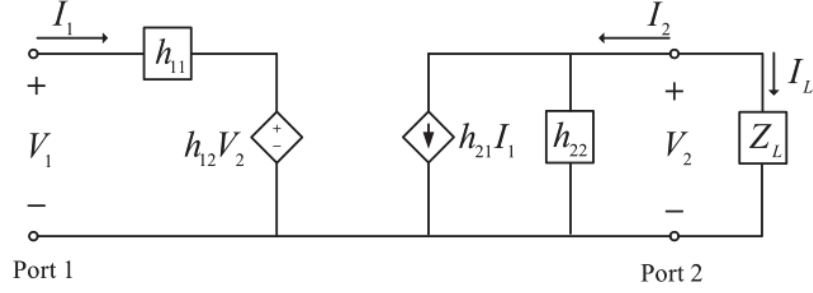


Figure 6.2: Equivalent model for a general two-port h -parameter network with an arbitrary passive load Z_L at port 2. [6]

load Z_L at port 2. The defining equations for the model are as follows:

$$\begin{aligned} V_1 &= h_{11}I_1 + h_{12}V_2 \\ I_2 &= h_{21}I_1 + h_{22}V_2 \end{aligned} \quad (6.1)$$

Since the port 2 is terminated with a passive impedance Z_L , the input impedance (seen into port 1) reads as

$$\begin{aligned} Z_{in} &= \frac{V_1}{I_1} = h_{11} - \frac{K \cdot Z_L}{1 + h_{22}Z_L}, \\ K &= h_{12}h_{21}. \end{aligned} \quad (6.2)$$

Here, K stands for the conversion ratio. Particularly, for an ideal NIC with $K = 1$, the following conditions should be satisfied by inspection of Eq. (6.2)

$$\begin{aligned} h_{11} &= h_{22} = 0 \\ h_{12}h_{21} &= 1. \end{aligned} \quad (6.3)$$

Consequently, two basic types of NICs can be developed depending on the sign of both h_{12} and h_{21} [6]. The first type is referred to as a current inverter or INIC when

both h_{12} and h_{21} are positive and unity, thus Eq. (6.1) leads to

$$V_1 = V_2, \quad I_1 = I_2. \quad (6.4)$$

This makes the following relationship between the current at port 1 and load impedance Z_L

$$I_1 = -I_L. \quad (6.5)$$

Hence, the input impedance at the port 1 is

$$Z_1 = \frac{V_1}{I_1} = \frac{I_L Z_L}{-I_L} = -Z_L. \quad (6.6)$$

Clearly, it does current inversion without affecting the polarity of input and output voltages. This can be written in the matrix form as

$$h = \begin{bmatrix} 0 & 1 \\ 1 & 0 \end{bmatrix}. \quad (6.7)$$

Another possible way to achieve negative input impedance is to reverse one port voltage leaving polarity of currents unchanged. Thus, $I_1 = -I_2$, $V_1 = -V_2$, which again leads to a simple h -parameter matrix

$$h = \begin{bmatrix} 0 & -1 \\ -1 & 0 \end{bmatrix}. \quad (6.8)$$

The device defined by Eq. (6.8) is referred to as a voltage inverter or VNIC.

6.1.2 Compensation Network

As proposed in [7], practical or non-ideal NIC has non-zero h_{11} and h_{22} and need compensation using passive network for zeroing them. A passive network in series with practical

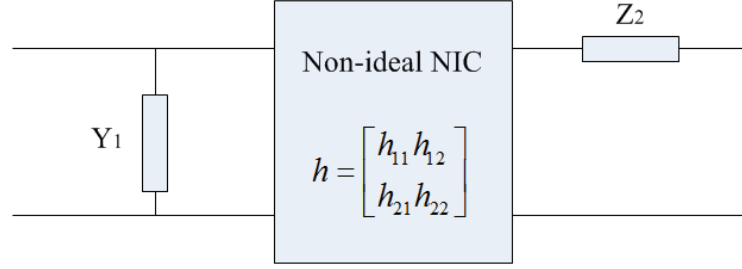


Figure 6.3: General model of a non-ideal NIC compensated with additional passive lumped elements.

NIC at one port and shunt at other port can make the overall two port network as ideal NIC ($h_{11} = h_{22} = 0$) as shown in Fig. 6.3

By circuit analysis, the h -matrix of overall network including compensation network is obtained by

$$h = \begin{bmatrix} \frac{h_{11} + Z_2 \Delta h}{1 + h_{11} Y_1 + h_{22} Z_2 + Y_1 Z_2 \Delta h} & \frac{h_{12}}{1 + h_{11} Y_1 + h_{22} Z_2 + Y_1 Z_2 \Delta h} \\ \frac{h_{21}}{1 + h_{11} Y_1 + h_{22} Z_2 + Y_1 Z_2 \Delta h} & \frac{h_{22} + Y_1 \Delta h}{1 + h_{11} Y_1 + h_{22} Z_2 + Y_1 Z_2 \Delta h} \end{bmatrix}, \quad (6.9)$$

where, $\Delta h = h_{11} h_{22} - h_{12} h_{21}$. For an ideal current inversion NIC, as the h -parameters are given in Eq. (6.7), we can therefore formulate the values of Z_2 and Y_1 by comparing to the matrix of Eq. (6.9)

$$\begin{aligned} Z_2 &= -\frac{h_{11}}{\Delta h} \\ Y_1 &= -\frac{h_{22}}{\Delta h}. \end{aligned} \quad (6.10)$$

Substituting Eq. (6.10) into matrix Eq. (6.9), we get

$$h = \begin{bmatrix} 0 & -\frac{\Delta h}{h_{21}} \\ -\frac{\Delta h}{h_{12}} & 0 \end{bmatrix}, \quad (6.11)$$

The compensated network behaves as ideal NIC with a positive conversion ratio

$$K = \frac{(\Delta h)^2}{h_{12}h_{21}}. \quad (6.12)$$

Here, we make the assumption that all h -parameters are real, since most practical electronic circuits can be considered to have real h -parameters at low frequencies. Such that, it is straightforward to see that the passive compensation networks Y_1 and Z_2 are a positive conductance and a positive resistance, respectively. Furthermore, in order to make a compensated NIC as shown in Fig. 6.3 becomes an ideal NIC, the criteria can be derived from Eqs. (6.10) and (6.12) [7]

$$I \left\{ \begin{array}{l} h_{11} \geq 0 \\ h_{22} \geq 0 \\ \Delta h < 0 \\ h_{12}h_{21} > 0 \end{array} \right. \quad (6.13)$$

or

$$II \left\{ \begin{array}{l} h_{11} \leq 0 \\ h_{22} \leq 0 \\ \Delta h > 0 \\ h_{12}h_{21} > 0 \end{array} \right. \quad (6.14)$$

where the conditions for the compensation may be satisfied by either set of the two equations. Since most practical NICs have the product $h_{11}h_{22}$ less than $h_{12}h_{21}$, the criteria of the set (I) is more opted for the application. However, it should be noted that for our research, a high frequency and broadband NIC is in need which hence limits the application of the criteria discussed above.

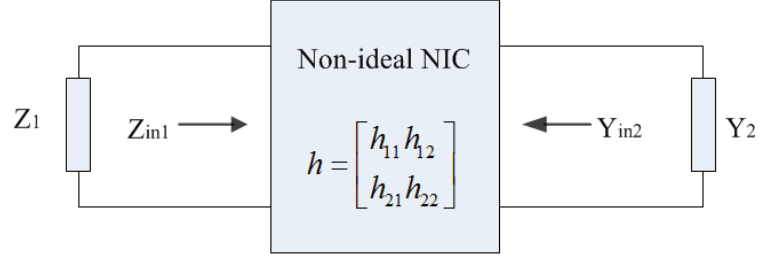


Figure 6.4: Compensated NIC with passive terminations.

6.1.3 Stability Analysis

In a compensated NIC, load impedance connected at the output port appears to be negative impedance at the input port. The NIC is stable or not, dependent on the passive network connected to the NIC. So, for the stability analysis of a NIC, we need to consider the complete system (NIC and its terminating network together). The analysis is dependent on whether any of the port of NIC is open circuit unstable (OCU), short circuit unstable (SCU), open circuit stable (OCS) and short circuit stable (SCS). Practically open circuit and short circuit conditions are determined by large impedance and small impedance respectively.

Practical NIC is SCS and OCU at one port, and OCS and SCU at the other port for achieving stability. SCS means almost zero impedance at one port and hence no zeros in right half s-plane. Also, OCS means almost infinite impedance at another port and hence no poles in right half s-plane. This approach is valid if NIC and its terminating network is linearly dependent on frequency. In the case of non-linear dependency on frequency, SCS-OCU at one port and OCS-SCU at other port, it is essential to prove the NIC is voltage controlled at one port and current controlled at other port.

Stability problem is not concern in ideal NIC ($h_{11} = h_{22} = 0$), because it is symmetrical and both ports are identical. But for a practical NIC, we need to be concerned about stability issues. Consider a practical non ideal NIC terminated by Z_1 and Y_2 as shown in Fig. 6.4, we can derive the input impedance at port 1 based on the relations

between the voltages V_1 , V_2 and currents I_1 , I_2 expressed by Eq. (6.1)

$$Z_{in1} = \frac{\Delta h + h_{11}Y_2}{h_{22} + Y_2}. \quad (6.15)$$

Similarly, the input admittance at port 2 is given as

$$Y_{in2} = \frac{\Delta h + h_{22}Z_1}{h_{11} + Z_1}. \quad (6.16)$$

In general, Z_1 and Y_2 are passive and positive real rational functions

$$Z_1 = \frac{N_1(s)}{D_1(s)}, \quad Y_2 = \frac{N_2(s)}{D_2(s)}. \quad (6.17)$$

Now, substituting Eq. (6.17) into Eq. (6.15) and Eq. (6.16), one obtains

$$\begin{aligned} Z_{in1} &= \frac{\Delta h D_2(s) + h_{11} N_2(s)}{h_{22} D_2(s) + N_2(s)} \\ Y_{in2} &= \frac{\Delta h D_1(s) + h_{22} N_1(s)}{h_{11} D_1(s) + N_1(s)} \end{aligned} \quad (6.18)$$

As per the condition (I) given by Eq. (6.13), it is straightforward that both denominators from Eqs. (6.18) are Hurwitz polynomials, since h_{11} and h_{22} are positive real numbers and $N_1(s)$, $D_1(s)$, $N_2(s)$ and $D_2(s)$ are all Hurwitz polynomials [8]. This means, both Z_{in1} and Y_{in2} cannot have right half s -plane poles, resulting in OCS at port 1 and SCS at port 2 [9, 10]. Moreover, from Eqs. (6.18), it is not difficult to see that the numerators of both immittances are not Hurwitz polynomials since the coefficients of both constant terms are negative, such that Z_{in1} and Y_{in2} have right half s -plane zeros, which leads to SCU at port 1 and OCU at port 2 [9, 10]. It should be noted that the addition of a passive network to compensate the practical non-ideal NIC does not change the form of Eq. (6.15) and (6.16), because the compensation networks can be included in the immittances Z_{in1} and Y_{in2} . Hence the conclusion derived above is also applicable to a fully compensated ideal NIC. It concludes that there are two types of NICs when its output port is terminated in a passive load.

- Open circuit stable NIC: having OCS at input port and SCS at output port. In case of BJT based NIC, it has emitters at input-output ports of NIC.
- Short circuit stable NIC: having SCS at input port and OCS at output port. In case of BJT based NIC, it has collectors at input-output ports of NIC.

The above analysis theoretically presents a methodology of designing a stable low frequency NIC circuit. In our work of design process, however, it should be noted that this analysis is not sufficient for ensuring stability, since the h -parameters for a high frequency NIC will be frequency dependent complex numbers and the compensation network cannot be formulated using a positive real rational function as well.

6.2 Design and Analysis of Operational Amplifier Based NICs

6.2.1 Ideal Op-Amp Properties

The operational amplifier, or op amp as it is commonly called, is a fundamental active element of analog circuit design. It is most commonly used in amplifier and analog signal processing circuits in the frequency band from 0 to 100 kHz. High-frequency op amps are used in applications that require a bandwidth into the MHz range. The first op amps were vacuum-tube circuits which were developed for use in analog computers. Modern op amps are fabricated as integrated circuits that show little resemblance to the early circuits. The ideal op amp is a three terminal circuit element that is modeled as a voltage-controlled voltage source. That is, its output voltage is a gain multiplied by its input voltage. The circuit symbol for the ideal op amp is given in Fig. 6.5 (a). The input voltage is the difference voltage between the two input terminals. The output voltage is measured with respect to the circuit ground node. The model equation for the output

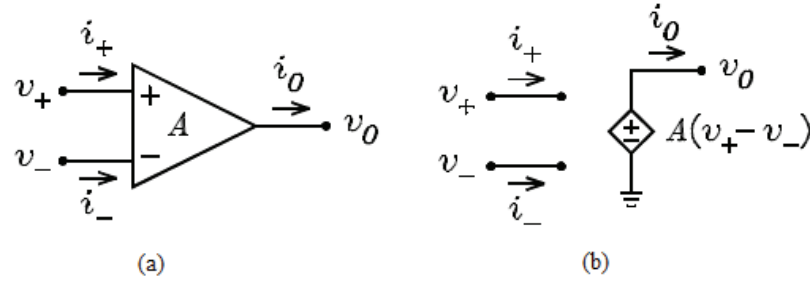


Figure 6.5: (a) Op-amp symbol. (b) Controlled-source model. [11]

voltage is [11]

$$v_O = A(v_+ - v_-), \quad (6.19)$$

where A is the voltage gain, v_+ is the voltage at the non-inverting input, and v_- is the voltage at the inverting input. The controlled source model of the ideal op amp is shown in Fig 6.5 (b).

The terminal characteristics of the ideal op amp satisfy four conditions. These are as follows:

- The current in each input lead is zero.
- The output voltage is independent of the output current.
- The voltage gain A is independent of frequency.
- The voltage gain A is very large, approaching infinity in the limit.

The first condition implies that the resistance seen looking into both input terminals is infinite. The second implies that the voltage gain is independent of the output current. This is equivalent to the condition that the output resistance is zero. The third implies that the bandwidth is infinite. The fourth implies that the difference voltage between the two input terminals must approach zero if the output voltage is finite.

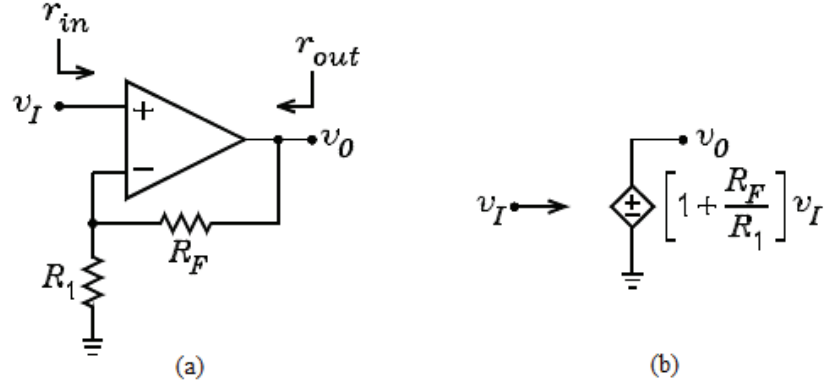


Figure 6.6: (a) Non-Inverting amplifier. (b) Controlled-source model. [11]

6.2.2 Non-Inverting Amplifier

Fig 6.6 (a) shows the circuit diagram of a non-inverting amplifier. The input voltage v_I is applied to the non-inverting op amp input. A voltage divider consisting of resistors R_F and R_1 connects from the output node to the inverting input. The circuit is called a non-inverting amplifier because its voltage gain is positive. This means that if the input voltage is increasing or going positive, the output voltage will also be increasing or going positive.

For the circuit of Fig 6.6 (a), the voltage difference between the two op amp input terminals is given by $v_+ - v_- = v_O/A$. For v_O finite and $A \rightarrow \infty$, it follows that $v_+ \rightarrow v_-$. It is said that a virtual short circuit exists between the two inputs because there is no voltage difference between the two terminals. For $i_- = 0$, the condition that $v_+ = v_-$ requires v_I and v_O to satisfy the equation

$$v_+ = v_- \Rightarrow v_I = v_O \frac{R_1}{R_F + R_1}, \quad (6.20)$$

where voltage division has been used for v_- . This can be solved for the voltage gain to obtain

$$\frac{v_O}{v_I} = 1 + \frac{R_F}{R_1}. \quad (6.21)$$

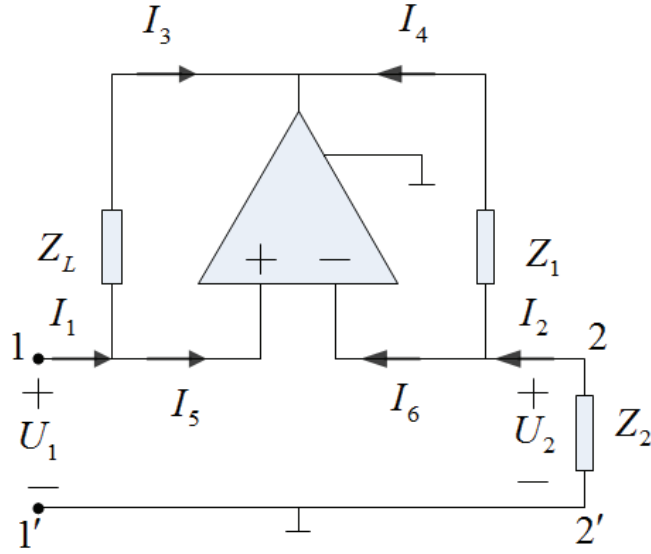


Figure 6.7: Topology of an op-amp based NIC.

The input and output resistance are given by

$$r_{in} = \infty, \quad r_{out} = 0. \quad (6.22)$$

The controlled source model for the non-inverting amplifier is shown in Fig. 6.6 (b).

6.2.3 Ideal Op-Amp Based NIC Circuit

As shown in Fig. 6.7, the schematic of an ideal op-amp based NIC circuit is proposed as an application of the non-inverting configuration [12]. For the proposed circuit, the impedance Z_1 bridges the input and output terminals of a non-inverting amplifier. We can write

$$U_1 = U_2 = -I_2 Z_2, \quad (6.23)$$

which gives

$$I_3 Z_L = I_4 Z_1. \quad (6.24)$$

Since the current in each input lead for an ideal op-amp is zero, we may write

$$I_1 = I_3, \quad I_2 = I_4. \quad (6.25)$$

Substituting into Eq. (6.24), we have

$$I_1 Z_L = I_2 Z_1 \quad (6.26)$$

further to

$$I_1 = \frac{Z_1}{Z_L} I_2 \quad (6.27)$$

Finally, from Eqs. (6.23) and (6.27), the input resistance from port 1-1' is given by

$$Z_{in1} = \frac{U_1}{I_1} = -\frac{Z_2}{Z_1} Z_L, \quad (6.28)$$

which clearly exhibits an ideal NIC with the conversion ration Z_2/Z_1 . In general, the elements Z_1 , Z_2 and Z_L are not necessary to be pure resistances which means they may be capacitors, inductors, or impedance networks [12].

For the purpose of verification, here, we propose a schematic design of an ideal op-amp based negative capacitance circuit using Agilent ADS 2009U1 [13]. The schematic of the proposed circuit is shown in Fig. 6.8. Assuming the following values for the lumped elements

$$\begin{aligned} R_1 &= 1k\Omega \\ R_2 &= 1k\Omega \\ C_1 &= 5pF, \end{aligned} \quad (6.29)$$

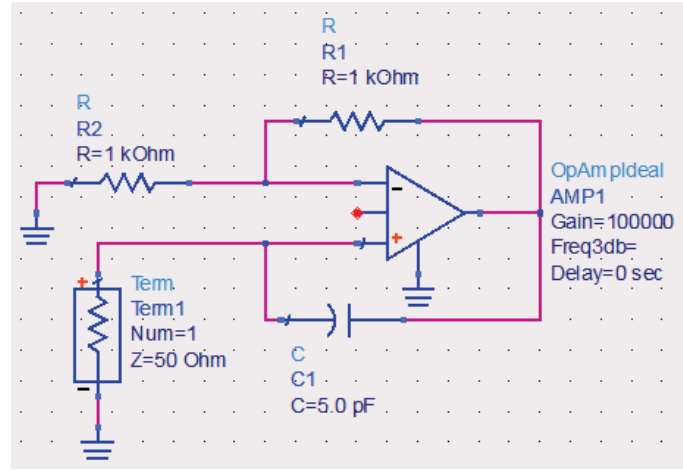


Figure 6.8: Schematic of an ideal op-amp based negative capacitance circuit captured from Agilent ADS.

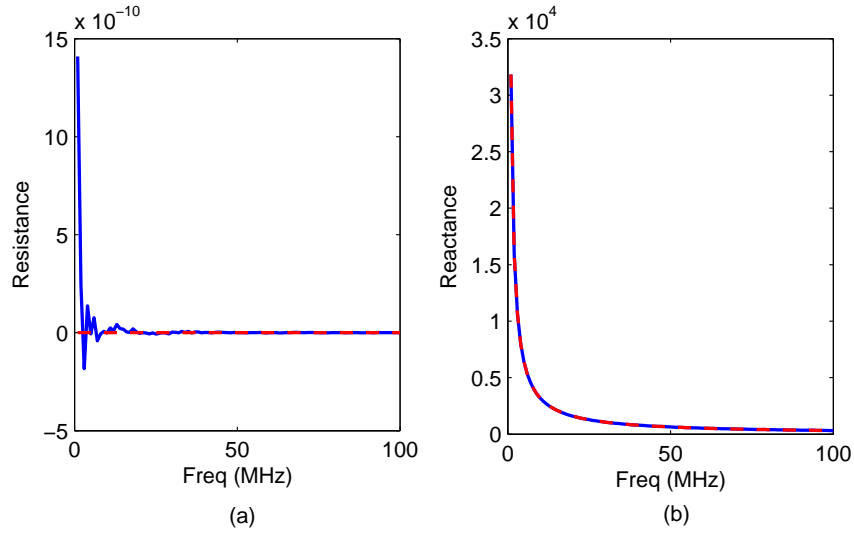


Figure 6.9: Input impedance of the NIC circuit based on an ideal op-amp simulated using ADS, as compared to the theoretical results. The simulated case is represented by blue-solid line while the theoretical case is represented by red-dashed line. (a) Resistance. (b) Reactance. It is shown that there is good agreement between both cases, although the simulated resistance exhibits some oscillations at low frequencies due to the finite gain.

One may obtain the theoretical input impedance from Eq. (6.28)

$$Z_{in1} = -\frac{R_2}{R_1} \frac{1}{j\omega C_1} = j \frac{1}{\omega C_1}. \quad (6.30)$$

The real and imaginary parts of the input impedance obtained from the simulation are shown in Fig. 6.9, as compared to the results given by Eq. (6.30). Clearly, it is shown that the simulated case are in excellent agreement with the theoretical calculations, and so it is possible to achieve a constant negative capacitance over a wide frequency band using the ideal op-amp based circuit.

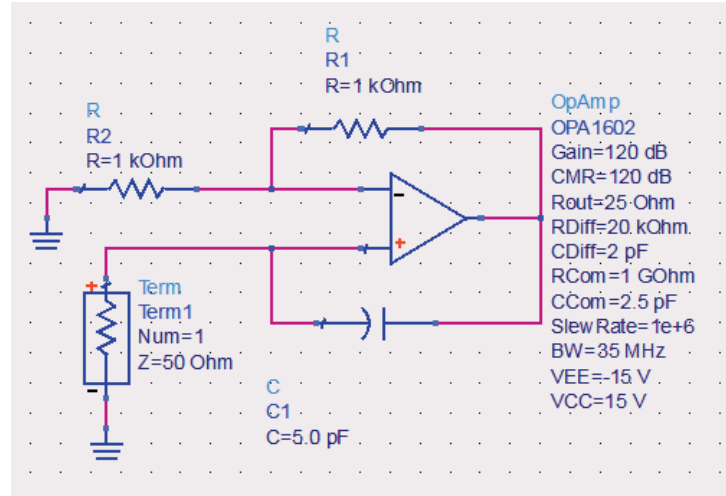
6.2.4 Real Op-Amp Based NIC Circuit

However, we should note that, the above analysis are based on an ideal op-amp model which differs from the real op-amps in various aspects. It is said that, real op-amps suffers from several non-linear effects, such as finite gain, finite input impedances, non-zero output impedances, etc. In order to illustrate how these effects affect the performance of the NIC circuit, we replace the ideal op-amp in Fig. 6.8 with a real op-amp. As an example, we choose the Texas Instruments OPA1602 as the op-amp which has a bandwidth up to 35MHz and open-loop gain of 120dB [14].

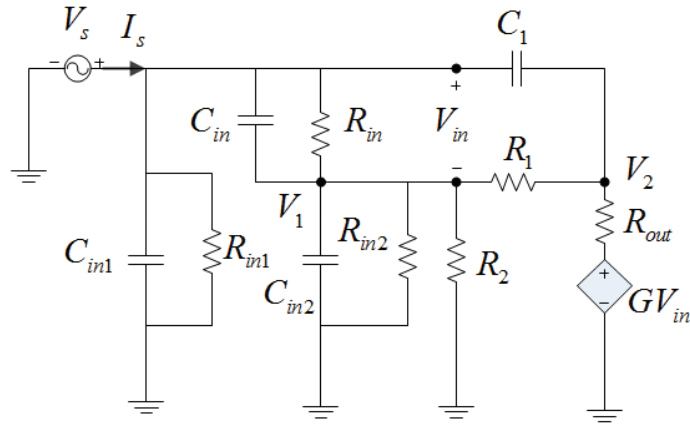
Fig. 6.10 (a) shows the schematic captured from ADS of the real op-amp based negative capacitance circuit. Based on the parameters found in the datasheet of OPA1602 [14], it may be possible for us to create a behavior model of the NIC circuit as depicted in Fig. 6.10 (b) in a similar manner to Ref. [15]. It is shown that the op-amp is replaced by a controlled-source model with parasitical impedances at both input and output leads. Tab. 6-A presents the explicit values of the circuit model parameters.

A mathematical model corresponding to Fig. 6.10 (b) may be constructed by using Kirchhoffs voltage law (KVL) and current law (KCL) to generate a set of equations relating the voltages V_1 , V_2 , V_{in} and V_s . Here, we have

$$\begin{aligned} V_{in} &= V_s - V_1 \\ \frac{V_s - V_1}{Z_0} &= \frac{V_1}{Z_2} + \frac{V_1 - V_2}{R_1} \\ V_2 &= \left[j\omega C_1(V_s - V_2) + \frac{V_1 - V_2}{R_1} \right] R_{out} + GV_{in}, \end{aligned} \quad (6.31)$$



(a)



(b)

Figure 6.10: (a) Schematic of an real op-amp based negative capacitance circuit captured from Agilent ADS. (b) Behavior model of the real op-amp based NIC circuit, where the op-amp are described as a controlled-source model with parasitical lumped elements.

where $Z_0 = R_{in} \parallel C_{in}$ is the differential input impedance and $Z_2 = R_{in2} \parallel C_{in2} \parallel R_2$ is the parallel of the common-mode input impedance at the inverting op-amp input and the external resistance R_2 . From Eqs. (6.31), it is straightforward to derive the analytical solutions of voltages V_1 , V_2 related to the source voltage V_s . However, due to the cumbersome algebraic manipulations, thus, we choose to give their symbolic expressions

Table 6-A: Circuit model parameters of the op-amp based NIC

Parameter	Lumped Element	Value
Differential Input Impedance	$R_{in} \parallel C_{in}$	$20K\Omega \parallel 2pF$
Common-Mode Input Impedance	$R_{in1} \parallel C_{in1}, R_{in2} \parallel C_{in2}$	$10^9\Omega \parallel 2.5pF$
Output Impedance	R_{out}	25Ω
External Resistance	R_1, R_2	$1k\Omega$
Non-Inverting Capacitance	C_1	$5pF$
Open-Loop Gain	G	$120dB$

for the purpose of clarify

$$\begin{aligned} V_1 &= k_1 V_s \\ V_2 &= k_2 V_s. \end{aligned} \quad (6.32)$$

Here, k_1 and k_2 are the frequency dependent coefficients which can be solved from Eqs. (6.31). Furthermore, the source current can be obtained as

$$I_s = \frac{V_s}{Z_1} + j\omega C_1(V_s - V_2) + \frac{V_s - V_1}{Z_0}, \quad (6.33)$$

where $Z_1 = R_{in1} \parallel C_{in1}$ is the common-mode input impedance at the non-inverting op-amp input. Substitution of Eq. (6.32) into Eq. (6.33) yields the input impedance of the op-amp based NIC circuit

$$\begin{aligned} Z_{in1} &= \frac{V_s}{I_s} \\ &= \frac{Z_0 Z_1}{Z_0 + Z_1(1 - k_1) + j\omega C_1 Z_0 Z_1(1 - k_2)}. \end{aligned} \quad (6.34)$$

In particular, by assuming an ideal op-amp with $Z_1 = Z_2 = 0$ and $Z_0 = \infty$ and $G = \infty$, Eq. (6.34) can be rewritten as

$$Z_{in1} = \frac{R_1 + R_2 + GR_2}{j\omega C_1(R_1 + R_2 - GR_1)} \Rightarrow j\frac{1}{\omega C_1}, \quad (6.35)$$

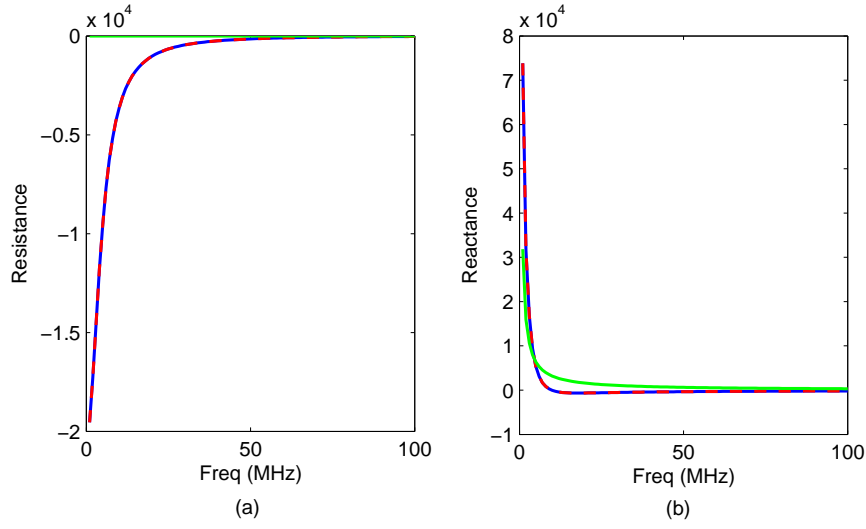


Figure 6.11: Input impedance of the NIC circuit based on an real op-amp simulated using ADS, as compared to the theoretical cases. The simulated case is plotted with blue-solid lines, while the theoretical case (I) from Eq. (6.34) is represented by red-dashed line, and case (II) from Eq. (6.35) is green-solid. (a) Resistance. (b) Reactance. It is shown that the simulation results again match the analytical solution very well. However, it also indicates the error between the ideal and real op-amp based NICs.

which validates the previous analysis on an ideal op-amp based NIC as given by Eq. (6.30).

The simulated input impedance of the op-amp OPA1602 based NIC by ADS are depicted in Fig. 6.11, as compared to its analytical solution. For comparison, we also plot the ideal case as obtained from Eq. (6.35). Although it is shown that the simulation results are in excellent agreement with its theoretical counterpart, we should note the differences between the ideal and real op-amp based NICs which clearly exhibit the effects on the NIC performance of the parasitics of an non-ideal op-amp. Hence, it may not be applicable for op-amp based NICs in the design of microwave devices which usually request high frequency and broadband properties.

6.3 Design and Analysis of Transistor Based NICs

6.3.1 Floating NIC Circuit

The first practical transistorized NICs were designed, built and tested by Linvill [2] in 1954. He built negative resistance circuits using both grounded and floating NICs. As shown in Fig. 6.12 (a), a floating transistor NIC circuit is proposed. The circuit shown are "open-circuit stable" (OCS), meaning, practically, that if a very large resistance terminates the negative-resistance one-ports on the left, then the overall network will be stable. The equivalent circuit of Linvill's NIC can be extracted as shown in Fig. 6.12 (b). Moreover, the input impedance of the converter circuit is given based on its circuit model

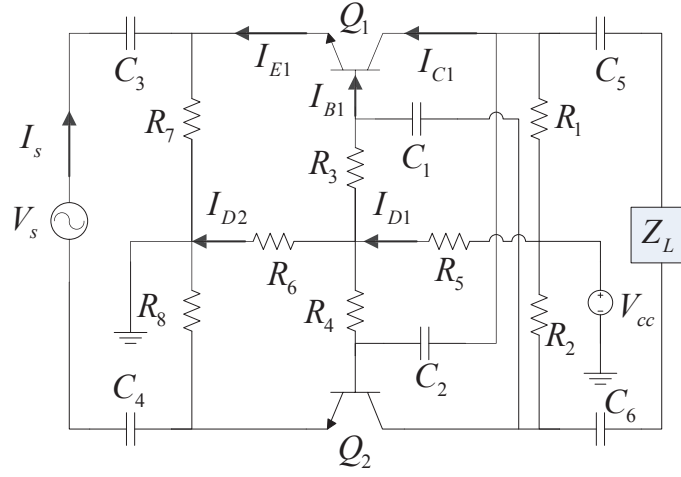
$$\begin{aligned} Z_{in1} &= \frac{V_s}{I_s} \\ &= 2r_e + (1 - \alpha)(2r_b + \frac{2Z_g(Z_L + 2Z_d)}{2Z_g + Z_L + 2Z_d}) - \alpha Z_N \frac{Z_g}{Z_g + Z_d}, \end{aligned} \quad (6.36)$$

where

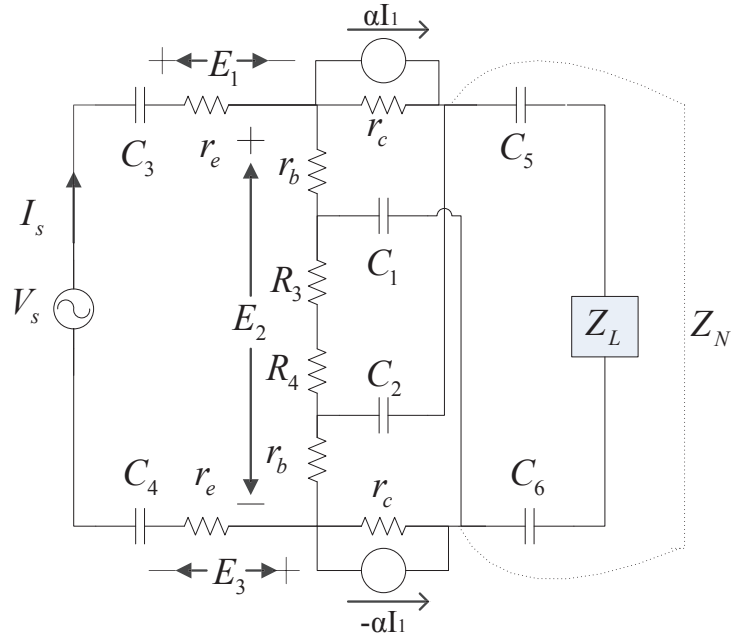
$$\begin{aligned} Z_g &= R_3 = R_4, \\ Z_d &= 1/(j\omega C_1) = 1/(j\omega C_2), \\ Z_N &= Z_L \parallel (2Z_g + 2Z_d), \end{aligned}$$

and α is an important transistor parameter which indicates the common-base current gain. For the operating frequency, followed by $Z_d \rightarrow 0$, the input impedance can be thereby approximated as

$$Z_{in1} \approx (1 - 2\alpha)Z_N + 2r_e + (1 - \alpha)2r_b. \quad (6.37)$$



(a)



(b)

Figure 6.12: (a) Linvill's floating OCS NIC. (b) Equivalent circuits of Linvill's floating OCS NIC. [2]

Furthermore, since the value of α for a BJT transistor normally falls between 0.98-0.998 and r_b is typically equal to 20Ω , we can rewrite the above equation as

$$Z_{in1} \approx (1 - 2\alpha)Z_N + 2r_e. \quad (6.38)$$

Note the independence of the input impedance with respect to the point of operation is important for a negative-impedance converter. However, the α value normally varies significantly with the point of operation, which hence makes the biasing scheme very important since it contributes considerable effects to the deviation of working point. However, for a low frequency operation, we can assume that α is independent of the operation point, thus, it only varies with the frequency changes roughly according to the relationship [2]

$$\alpha = \frac{\alpha_0}{1 + jf/f_{cut}}, \quad (6.39)$$

where f_{cut} is called the α cut-off frequency which mainly depends on the transistor itself.

To illustrate the utility of this floating NIC circuit, we designed and optimized in ADS a practical implementation of a transistor based negative resistance circuit as shown in Fig. 6.13. We should note here that, in order to avoid the possibility of instabilities due to the negative impedance, a large resistance Z_s is employed in series with the NIC input. For our experiment, we choose multcomp 2N2222A as the NPN transistors Q_1

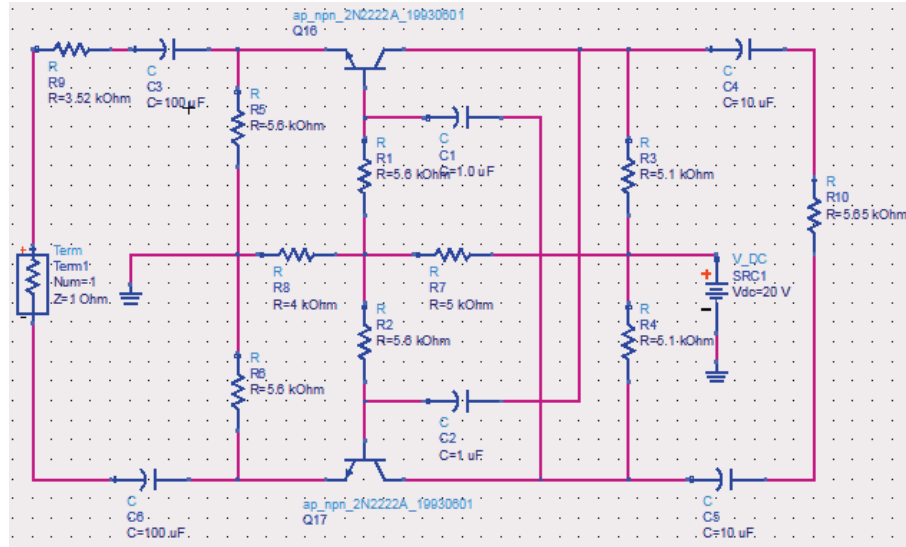


Figure 6.13: Schematic of a transistor based floating NIC circuit captured from Agilent ADS to achieve a negative resistance.

and Q_2 which are commonly used for low frequency application [16], thus, the other circuit parameters of the NIC circuit can be analytically calculated by assuming the DC

operation point as $V_{CE} = 4.5V$ and $I_C = 1.5mA$.

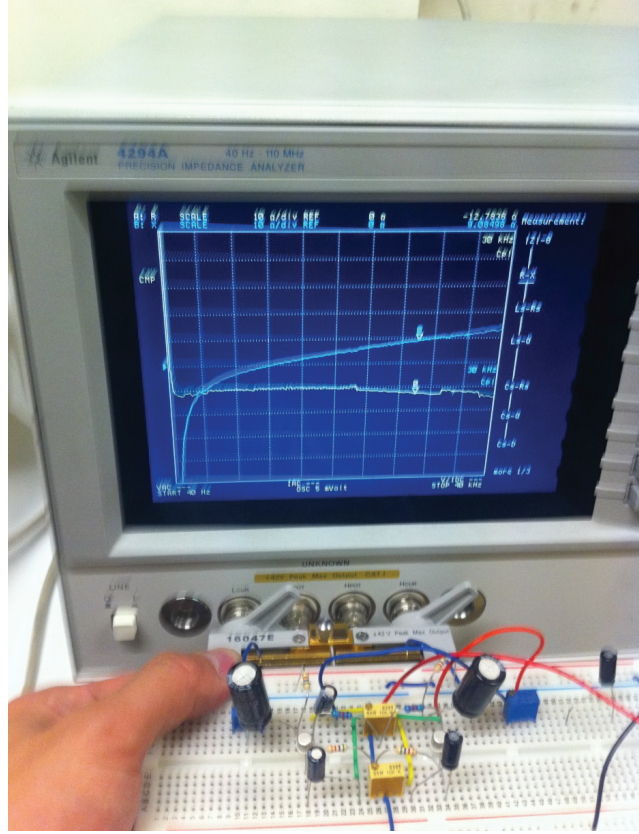


Figure 6.14: Prototype of the transistor based floating NIC circuit.

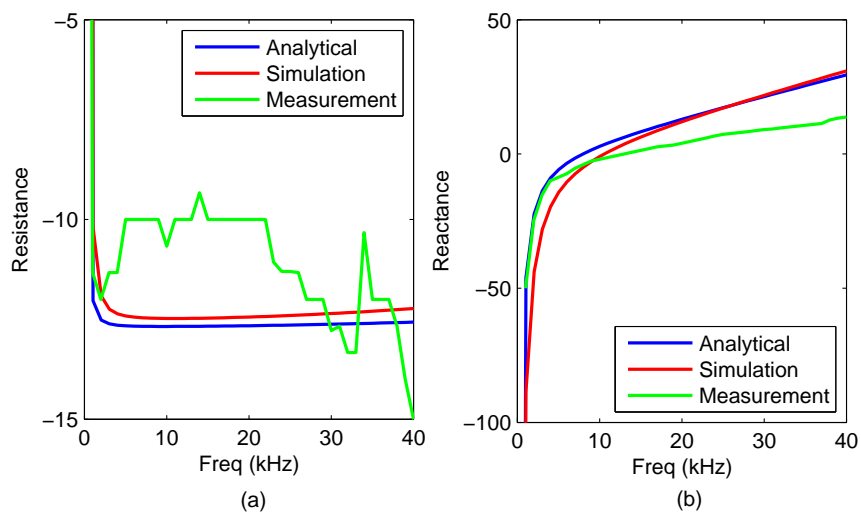


Figure 6.15: Measured input impedance of the floating NIC circuit, as compared to the simulation and theoretical cases. (a) Resistance. (b) Reactance.

Fig. 6.14 shows the fabricated prototype using the breadboard and measured by Agilent 4294A impedance analyzer. The measured input impedance of the NIC circuit is depicted in Fig. 6.15. For comparison, we also plot the ADS simulated impedance and the theoretical calculation from Eq. (6.38). It is shown that the measurement results match very well with the simulation as well as the analytical solution, thus, validating Linvill's design concept. However, we note that this circuit is found to work only at low frequencies due to the α cut-off frequency. As an example, its negative performance degrades significantly as the frequency increases, and the resistance part also becomes extremely dispersive when the frequency ranges up to MHz. One way to overcome this limitation is to employ high quality transistors with high cut-off frequency. Hence, improved transistor based NIC circuits using print circuit board (PCB) will be introduced later by applying different transistors and topologies to achieve better performance.

6.3.2 Grounded NIC Circuit

Recently, Sussman-Fort gives a modified NIC design based on Linvill's circuit with its application to impedance matching of electrically small antennas (ESAs) [5]. In his paper, a negative capacitor obtained from the NIC is connected to the antenna in series to improve both antenna gain and signal to noise ratio (SNR) from 20MHz to 120MHz. Furthermore, he also presents a grounded NIC model based on Linvill's OCS NIC as shown in Fig. 6.16, which is of potential interest for us to develop another type of transistor based NIC. By relating the voltages across the different resistors and currents flowing in the circuit, the principle of this circuit model is given as follows:

- Input current flows through Q_1 producing V_L across Z_L
- V_L fed back through CE stage Q_2 producing 180° phase inversion at B_1
- Voltage at E_1 , V_s , appears in phase with voltage at B_1
- $Z_{in1} = V_s/I_s$ seen to be negative of Z_L : because current is the same, but voltages

are inverted.

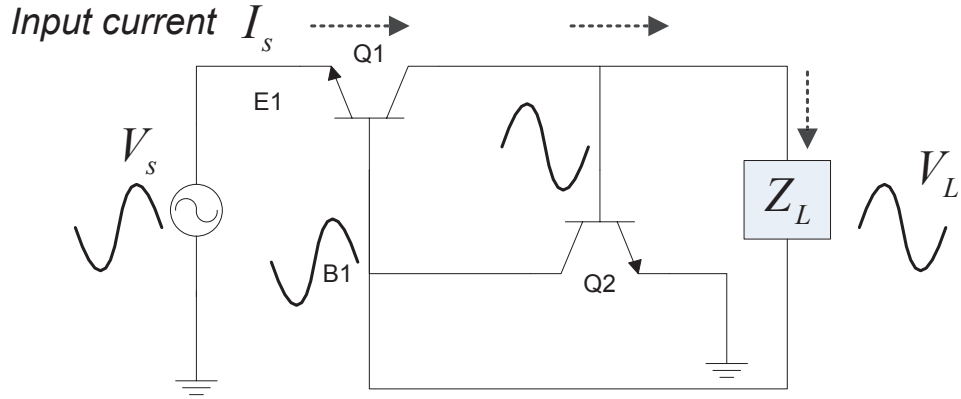


Figure 6.16: Grounded NIC model based on Linvill's OCS NIC [5].

Clearly, the above circuit model represents an voltage-inversion NIC as mentioned earlier. Subsequently, one may derive the analytical solution to verify the principle by introducing a small-signal equivalent circuit as depicted in Fig. 6.17. Therein, the BJT transistors Q_1 and Q_2 are replaced by their equivalent control models. Depending on whether the emitter is grounded or not, the hybrid- π and T models are applied to represent the different transistors, respectively.

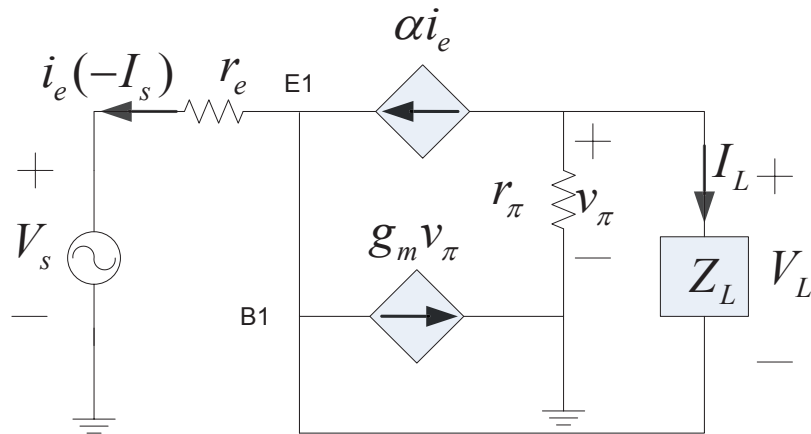


Figure 6.17: Small-signal equivalent circuit of the grounded NIC model.

Once again, Kirchhoff's law is used to construct circuit equations relating the voltages and currents in the circuit as follows

$$\begin{aligned} g_m v_\pi + \frac{v_\pi}{r_\pi} + i_e &= 0, \\ I_L - g_m v_\pi - (1 - \alpha)i_e &= 0, \\ V_s + i_e r_e + V_L &= v_\pi. \end{aligned} \tag{6.40}$$

Here g_m is the transconductance determined by the dc collector current of the transistor, while r_e , r_π and α are the typical model parameters. Assuming Q_1 and Q_2 are identical to each other, such that

$$\begin{aligned} r_e &= \frac{\alpha}{g_m}, \\ r_\pi &= \frac{\beta}{g_m}, \\ \beta &= \frac{\alpha}{1 - \alpha}. \end{aligned} \tag{6.41}$$

By substituting Eqs. (6.41) into Eqs. (6.40), one may obtain the input impedance as

$$\begin{aligned} Z_{in1} &= -\frac{V_s}{i_e} \\ &= 2r_e + (1 - 2\alpha)Z_L \approx -Z_L \end{aligned} \tag{6.42}$$

which exhibits an voltage inversion NIC with the conversion ratio approximated to 1.

In our experiment, however, we seek to build a negative parallel-RLC network for eventual use in the design of active metamaterials as mentioned in chapter 3. Shown in Fig. 6.18 is the ADS schematic which illustrates the actual circuit that we built. The circuit was hand-constructed using discrete components on RF-prototyping circuit boards. Note that, data on the negative RLC itself were de-embedded from measurements including a known, stabilizing positive inductor placed in series with the NIC input.

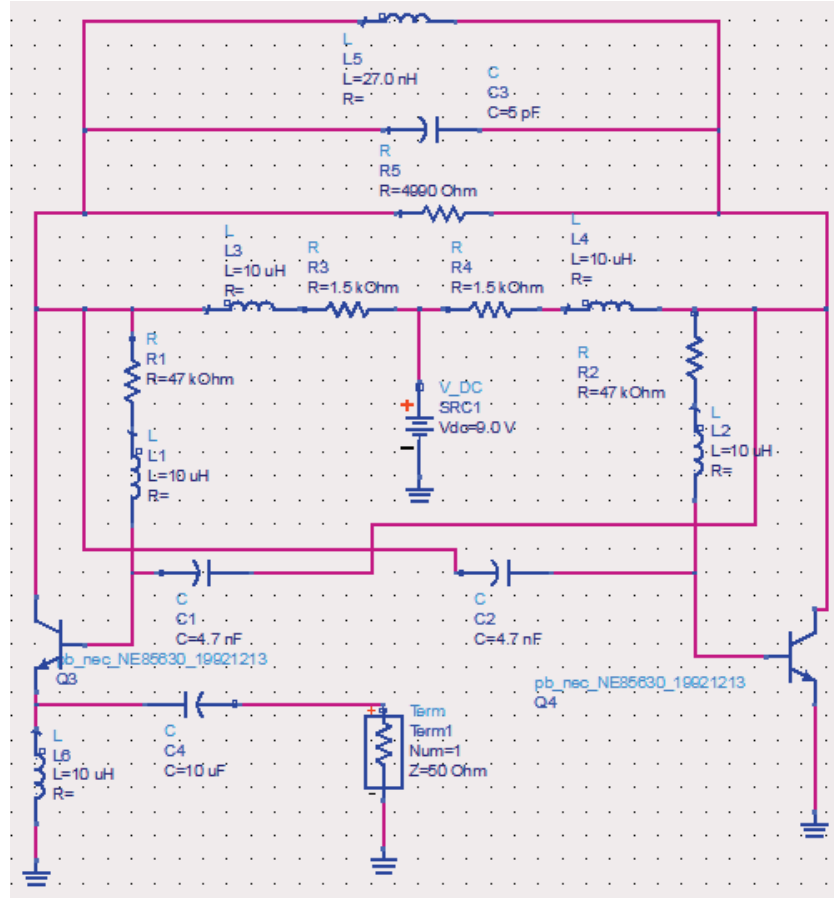


Figure 6.18: Schematic of a transistor based grounded NIC circuit captured from Agilent ADS to achieve a negative parallel-RLC network.

Subsequent to verifying the design scheme, a prototype of the NIC circuit is presented as shown in Fig. 6.19. This circuit uses NEC NE85630 BJTs with inductor-resistor biasing, and fabricated on FR4 substrate which has $\epsilon_r = 4.4$ and thickness $h = 1.6\text{mm}$. In order to obtain the negative impedance components, its positive counterpart which consists of a parallel-RLC circuit is employed as the NIC load Z_L , while the corresponding lumped elements are chosen to be $R_L = 4990\Omega$, $L_L = 27\text{nH}$ and $C_L = 5\text{pF}$ for convenience. All of these components are from Multicomp using 0805 or 0603 surface mount packaging. Since our design goal is to achieve a negative impedance network up to 1GHz which has gone beyond the capabilities of the impedance analyzer, an Agilent PNA5230C network analyzer is therefore used for our measurement.

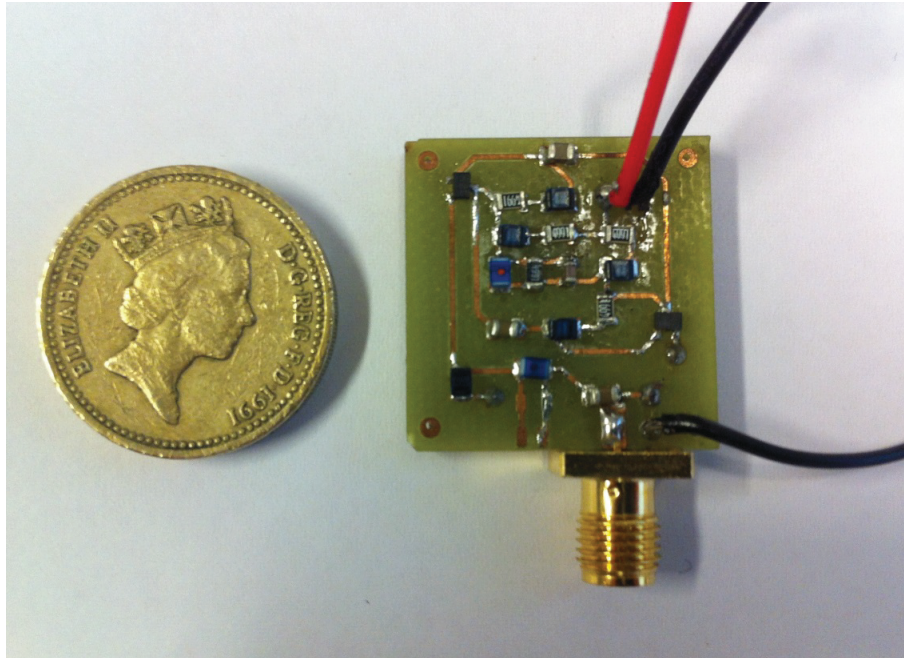


Figure 6.19: Prototype of the transistor based grounded NIC circuit.

Fig. 6.20 shows the frequency variations of the measured input impedance of the NIC circuit. Moreover, the simulation and analytical results are also plotted for comparison. Clearly, the measurement results differs from its simulated and analytical counterparts due to the parasitics and nonlinearities of the actual circuit. However, we should note that, by replacing the NIC load capacitance with $C_L = 2.1pF$, the modified analytical case may represent an analogical curve to the measurement case despite some irregular mismatches, thus validating our design approach. Furthermore, by considering the effects of the parasitics of the real circuit on the NIC performance, it is shown that this circuit provides a good solution to achieving the negative reactive elements. Nevertheless, it is beyond the capabilities of producing frequency independent negative resistances, thus affecting the overall performance. Finally, we should note that, this design is based on the ADS schematic simulation, which is less accurate when the modeling practical circuits, since it does not account the interaction between traces and components. Consequently, in order to obtain more reliable results, the ADS electromagnetic (EM) simulation tool shall be applied to the NIC design which can model more realistic scenarios.

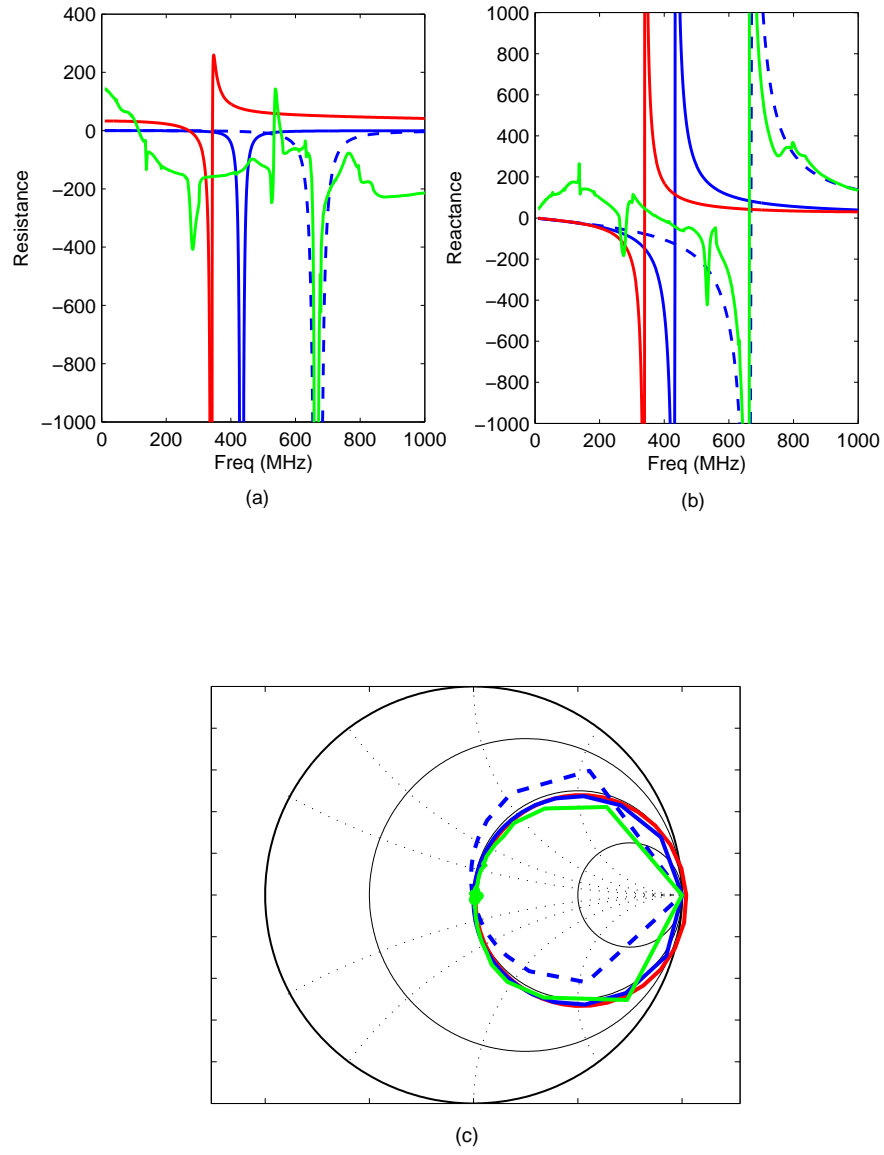


Figure 6.20: Measured input impedance (green-solid) of the grounded NIC circuit, as compared to the simulation (red-solid) and analytical cases (blue-solid and blue-dashed). Here, two analytical cases are given: case (I) (blue-solid) corresponds to the designed NIC circuit with load capacitance $C_L = 5pF$, while case (II) (blue-dashed) is an modification of case (I) to fit the measurement results, by replacing the capacitance with $C_L = 2.1pF$. (a) Resistance. (b) Reactance. (c) Smith-chart plotting.

6.4 Conclusions

In this chapter, the design and analysis of negative impedance converter are presented as an important part for the design of active metamaterials. Starting with the modeling of a standard negative impedance converter, the characteristics of both ideal and non-ideal NIC circuits are reviewed in terms of its compensation network and stability analysis. However, we should note that, due to the parasitics and nonlinearities of the real NIC circuits in high frequencies, these proposed principles are limited for application in our design, although they do provide some concepts which are helpful for our work.

Subsequently, two categories of NIC circuits based on different active components are demonstrated. First, NIC circuits realized using technology of operational amplifiers are investigated. Due to the basic properties of an ideal op-amp, the circuit configuration of an non-inverting amplifier can be used to construct an ideal NIC circuit. However, it is shown that, the real op-amp based NIC may be affected by the non-ideal effects of the practical op-amp, thus leads to reduced performance as compared to the ideal op-amp based NIC. Conversely, the transistorized NICs provide a good solution to these problems. Based on Linvill's OCS NIC [2], two types of transistor based NICs are developed: one is the floating NIC which is convenient for series insertion into an external network. For the purpose of verification, a practical NIC fabricated on breadboard is presented following the theoretical analysis and ADS schematic simulation, to achieve a negative resistance. The measurement results are shown to match very well with the simulated and analytical cases. However, it is noted that this NIC circuit is very frequency limited and always accompanies a considerable imaginary part, thus limits its application in the design of active metamaterials. Another type of transistor based NIC we demonstrated is the grounded NIC circuit which is also developed from Linvill's design concept. This circuit is fabricated on FR4 substrate, and exhibits a negative parallel-RLC network up to 1GHz, although there are still a few mismatches between the measurement, simulation, and analytical results. However, by comparing the different cases, it is evident that the schematic simulation is not reliable for the RF NIC design,

since it can not model the non-ideal effects of the real circuit. Note that, by inspection the active metamaterial structure as discussed before, it is simple to show that to achieve the broadband and other material properties, a floating NIC circuit is required which can be inserted in each unit cell. Hence, the corresponding circuit design are under experiments, and so far only electromagnetic simulation results can be provided as shown in Fig. 3.10.

References

- [1] J. Merrill, "Theory of the negative impedance converter," *Bell Syst. Tech. J.*, vol. 30, no. 1, pp. 88–109, 1951.
- [2] J. G. Linvill, "Transistor negative impedance converters," *Proc. IRE.*, vol. 41, pp. 725–729, 1953.
- [3] A. Larky, "Negative-impedance converters," *Circuit Theory, IRE Transactions on*, vol. 4, no. 3, pp. 124–131, 1957.
- [4] T. Yanagisawa, "Rc active networks using current inversion type negative impedance converters," *Circuit Theory, IRE Transactions on*, vol. 4, no. 3, pp. 140–144, 1957.
- [5] S. E. Sussman-Fort and R. M. Rudish, "Non-foster impedance matching of electrically-small antennas," *IEEE Transactions on Antennas and Propagation*, vol. 57, pp. 2230–2241, 2009.
- [6] A. K. Perry, "Broadband antenna systems realized from active circuit conjugate impedance matching," DTIC Document, Tech. Rep., 1973.
- [7] L. K. Shing, *Systematic realization of negative impedance converter and its application to the synthesis of driving-point nonlinear characteristic*. MPhil Dissertation, Hong Kong University, 1973.
- [8] F. Kuo, *Network analysis and synthesis*. John Wiley and Sons., 1966.
- [9] K. L.-C. Su, *Active network synthesis*. McGraw-Hill, 1965.
- [10] M. E. Van Valkenburg, *Introduction to modern network synthesis*. John Wiley and Sons., 1967.
- [11] Gatech. [Online]. Available: <http://users.ece.gatech.edu/mleach/ece3050/sp04/>

OpAmps01.pdf

- [12] W.-K. Chen, *The circuits and filters handbook*. CRC Press, 2002.
- [13] Advanced Design System 2013, Agilent Technologies, URL: <http://www.agilent.com/>.
- [14] [Online]. Available: www.ti.com/product/opa1602
- [15] [Online]. Available: <http://masteringelectronicsdesign.com/>
- [16] [Online]. Available: <http://www.farnell.com/datasheets/1449532.pdf>

Chapter 7

Conclusions and Future Work

7.1 Conclusions

The main objective of the research work presented in this dissertation is to analyze and design active metamaterials. First of all, the tunable metamaterials based on composite right/left handed transmission line (CRLH TL) structures are introduced with the application in the design of varactor controlled leaky-wave antennas. And then we paid most of our attention to the application of non-Foster impedance matching in the design of active metamaterials including broadband magnetic metamaterials and high impedance surfaces (HIS). As is well known, conventional metamaterials suffer from the inherent limitations such as high loss and narrow bandwidth. However, by incorporating the negative reactive elements to compensate the self reactance of the structures, non-Foster loading is proved to be an effective solution to these problems.

In **Chapter 2**, varactors were applied to the design of composite right/left-handed (CRLH) structures based on the transmission line (TL) theory, a multi-functional antenna with both the fixed beam and scanning capability was designed and fabricated. It was shown that an fixed-beam operation can be achieved by manipulating the reverse-biasing voltage applied to the varactor diodes.

Chapter 3 presented the characterization of active magnetic metamaterials with non-Foster loads. Based on the effective medium model, several techniques were explored for analyzing the stability of the actively-loaded medium. In particular, an immittance-based stability criterion was proposed and applied to the practical design of broadband active metamaterials, where a novel stability criterion named the Exponential Peaking Stability Criterion (EPSC) was proposed which imposes a forbidden region in the complex plane, so as to give the design specifications of an arbitrary load for a given unloaded loop array. It was shown that the EPSC is less conservative than all the other criteria proposed for ensuring robust stability. Subsequently, the wave propagation in the actively-loaded medium was investigated based on the transmission line theory. Furthermore, by inspection of the relation between the wave propagation and the effective medium properties, a broadband zero loss magneto-inductive transmission structure was proposed based on the combination of the NIC circuits and negative resistance amplifiers. And in **Chapter 4**, a general analytical model was developed for the prediction of the noise performance of broadband, stable active metamaterials based on negative impedance converters (NICs). It was shown that active metamaterials with NICs demonstrated much higher noise levels in comparison with passive metamaterials consisting of resonant structures. However, active metamaterials possess extraordinary material properties which are impossible to implement with passive media, over such broad frequency ranges.

In **Chapter 5** a detailed investigation on the characterization of active high impedance surface (HIS) with non-Foster loads was provided. Based on the circuit model of normal unloaded HIS, we developed the principle of active broadband HIS by employing the non-Foster loads. Similar as the design of active metamaterials, the stability of actively-loaded HIS were also examined. By applying the Routh-Hurwitz technique, we gave the stability conditions for an parallel negative RLC loaded HIS. Furthermore, the Nyquist criterion is used to verify the proposed stability conditions. As an example, the application of the stability analysis in the design of actively-loaded HIS was demonstrated. It

was shown by choosing appropriate NIC loads, we could achieve a broadband but with fixed resonance HIS design, while keeping the system stable.

Finally in **Chapter 6**, the design and analysis of NIC circuit were presented as an important part for the design of active metamaterials including both MNG and HIS metamaterials. Starting with the modeling of a standard negative impedance converter, the characteristics of both ideal and non-ideal NIC circuits were reviewed in terms of their compensation network and stability analysis. Afterwards, two categories of NIC circuits based on different active components are demonstrated. First, NIC circuits realized using technology of operational amplifiers were investigated. It was shown that the real op-amp based NIC may be affected by the non-ideal effects of the practical op-amp, thus leading to reduced performance as compared to the ideal op-amp based NIC. Conversely, the transistorized NICs provide a good solution to these problems. Based on Linvill's OCS NIC, two types of transistor based NICs were developed: one is the floating NIC which is convenient for series insertion into an external network. Another type of transistor based NIC we demonstrated is the grounded NIC circuit. Both NIC circuits were simulated and fabricated. The former NIC was built on breadboard and showed very good matching between the measurement results and the simulation results. However, it was also seen that this NIC circuit is very frequency limited and always accompanies a considerable imaginary part, thus limiting its application in the design of active metamaterials. The latter one was for the active metamaterials application which required a negative parallel-RLC network up to 1GHz. The measurement results have verified our design by considering the parasitics, although there are still a few mismatches exhibited. However, we should note that the latter one was a grounded NIC circuit, but for our application, a floating NIC circuit is required making a new NIC design necessary.

7.2 Future Work

In our work, active metamaterials have been proposed as an effective means to overcome the inherent limitations of their passive counterparts, thus can achieve the extraordinary properties in a broadband. However, a reliable floating RF NIC design and the integration of the active circuits and the passive structures is still a challenge for us due to the sensitivity of the NIC circuits. Presently, we are still experimenting with the circuit design and approaching the final success since the electromagnetic simulations have given us more confidence.

Arising from the research carried out during this work, areas of potential further research could include the followings

- So far we have only shown the applications of tunable metamaterials in the design of leaky-wave antennas. However, by incorporating of the varactors and 2D or 3D periodic structures, more metamaterial devices can be developed, such as tunable high impedance surfaces.
- In our work, the design of active magnetic metamaterials based on the real NIC design is proposed and verified by simulations. However, the NIC fabrication delayed our work progress. In the near future, we will continue with the experimental verification of this actively-loaded medium. Moreover, as discussed before, one of the potential extension of the active magnetic metamaterials is the design of zero-loss and broadband metamaterials by integrating the NIC circuit and negative impedance amplifier which could be considered for realization as well. After that, we will concentrate on the applications of the active metamaterials, such as novel antennas, imaging devices, and other RF components.
- For active high impedance surface, we also have provided the design principle and simulation samples. However, it is noted that the working frequency of the proposed design does not fit the practical NIC circuit. Such that we need decrease

the resonant frequency of the unloaded HIS structure by increasing the substrate thickness and the periodic size of each unit cell. As before, the experimental verification and possible applications are within our research scope.

- As mentioned previously, the NIC design is the key part of the design of broadband active metamaterials. So far we have demonstrated some successful samples. However, the parasitics and sensitivity in the high frequencies limit their applications. Hence, we need still need improve its performance by optimizing the circuit structure. The experimental work is ongoing for the moment and approaching the final success.